

MILD Combustion in Confined Flows: Reactor Features and Modelling Needs



Giuseppe Ceriello

Tutor: Prof. Antonio Cavaliere

Supervisors: Dr. Giancarlo Sorrentino

Dr. Raffaele Ragucci

PhD Program: Industrial Product and Progress
Engineering

Department of Chemical, Materials and Production
Engineering (DICMaPI)

University of Naples 'Federico II'

This dissertation is submitted for the degree of

Doctor of Philosophy

2020

To my family,
with endless love.

*The more a man knows, the more willing he is to learn. The less
a man knows, the more positive he is that he knows
everything...*

Robert G. Ingersoll

*Success is not the key to happiness. Happiness is the key to
success. If you love what you are doing, you will be successful.*

Albert Schweitzer

Run to rescue with love and peace will follow.

River Phoenix.

Contents

Abstract.....	vii
List of figures.....	xi
List of tables.....	xv
Chapter 1 Introduction.....	1
1.1 Energy, Combustion and Environment.....	1
1.2 MILD Combustion.....	4
1.2.1 Definition.....	4
1.2.2 MILD systems classification.....	7
1.2.3 Heat transfer role.....	10
1.2.4 Modelling issues and strategies.....	13
1.3 Objectives and Outline of the thesis.....	17
Chapter 2 Experimental test case.....	19
2.1 Cyclonic chamber.....	19
2.2 Operative parameters.....	21
2.3 Measurements and uncertainties.....	22
2.4 Dominant heat transfer mechanisms.....	25
2.5 Thermal uniformity.....	27
Chapter 3 Numerical methods.....	29
3.1 Flamelet Generated Manifolds.....	29
3.1.1 Basic principles and operational steps.....	29
3.1.2 Flamelet equations.....	31
3.1.3 Manifold generation.....	34
3.2 CFD setup.....	37
3.2.1 Grid independence study.....	37
3.2.2 Turbulence model.....	38
3.2.3 Radiation model.....	41
3.3 CFD code and FGM interaction.....	43
Chapter 4 Results of the CFD Modelling.....	47
4.1 CFD simulation of the MILD cyclonic burner.....	47
4.2 Sensitivity on the chemistry resolution.....	50

4.2.1 Effect of the kinetic mechanism.....	51
4.2.2 Effect of Flamelet configuration	52
4.3 Sensitivity on the external operating parameters	54
4.3.1 Inlet mixture composition	55
4.3.2 Preheating temperature.....	57
4.3.3 Dilution level.....	58
4.3.4 Diluent nature.....	62
4.4 Sensitivity on the radiative heat transfer.....	67
4.5 Comparison with PSR tabulation.....	72
Chapter 5 Reactor Parameters and Manifold Reduction	77
5.1 Main parameters of a MILD reactor	77
5.2 Tabulation by means of Diluted Homogeneous Reactor	79
5.3 DHR tabulation applied to the cyclonic burner	82
5.3.1 Sensitivity to the heat loss and dilution levels	83
5.3.2 Dilution and heat loss constraints for the cyclonic burner	85
Chapter 6 Conclusions and Future Perspectives	91
6.1 Conclusions.....	91
6.2 Future perspectives	94
References	97
Acknowledgements	109

Abstract

Nowadays, the constant increase in energy demand is in conflict with the constraints imposed by environmental sustainability related to the use of new energy sources. The simultaneous fulfillment of such requirements results in the design of innovative combustion systems. In this context, configurations with high levels of internal dilution and preheating show several peculiarities related to low pollutant emissions, smooth temperature gradients (thermal uniformity), absence of a visible flame and large fuel and load flexibility. These features are usually difficult to obtain within conventional processes and are associated with the so-called MILD Combustion regime. Such a combustion mode consists of the dilution and preheating of the reactants through the recirculation of the exhausts. It allows avoiding the high-temperature regions and steep temperature gradients which are typical of traditional combustion. Therefore, MILD Combustion ensures low pollutant emissions in terms of NO_x and CO and large fuel flexibility. However, the large-scale use of such technology relies on the improving of the numerical modelling of the multiple physical phenomena connected to the strong interconnection between fluid-dynamics and kinetics time scales. In addition, heat transfer plays a key role in the modulation of such behavior because of the strong confinement of the walls usually present in these systems. The adoption of tabulated chemistry methods represents a possible solution to characterize the thermo-chemical pattern of a MILD combustion system. However, the definition and identification of the controlling variables must be done in a proper way. In this thesis, the main features of a MILD Combustion system are analyzed and investigated by means of an experimental and numerical study on a cyclonic burner. In particular, the work is focused on understanding the physical mechanisms occurring under this regime, addressing the key parameters responsible for its stabilization and giving indications regarding the developing of adequate numerical models.

In the first part of this thesis (Chapter 1 and 2), the main characteristics of the MILD Combustion are presented, and the experimental test case object of this work is described. Several literature studies highlighting the most common numerical

methodologies for MILD systems and the role of heat transfer on their combustion features are reported and discussed. In particular, thermal behavior is analyzed in order to stress the distinctive role of heat loss and evaluate the convective and radiative contributions. The test case burner, based on the establishment of a cyclonic flow to ensure elevated internal recirculation levels, is introduced as a representative of a specific category named MILD reactors. In the second part of the thesis (Chapter 3 and 4) the tabulated chemistry methodology used is described, and the results of the CFD simulation are evaluated by making a comparison with the experiments. A Flamelet-based model (FGM) is adopted. It makes two main assumptions: a turbulent flame can be considered as an ensemble of 1D laminar flames (Flamelets), and the space of compositions can be represented by a lower-dimensional manifold by defining few controlling variables. Two different 1D flame configurations and two controlling variables (a mixture fraction and a progress variable) are used. To take into account the significant radiative heat transfer in the cyclonic burner, radiation is also coupled into the FGM model by means DO model. The radiative properties of gases are modelled with a WSGG model which accounts for the local mole ratio between CO_2 and H_2O . In addition, a method to consider turbulence-radiation interaction with FGM has also been developed. The comparisons between model and experiments are reported for different inlet conditions evaluating the influence of the operative parameters on both the MILD features and the performances of the model. The comparisons are shown for two temperature profiles within the cyclonic chamber. Experiments report an elevated uniformity of the temperature field for all the conditions investigated. The numerical results, however, are strongly affected by the inlet dilution level due to the internal exhaust recirculation. In fact, for low dilution levels of the reactant mixture, the model is not able to predict the low and distributed reactivity of the system, especially in the inlet area. On the other hand, the conditions with high dilution at inlet show a very good agreement with the experiments because of the lower impact of the recirculating products. The inclusion of a radiation model has a big impact in improving the numerical/experimental agreement, especially respect to the high thermal uniformity. Finally, the choice of the Flamelet configuration does not affect the simulations significantly except for the inlet area because of the diffusion/mixing effects. The tabulation by means a PSR depicts a slight

overprediction compared to the FGM because of the absence of a radiation model. In the last part of the thesis (Chapter 5 and 6), a new methodological approach to tabulate internal dilution and heat loss effects for a MILD reactor is presented and the main conclusions of the work are summarized. The method proposed allows to include as the controlling variables of the system, a dilution parameter and a heat loss factor in addition to progress variable and mixture fraction. The reduction of the reactivity related to the combined effects of these new variables is discussed. Finally, a reduction of the complete thermo-chemical manifold representing the cyclonic burner behavior, is carried out by considering physical and process constraints related to the features of the MILD reactor. The lower-dimensional manifolds found, related to mean values of dilution level and heat loss (estimated by measurable quantities) are compared with the experimental thermal fields for different conditions. The good results obtained represent a promising indication for the future development of comprehensive CFD models for the simulation of that kind of combustion systems for any operative conditions.

List of figures

1.1 - Worldwide primary energy consumption by energy source [1].....	2
1.2 - Reactor schematization of a MILD Combustion system.....	5
1.3 - Classification of different combustion regimes according to Cavaliere and de Joannon [2].....	6
1.4 - A burner operating under conventional (left) and MILD conditions (right) [3].....	6
1.5 - Combustion regimes diagram proposed by Rao and Levy [4].....	8
1.6 - Total emissivity of pure carbon dioxide (left) and pure water vapor (right) as a function of temperature, adapted from [5] and converted to SI units [59].....	11
1.7 - Iso-surfaces of the reaction rate and x–y, y–z and z–x planes of temperature field. The gray iso-surfaces correspond to a reaction rate of 0.7 whereas the coloured ones to 1.05, where interacting and non-interacting local flame fronts are respectively denoted by purple and light blue colours [6].....	14
2.1 - Picture of the midplane section of the cyclonic burner under frozen (top) and mild (bottom) conditions at left; sketch of the cyclonic chamber, the feeding system, the movable thermocouples and the materials at right.....	19
2.2 - Inner alumina layer (left) and outer steel case (right) of the cyclonic chamber...	20
2.3 - Thermocouples system.....	23
2.4 - Measured temperature profiles T _l (left) and T _c (right) with the relative uncertainties under a mild condition sample case.....	24
2.5 - Ratio between radiation and convection heat flux for CO ₂ (left) and H ₂ O (right) as a function of the mean gas temperature and at different wall temperatures and operating points under MILD condition for LUCY burner (red area).....	26
3.1 - Distribution of mixture fraction in a 2D DNS calculation from [7] (left) and distribution of hydrogen molar fraction on the flamelet extracted from the thick black curve (right).....	30

3.2 - Temperature evolutions along the spatial coordinate, in time for an igniting mixing layer configuration (left), and at different compositions for a premixed flame (right). For both configuration the stoichiometric air/methane case with the C1C3 kinetic mechanism [8] is reported.....	32
3.3 - Manifolds in the Z, J space for the progress variable production rate (left) and the temperature (right) calculated for the stoichiometric air/methane case with the C1C3 kinetic mechanism [8] and the IML configuration.....	36
3.4 - Structured computational grid of the LUCY burner depicted for the external domain (left) and the internal midplane section (right).....	38
3.5 - Study of independence on the number of grid cells.....	38
3.6 - Comparison between the measured and simulated tangential velocity profiles in the mid-plane along the direction at $x=0.1$ m (left) and at $y=0.1$ m (right).....	39
3.7 - Effect of the inlet turbulence levels (TI) on the temperature predictions.....	40
3.8 - Schematic representation of the numerical model separated in a pre-processing and an online calculation part.....	45
4.1 - Simulated pathlines of the cyclonic flow field for case A.....	48
4.2 - Simulated velocity (left) and temperature (right) fields of the cyclonic chamber for case A.....	49
4.3 - Simulated fields for several quantities on the midplane of the cyclonic chamber for case A.....	50
4.4 - Measurements with uncertainties (symbols with error bars) and predicted temperature by FGM (solid lines) using three different kinetic mechanisms for case B.....	51
4.5 - Manifolds in the Z, J space for $\dot{\omega}_J$ and temperature calculated for case A with premixed 1D flame (left) and IML (right).....	52
4.6 - Measurements with uncertainties (symbols with error bars) and predicted temperature by FGM (solid lines) using two different Flamelet configuration for case A and C.....	53
4.7 - Measurements with uncertainties (symbols with error bars) and predicted temperature by FGM (solid lines) at different inlet compositions.....	56

4.8 - Comparison between the measured (symbols) and modelled (solid lines) volumetric concentrations of major species at different inlet compositions.....	57
4.9 - Measurements with uncertainties (symbols with error bars) and predicted temperature by FGM (solid lines) at different inlet temperatures.....	58
4.10 - Manifolds in the Z, J space for $\dot{\omega}_J$ (left) and temperature trends against Z changing J (right), for three different dilution levels.....	59
4.11 - Measurements with uncertainties (symbols with error bars) and predicted temperature by FGM (solid lines) at different inlet dilution levels.....	60
4.12 - Contours of $\dot{\omega}_J$ (left) the temperature (right) at the inlet region for three different inlet dilution levels.....	61
4.13 - Manifolds in the Z, J space for $\dot{\omega}_J$ (left) and temperature trends against Z changing J (right), for N_2 (case A) and CO_2 (case H) as diluent species.....	63
4.14 - Measurements with uncertainties (symbols with error bars) and predicted temperature by FGM (solid lines) for N_2 (case A) and CO_2 (case H) as diluent....	64
4.15 - Contours of $\dot{\omega}_J$ (left) the temperature (right) at the inlet region for N_2 (case A), CO_2 (case H) and the fictitious species N_2^* (case H*) as diluent.....	65
4.16 - Numerical lateral (left) and central (right) temperature profiles for N_2 (case A), CO_2 (case H) and the fictitious species N_2^* (case H*) as diluent.....	66
4.17 - Simulated temperature fields without (left) and with (right) the inclusion of the radiative model. Case A.....	68
4.18 - Measurements with uncertainties (symbols with error bars) and predicted temperature by FGM with (solid lines) and without (dashed lines) radiation model at different inlet conditions.....	68
4.19 - Simulated field of the volumetric absorbed and emitted radiation at the midplane of the cyclonic chamber for case A.....	69
4.20 - Role of radiation on temperature uniformity (expressed by the parameter R) as a function of the overall heat loss by the system. Case A.....	71
4.21 - Schematic of the non-adiabatic PSR.....	72
4.22 - Mid-plane contours of the reaction rate and temperature (left) and reaction zone behavior under different MILD conditions (right).....	73

4.23 - Measurements with uncertainties (symbols with error bars) and predicted temperature by FGM and Non-adiabatic PSR model (solid lines) at different inlet compositions.....	74
4.24 - Measurements with uncertainties (symbols with error bars) and predicted temperature by FGM and Non-adiabatic PSR model (solid lines) at different inlet temperatures.....	75
5.1 - Sketch at the midplane of the velocity field of the cyclonic burner with the evaluation section of the recirculation factor k (thick black line).....	78
5.2 - Flow diagrams regarding traditional (left) and diluted homogeneous reactor approach (right).....	80
5.3 - DHR simulated temperature profiles as a function of the diluted mixture fraction Z for various J and at different (α, β) coordinates. Case I.....	83
5.4 - DHR simulated manifolds of $\dot{\omega}_J$ in the (J, Z_0) plane for case I and different (α, β) coordinates.....	84
5.5 - Measured temperature profiles inside the cyclonic burner (a-c); and DHR temperature and $\dot{\omega}_J$ simulated for estimated operational mean values of α and β (d-i) for cases I, M and L.....	87
5.6 - Measured temperature profiles inside the cyclonic burner (a-c); and DHR temperature and $\dot{\omega}_J$ simulated for estimated operational mean values of α and β (d-i) for cases O and N.....	88

List of tables

1.1 - Mild reactor categories: features and references	10
2.1 - List of the external operational parameters and their operating ranges.....	21
2.2 - Operating conditions test case for uncertainties analysis.....	24
2.3 - Operating conditions test case for heat transfer analysis.....	25
2.4 - Thermal uniformity evaluated inside the cyclonic chamber for different operating conditions.....	27
4.1 - Boundary conditions of case A.....	47
4.2 - Boundary conditions of cases A, B and C.....	50
4.3 - Boundary conditions of the cases used in the sensitivity study.....	54
4.4 - Boundary conditions for cases A, C and I.....	67
4.5 - Uniformity factor for experiments and simulations including and not the radiative heat transfer modelling.....	70
5.1 - Boundary conditions of the cases used for the DHR analysis.....	82

Chapter 1

Introduction

In this first chapter, the framework of this thesis is set. First, the motivations of the work are discussed with reference to the main queries and requirements regarding the innovative combustion-based energy systems (see [Section 1.1](#)). Afterwards, the thermo-chemical conversion process object of this study is defined, and its main features and issues are presented (see [Section 1.2](#)). In the end, the targets and the outline of the thesis are addressed (see [Section 1.3](#)).

1.1 Energy, Combustion and Environment

From the modest energy needs of pre-industrial revolution to the growing demands and technological innovations of the 21st century, energy technology has helped to shape the world we live in. The growing energy demand has led to several constraints that are quickly and constantly modifying the possible frameworks in the energy scenario. Such background usually regards the obtainment of reduced greenhouse gases (GHG) emissions as required by international regulations [1].

In the last decades, progress is being made towards the enhanced consumption of Renewable Energy Sources (RES), such as solar and wind energy. Nevertheless, as shown in Figure 1.1, the world energy consumption is expected to rise nearly 50% between 2018 and 2050 according to the International Energy Outlook 2019 from the US Energy Information Administration [1]. Therefore, we must deal with this greater supply and, at the same time, operate a transition to renewable sources. The latest projections depicted in Figure 1.1, moreover, predict a sharp increase of the renewables until they will reach the biggest share among the energy sources in 2050. Although such fast growth, fossil fuels will still account for about 70% of the world energy consumption in 2050, leading to serious environmental damage. In this context, it appears evident that the eco-sustainable development and improvement of the

efficiency of both thermal and electrical energy production plants are key requirements.

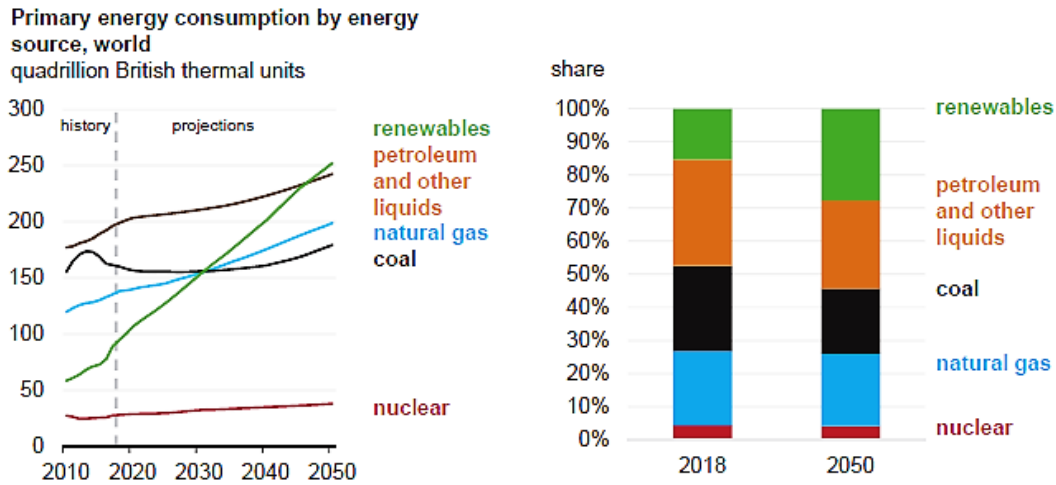


FIGURE 1.1 - WORLDWIDE PRIMARY ENERGY CONSUMPTION BY ENERGY SOURCE [1].

The generation of Power through RES requires a major update of back-up systems and infrastructures in order to ensure the energy supplies required and address the inherent RES intermittencies [9]. In this context, effective energy storage systems might offer a feasible solution to the intermittent nature of RES and help their integration into electrical grids. Among the possible solutions, chemical-based storage technologies, such as combustion, represent a valid option to store large amounts of energy for extended periods of time. In particular, the new combustion processes require the simultaneous fulfillment of several requisites such as the fuel flexibility, efficiency in term of pollutant reduction and thermal conversion and affordability of the supplies. Over the years, the wide development of combustion systems has led to damaging effects on our environment, e.g. air pollution (particulate matter, NO_x , SO_x) and climate change (releasing greenhouse gases like CO_2 into the atmosphere). Among the nitrogen oxides, NO_x , the most relevant for air pollution are the nitric oxide, NO , and nitrogen dioxide, NO_2 . The most dominant source of nitrogen oxides is the combustion of fossil fuels. In the atmosphere, those species can further react to produce

photochemical smog, acid rain, as well as enhance tropospheric ozone production and stratospheric ozone depletion [10].

Since is not feasible to switch the energy source from fossil fuels to renewables in a relatively short term, the greatest challenges which researchers are facing in the last years are the identification of new combustion technologies in order to:

- Maximize flexibility with respect to the nature of the fuel;
- Minimize pollutant emissions by reducing the environmental impact;
- Improve the distribution of energy production processes with efficient and reliable supply systems (smart grid).

Flexibility with respect to the type of fuel has been for a long time a common prerequisite in the design of combustion systems, mainly to meet commercial needs, such as the adaptation of power plants to the local availability of a given source. Nowadays, such flexibility is a fundamental requirement for dealing with both the rapid change in the fuel market and the increasing availability of energy carriers, mainly due to the growing diffusion of renewable and unconventional energy sources [11]. Regarding the environmental impact, the mitigation of air pollutant emissions has been a central priority for the EU Framework Program for Research and Innovation Horizon 2020 [12]. Finally, the implementation of a new energy production and distribution system based on the smart-grid concept is seen as a solution to locally increase the efficiency of energy distribution. Such a concept regards the construction of a strongly delocalized and flexible energy system. In fact, small and medium-scale energy production plants operate mainly in conditions of low energy efficiency and consequently with high environmental impact due to their limited technological development, considerably lower than large plants [13]. Thus, it is beneficial to improve the development of energy production systems capable of using both fossil fuels (even with low heating value) and alternative ones such as biomass or waste-derived.

Therefore, the final objective is the identification of innovative combustion technologies that can support the development of local energy production systems able to use different energy sources, with the improvement of the energy efficiency and the reduction of pollutant emissions.

1.2 MILD Combustion

Among the new combustion technologies developed in the last decades in order to face the requirements presented in [Section 1.1](#), MILD combustion seems to be one of the most promising. In this section, such a combustion process is defined as respect to its main operative boundaries and its main differences compared to other innovative systems are pointed out (see [paragraph 1.2.1](#)). Afterwards, different configurations and categories of systems are defined with respect to the main features of MILD technology (see [paragraph 1.2.2](#)). Then the role of the heat transfer and the effect of the walls are discussed (see [paragraph 1.2.3](#)). Finally, the main modelling issues and strategies related to the simulation of such a peculiar combustion regime are reported (see [paragraph 1.2.4](#)).

1.2.1 DEFINITION

A large share of literature concerning efficient and sustainable combustion systems deals with the evaluation of measurable quantities in order to identify useful qualitative and quantitative features, such as Flameless [14,15], Noiseless/Silent [16,17], Colorless/Optically Invisible [18,19] and Odorless/ Pollutants Absence [20,21]. Such features, which characterize the combustion process, are linked to both the specific inlet conditions imposed and the design of enclosure and feeding configuration, as schematized in Figure 1.2. The most relevant and documented boundaries considered to obtain these characteristics are related to dilution and preheating of the reactants, which are linked to the definition of the Moderate or Intense Low oxygen Dilution (MILD) combustion regime [22]. This regime arises from a change of perspective in the analysis of combustion problems, from purely energetic to chemical aspects: the combustion system is treated as a chemical reactor, which must be optimized for fuel flexibility, conversion efficiency and emissions. A MILD process is characterized by fuel oxidation in an environment with relatively low oxygen concentration and high inlet temperatures. Looking at the schematization of a MILD system depicted in Figure 1.2, it is worth highlighting that the post-determined combustion features can be obtained locally inside the system not only by diluting and preheating the fresh

reactants (imposed inlet boundaries), but also by design the enclosure in a proper way (reactor design).

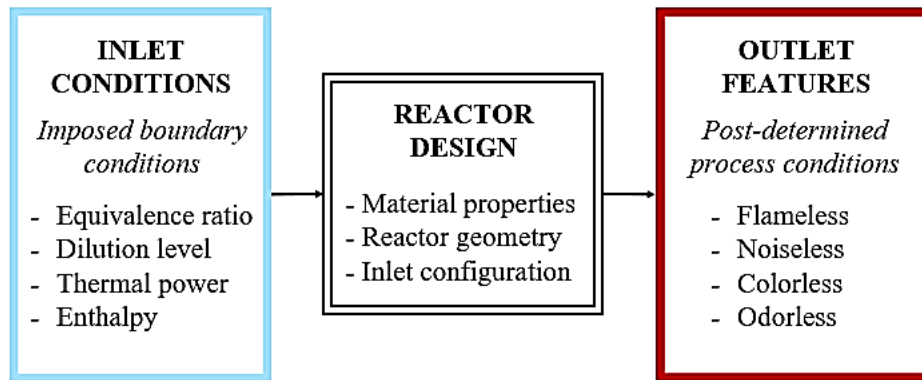


FIGURE 1.2 – REACTOR SCHEMATIZATION OF A MILD COMBUSTION SYSTEM.

Over the years, different definitions have been formulated to address MILD operative boundaries. Following Cavaliere and de Joannon [22], a combustion process can be defined as MILD if “the inlet temperature of the reactants is higher than the autoignition temperature of the mixture and, simultaneously, the increase in maximum temperature due to oxidation reactions remains lower than the mixture autoignition temperature because of the high dilution levels” [2]. This definition is depicted in Figure 1.3, where the operating regions of the different combustion regimes are shown in the dilution/preheating temperature (T_{in}) space. In the Figure, T_{ign} is the self-ignition temperature, X_{O_2} is the oxygen molar fraction and HiTAC stands for High-Temperature Air Combustion [15]. From such a definition, the MILD regime can be easily identified with respect to the feeding conditions. However, it can be also inferred by internal (local) dilution and/or preheating through proper design of the chamber confinement in order to induce a massive internal recirculation [23–25]. Under MILD conditions, the oxidation process is mainly related to local ignition mechanisms due to the presence of hot gases/fresh reactants mixtures to locally obtain low oxygen levels. Furthermore, dilution prevents the stabilization of deflagrative/diffusive structures as a consequence of the occurrence of the self-ignition. Thus, several specific characteristics can be observed under such conditions: thermal and composition

homogeneity inside the combustor chamber, absence of a visible flame front (flameless), very low pollutants emissions (such as CO, NO_x and soot) and thermal load flexibility [26,27]. Therefore, this technology gives the opportunity to use a broad range of fuels, being a very good candidate for low-calorific-value [28], hydrogen-based and industrial fuels [29,30].

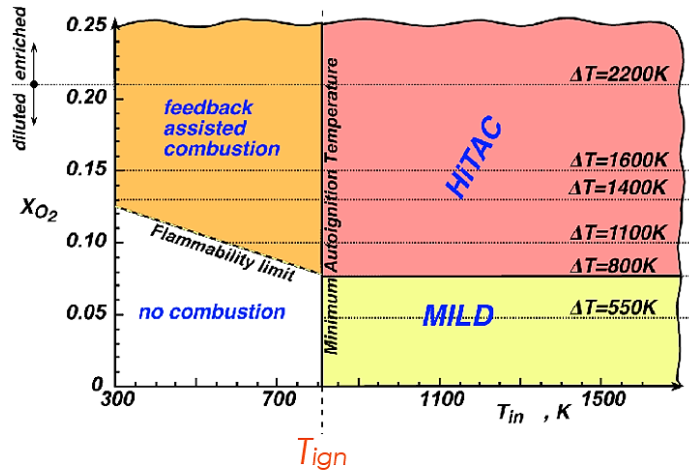


FIGURE 1.3 - CLASSIFICATION OF DIFFERENT COMBUSTION REGIMES ACCORDING TO CAVALIERE AND DE JOANNON [2].

In Figure 1.4, in order to better explain the meaning of flameless nature of the process and highlight the difference in respect to a traditional system, a burner operating under conventional and MILD conditions is shown.



FIGURE 1.4 - A BURNER OPERATING UNDER CONVENTIONAL (LEFT) AND MILD CONDITIONS (RIGHT) [3].

From the figure, it looks clear how the combustion processes occurring under MILD conditions differ from those involved in conventional systems. Such a difference lays on the strong interplay between mixing, chemistry and heat loss effects, as will be discussed in detail throughout this thesis work.

1.2.2 MILD SYSTEMS CLASSIFICATION

In the literature concerning MILD Combustion, several facilities such as the Adelaide and Delft Jet-in-Hot-Coflow (JHC) [31,32] and the Cabra flame [33], have been used to reproduce the conditions locally realized by means of diluted and preheated reactants. However, these configurations are only based on modifications of the kinetics time scales and their stabilization is achieved without significant flow convolutions. Moreover, in all these cases the combustion process is not confined and occurs far from the walls, allowing to assume nearly adiabatic conditions.

In contrast, in industrial applications, MILD Combustion is typically achieved through the strong recirculation of the burned products, which preheat and dilute the reactant mixture through internal [34,35] or external [36] exhaust gas recirculation (EGR) techniques. The internal EGR, in particular, is carried out by special designs of the feeding jets as well as of the combustion chamber. Practical solutions consist of both exploit internal aerodynamics of the reactor configuration and use high-momentum inlet jets [37]. Heat recovery by preheating the oxidant stream can also help to improve thermal efficiency and sustain the MILD regime [38]. MILD combustion burners are characterized by longer residence times with respect to traditional ones [39] and the high levels of flue gas entrainment and confinement [23] lead to chemical time scales comparable to the mixing ones [40]. Such aerodynamics constraints reflect the high relevance of tailored fluid/dynamics pattern such as impinging wall jets, revers and cavity flow zones [41,42]. The heat loss through the confinements also plays an essential role in the stabilization process, thus differentiating such category of MILD systems from those characterized by coflow-like facilities. Therefore, in confined systems, the recirculation of burned products is relevant because it induces local dilution of fresh reactants lowering system temperatures. It is usually defined through a recirculation ratio parameter. In particular, the systems based on recirculating flows

to preheat the reactants pose difficulties respect to the identification of MILD conditions. In fact, considering the reactants inlet conditions before the mixing with vitiated gases is not sufficient to describe the regime, as well as considering the reactants and recirculated gases to be perfectly premixed prior any reaction is also inaccurate.

One of the most comprehensive definitions for confined burners is that of Rao and Levy [4]. The diagram proposed by such authors, of which a version is shown in Figure 1.5, highlights the roles of inlet temperature of the reactants, the oxygen concentration and the recirculation ratio (as the concentration of diluent and combustion products). However, the depicted values are the only representative and can vary significantly depending on the specific application. The diagram is useful to figure out the difficulties in achieving the MILD/Flameless regime in several applications such as gas turbine combustors, as the degree of recirculation of exhaust and diluent species, required to achieve a very low concentration of O_2 , is significantly high [43].

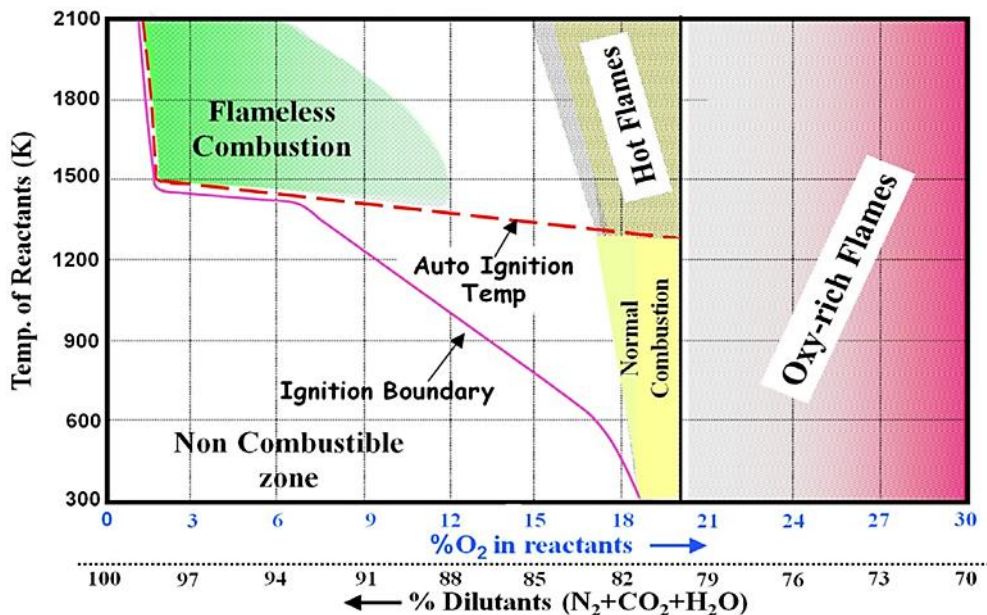


FIGURE 1.5 - COMBUSTION REGIMES DIAGRAM PROPOSED BY RAO AND LEVY [4].

Based on the constraints related to the attainment of the MILD regime in a confined system, different configurations can be identified and categorized. In general, such systems can be labelled as “MILD reactors”. A possible classification for MILD reactors can be carried out based on the MILD constraints about the local inlet temperature inside those systems T_{in} and the maximum temperature increase ΔT [22]: T_{in} must be higher than the ignition temperature T_{ign} and ΔT must be lower than T_{ign} itself, as shown in Figure 1.3. Therefore, in literature, three main categories of MILD reactors can be identified with respect to the strategy they use to fulfil the above-mentioned conditions.

The first configuration (category 1 in Table 1.1) includes reactors where both the conditions ($T_{in} > T_{ign}$ & $\Delta T < T_{ign}$) are satisfied through appropriate external feeding. The inlet vitiation and preheating of reactants guarantees MILD regime, in fact, have been exploited for reactors which could be considered post-combustion processes. Fuel-rich [44] or fuel-lean re-burning process [45,46] are examples of in-furnace and/or post-furnace NO_x abatement systems which use exhausts at low temperature with residual oxygen content. In other afterburning processes, the fuel is injected into an exhaust/oxygen mixture for jet engine systems [47] or waste incineration [48]. The low oxygen level infers a low-temperature increase, leading to intrinsically temperature uniformity.

The second design (category 2) is related to those systems where external feeding ensures high preheating levels whereas different intra-reactor (internal) processes are able to realize a local temperature increase higher than T_{ign} . This is the case of recuperative/regenerative furnaces [14,39,40,49,50] in which part of the heat released by combustion is taken away by the walls. In principle, this peculiar heat exchange arrangement can be obtained using any fluid-dynamic configuration, because it only relies on radiative heat exchange. However, in practice, the most used configuration is based on a strong interaction between the reactants stream and the reverse exhaust flows.

Finally, the third configuration (category 3) regards those systems where both MILD conditions ($T_{in} > T_{ign}$ & $\Delta T < T_{ign}$) are fulfilled by using internal recirculation and heat exchange strategies. In this case, proper fluid-dynamic arrangements are needed. Two

of them are extensively described in the literature: parallel jets with reverse flows [28,51,52] and toroidal or swirled flow configurations [17,23,53]. Both ensure long residence times of recirculated products in the combustion chamber. The former has also been used for burners in regenerative conditions (category 2) [14,39,49,50], whereas about the latter, a small-scale cyclonic burner [54], is a valuable example of a MILD reactor with a tailored flow-field.

The classification made is summed up in Table 1.1.

TABLE 1.1 - MILD REACTOR CATEGORIES: FEATURES AND REFERENCES.

CATEGORY	AERODYNAMICS CONFIGURATION	TECHNOLOGICAL APPLICATIONS	REF.
1	<ul style="list-style-type: none">- Coaxial Jets- Jet/swirl flows	<ul style="list-style-type: none">- Post-combustion and afterburning- Waste Incineration	[44–48]
2	<ul style="list-style-type: none">- Parallel Jets- Reverse Flow	<ul style="list-style-type: none">- Recuperative/Regenerative furnaces	[14,39,40,49,50]
3	<ul style="list-style-type: none">- Internal Flow- Reverse Flow- Cyclonic/Toroidal Flows	<ul style="list-style-type: none">- Boilers- Gas turbines	[17,23,28,51–54]

1.2.3 HEAT TRANSFER ROLE

MILD reactors that pertain to category 2 and 3 (see Table 1.1), are severely affected by the heat loss at walls. In fact, it reduces the mean temperature of the reacting mixture which, on the other hand, needs to be sufficiently high to guarantee the preheating of the reactants. In other words, the confinement is responsible for both the enthalpy loss by the combustion product and the heat gain by fresh reactants. In general, for such reactors, heat transfer is crucial in establishing the operating conditions.

As discussed above, in MILD combustion applications high internal or external recirculation of burned products is essential to put in contact with the fresh reactants both the inert flow, capable to lower reaction rates, and the heat needed to sustain the oxidation in diluted conditions. Thus, the design of the reactor, the feeding configuration and the flow velocities must improve the internal mixing and the convective heat transfer between fresh reactants and hot exhausts. Moreover, it is also important to consider the contribution of the radiative heat transfer. In fact, the high concentrations of the absorbing and emitting mixture $\text{H}_2\text{O}/\text{CO}_2$ inside the combustion chamber [55] lead to the enhancing of the radiative re-absorption (higher optical thicknesses) for MILD reactors. This effect is not negligible and contributes to the thermal homogeneity of the system. Such behavior is highlighted in several literature papers focused on the radiation modelling of Flameless combustion systems [56–58]. In Figure 1.6, the emissivities of CO_2 and H_2O as a function of the temperature at different products between pressure P and length of the enclosure L , adapted from Hottel [5], are reported.

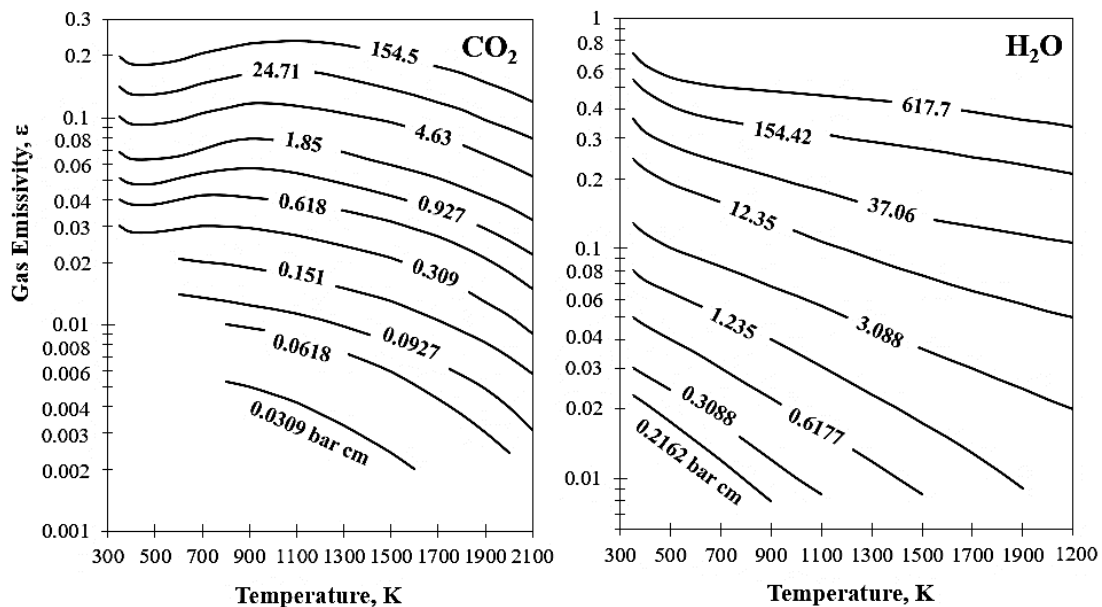


FIGURE 1.6 - TOTAL EMISSIVITY OF PURE CARBON DIOXIDE (LEFT) AND PURE WATER VAPOR (RIGHT) AS A FUNCTION OF TEMPERATURE, ADAPTED FROM [5] AND CONVERTED TO SI UNITS [59].

Those trends show that, for both species, when the temperature of the mixture gets lower, the emissivity increases. This result implies that for a MILD process, which usually presents moderate temperatures, the effect of the re-absorption is noticeable, even for a small-scale apparatus [57,58]. In [50], in particular, an estimation of the relative contributions of radiation and convection under MILD conditions was made, showing that the radiation contribution results to be greater.

For MILD reactors, moreover, the wall to wall heat transfer needs to be considered as well. In a black enclosure, radiative heat transfer depends only on the view factors and the surface temperatures. For a diffuse-gray enclosure, on the other hand, thermal radiation is also a function of the surface's emissivity [60]. Considering a gray and nearly opaque surface, it is easy to observe that part of the radiative heat transfer from gas to walls returns to gas, which means that a portion of the radiation emitted by the mixture to the walls is reflected and absorbed from the gas itself, result in making the thermal field more uniform. This effect is enhanced by the tendency of the system to behave as a blackbody cavity. In order to express this characteristic, the Gebhart factor [61] can be used. In fact, the radiative heat exchanged in an enclosure composed of surfaces with piecewise constant temperature and emissivity can be calculated in terms of Gebhart factors [62], G_{ij} , which are defined as a fraction of energy leaving surface i which reaches surface j and is absorbed. The Gebhart factors G_{ij} equals the view factors, F_{ij} , for black surfaces. Therefore, the net radiative heat exchange Q_k^{rad} between any surface k and all the others N surfaces of the enclosure can be expressed in terms of the Gebhart factors as

$$Q_k^{rad} = A_k \varepsilon_k \sigma \theta_k^4 - \sum_{j=1}^N A_j \varepsilon_j \sigma G_{ij} \theta_j^4 \quad (1.1)$$

where A_j , ε_j , θ_j , A_k , ε_k and θ_k are area, emissivity, and temperature of surface j and area, emissivity, and temperature of surface k , respectively [63].

For MILD reactors, which, as above mentioned, are usually closed and confined, the Gebhart factors related to the outlet section are usually lower than 0.1 [41,57,58]. Therefore, these systems tend to behave as a cavity with a maximization of the radiative re-absorption and ensuring higher and uniform wall temperatures.

1.2.4 MODELLING ISSUES AND STRATEGIES

Concerning the numerical modelling, the main issue regarding MILD combustion systems is the strong chemistry/fluid dynamic coupling. Indeed, in MILD reactors the dilution leads to higher chemical time scales whereas the high velocities lower the mixing ones. As a result, the two processes have comparable time scales [40], with the local Damköhler number that approaches unity [64,65]. This means that the numerical modelling of such systems must carefully consider the turbulence/chemistry interaction and detailed mechanisms must be used. Furthermore, recent Direct Numerical Simulation (DNS) studies have proved that both premixed and non-premixed modes exist in MILD combustion and that ignition is influenced by preferential diffusion effects whenever the fuel contains hydrogen [6,7,66]. In particular, several works in literature [66,67] analysed specific criteria to define MILD combustion in non-premixed condition by using the DNS of methane-diluted air established with internal exhaust gas recirculation. The studies revealed multiple coexisting and interacting reaction zones in MILD combustion which are extremely different from conventional combustion and highlight the role of the chemically active species. Minamoto et al. [6] carried out an adiabatic three-dimensional DNS of a CH₄/air partially premixed flame under MILD condition. Since the DNS of a complete EGR combustion system is not yet feasible because of heavy computational cost, the authors simulated the combustion phase after the resolution of the mixing phase by generating the initial and inflow fields. In order to account for EGR, they sent to the numerical cubic domain an exhaust stream together to the fresh mixture. In Figure 1.7, the numerical configuration and coordinates are shown. The normalized reaction rates of a temperature-based progress variable are reported as iso-surfaces. The flame shown in the figure has a unique shape compared to the conventional turbulent planar flames [68,69] and the presence of flame interactions is obvious. Moreover, due to the preheating temperature, regions of intense reaction rate are located not only in the middle of the computational domain but in the upstream and downstream regions as well. Such a study, therefore, underlines that the reaction under MILD condition occurs both in thin regions and in more distributed structure, due to flame–flame interaction, with a highly distributed heat released. Later works of the same group [70–74], focused on finding the best canonical reactor to address to the local MILD reactive

structure by means of *a priori* model testing and validation using DNS data. They found that the Flamelet predictions of reaction rate are poor, compared to the PSR, because they do not include the effects of flame interactions, which are abundant in the MILD combustion.

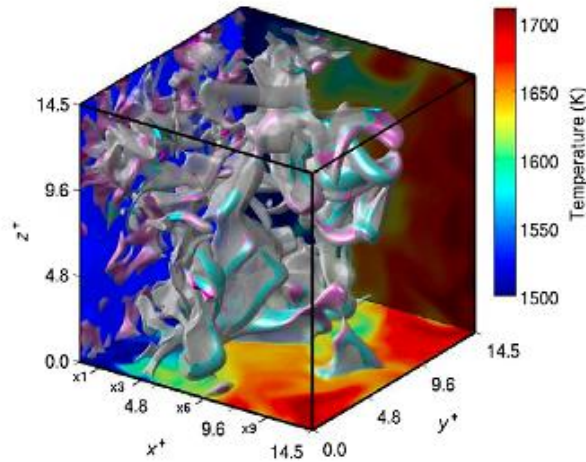


FIGURE 1.7 - ISO-SURFACES OF THE REACTION RATE AND X–Y, Y–Z AND Z–X PLANES OF TEMPERATURE FIELD. THE GRAY ISO-SURFACES CORRESPOND TO A REACTION RATE OF 0.7 WHEREAS THE COLOURED ONES TO 1.05, WHERE INTERACTING AND NON-INTERACTING LOCAL FLAME FRONTS ARE RESPECTIVELY DENOTED BY PURPLE AND LIGHT BLUE COLOURS [6].

As discussed in the previous paragraph (see [Paragraph 1.2.3](#)), in MILD reactors the heat transfer must be properly modelled. In particular, a suitable radiation model needs to be used. These features make the modelling of MILD combustion even more challenging and interesting for the scientific community. Although those systems have been successfully introduced in some industries, their broad implementation is hampered by a lack of fundamental insight into this combustion regime. The lack of understanding of MILD reaction zones also calls into question the common use of both Flamelet-like and non-Flamelet-based turbulent combustion models for Reynolds-averaged Navier-Stokes (RANS) equations [75] and for Large Eddy Simulations (LES) [16]. In this framework, affordable modelling tools based on reduced-order techniques are essential for the design and development of new concepts and

prototypes in the context of Digital Twin with application in monitoring, diagnostics and prognostics [76].

The need to use detailed kinetic mechanisms under MILD combustion regime was assessed in several works [77–79]. However, the inclusion of detailed chemistry effects requires increasing CPU resources. In the last few years, several of the most used approaches to model MILD systems were based on tabulated chemistry techniques [80,81]. Such models are chemistry reduction methods which allow using detailed kinetic mechanisms saving the computational cost. A considerable number of works considered such an approach as a valuable tool for the simulation of reactors with internal recirculation, through the tabulation of Flamelets [57,82] or homogeneous reactors [83]. Among the former, the Flamelet Generated Manifold model (FGM) [84,85] is one of the most used and promising. It is a chemistry reduction method that combines the advantages of dimension reduction techniques based on chemical steady-state assumptions and Flamelet models. In MILD context, several works [86,87] have already considered the Flamelet approach as a valuable tool for the simulation of a MILD combustion system. Recently, Abtahizadeh et al. [87] showed that the elementary configuration used for the tabulation strongly influences the representation of MILD combustion in Jet in Hot Coflow (JHC) configurations. A relevant challenge in Flamelet approach is to include the effects related to recirculated burned gas in the look-up tables to properly represent the dilution and heat loss effects [80]. This is a very demanding task that leads to expensive CFD simulations to the increased manifold dimension. That is the case of Huang et al. [88], which used FGM to characterize a MILD combustion lab-scale furnace adopting a 6D turbulent manifold, tabulating counterflow structures. Another possibility for the tabulated chemistry model is to use a homogeneous reactor instead of Flamelet. Chen et al. [83,89] modelled partially premixed combustion cases by tabulating the chemistry with a 0D Perfectly Stirred Reactor (PSR) configuration. Within the MILD combustion framework, however, the choice of the ideal configuration (Flamelet or not) able to locally reproduce the MILD combustion conditions still represents an open issue.

On the other hand, reaction rate-based approaches have been also proposed in the literature and applied to MILD conditions. Among them, it is worth to mention the Eddy Dissipation Concept (EDC) [90], which divides each grid cell into two regions:

the fine structures, modelled as Perfectly Stirred Reactors and the surrounding fluid mixture. Partially-Stirred Reactor (PaSR) model, originally proposed by Chomiak [91] is a modification of EDC and is characterized by a different definition of the reacting volume fraction, which turns in the ratio between kinetic time scale and the sum of mixing and chemical scales. It has been used to model the Adelaide Jet in Hot Co-flow (JHC) by Ferrarotti et al. [92]. In literature, there are works comparing EDC to tabulated chemistry models for the same MILD configurations [93]. However, the results showed that even the PaSR modelling paradigm needs modifications in case of MILD conditions, thus indicating that still no numerical solutions have been pointed out for such a regime. These numerical solutions may probably be also dependent on the way the competition between chemistry and turbulence is achieved, thus further motivating the activity carried out in the present PhD thesis.

Over the last years, JHC-like systems have been largely used to successfully assess different modelling strategy for MILD conditions [89,94–96]. Despite that, the MILD reactors, where the burned gas recirculation strongly influences the mixing and chemical timescales, are still far to be effectively simulated (and well understood). In fact, in addition to the effect of the dilution on the reactivity, the heat transfer mechanisms must be properly modelled as well, including the radiation. To model gas re-absorption, the dependence of the exhausts radiative properties on the wavelength must be known. The most accurate method for calculating the radiative properties of the combustion products is the Line-by-line integration [97] which uses spectroscopic databases [98–100]. The databases contain a set of spectral line parameters required to calculate spectral absorption coefficient for specified spectral location. However, line-by-line calculations are not practical for engineering purposes and, therefore, for computational fluid dynamics (CFD) models, the spectral variation of the gases is commonly neglected and the spectrum is treated by a single average, i.e. by a gray approximation [75,101,102]. Nowadays, the most common approach is to exploit the detailed spectral databases available and compute the gray gas absorption coefficient as an average of the spectral absorption coefficients weighted by the blackbody emission fractions at the respective wavelength [103]. In particular, the HITEMP2010 database, which has been reported in [98,100,104], provide the most accurate results if compared to other available databases. In order to predict in an affordable way the

radiative re-absorption in MILD reactors, the Weighted-Sum-of-Gray-Gases Model (WSGGM) [105] is usually adopted to model the spectrally dependent properties of the combustion gases, making use of updated spectral databases. The basic assumption of the WSGGM is that the total emissivity of a given non-gray gas can be presented as the sum of the emissivities of a given number of gray gases. Recently, a modified weighted-sum-of-gray-gases (WSGG) model [106] with four gray gases and one clear gas was developed. In particular, the coefficients proposed in this model were used to account for various temperature and various relative concentrations between H₂O and CO₂ in each computational cell. Another interesting modification of the WSGG model is represented by the Spectral Line Weighted sum of gray gases, SLW [107]. According to this approach, the black body and absorption coefficients of the generic fictitious gray gas are calculated using detailed gas spectroscopic data captured by a designed distribution function [108]. These modifications of the WSGG model represent useful modelling options for the simulation of radiation in practical combustion applications, being a reasonable compromise between the oversimplified gray-gas model and a detailed line by line calculation. Finally, about the resolution of the Radiative Transfer Equation (RTE) [109], the Discrete Ordinate Method (DO) [99] seems to be the most reasonable choice for MILD reactors, due to its applicability to a large range of optical thickness. This model allows solving the RTE for a set of discrete directions spanning a full sphere around their origin. The resolution of the RTE along each direction yields differential equations in terms of the new directions [110].

1.3 Objectives and Outline of the thesis

The main objective of this thesis is to shed light on the reactor and thermochemical features of MILD Combustion systems. In particular, the author intends to highlight which are the parameters and the mechanisms responsible for the establishment and the stabilization of the MILD conditions. Such a target, in fact, represents a key factor in order to favor the future development of these systems on a large scale. To achieve this result, both experimental and numerical activity has been performed. By adopting a tabulation of the chemistry by means of ideal configurations, the author wants to reproduce the mean conditions inside a MILD reactor, defining which reasonable

approximations regarding turbulence, kinetics and heat transfer can be assumed for modelling such a regime. The combined experimental and numerical work, therefore, is intended to identify the sensitivity of these systems to both design and operational parameters and to define the most adequate strategies for the creation of the manifolds in the tabulated chemistry context.

In the following chapter (see [Chapter 2](#)), the test case chosen is presented and described in detail. In particular, a cyclonic configuration is considered in order to emphasize the effect of the internal EGR of such systems. Afterwards, in [Chapter 3](#), each step of the CFD model based on tabulated chemistry used to treat the turbulence/chemistry interaction is analyzed and described. Then the comparisons between measured and simulated quantities are carried out (see [Chapter 4](#)) for different operating conditions. Finally, a new tabulating strategy is presented and a reactor analysis is conducted in order to define dimensional reduced manifolds which describe the mean MILD reactors conditions in a proper way (see [Chapter 5](#)).

Finally, the main conclusions and findings of this study are summarized and suggestions and recommendations for future studies are reported in [Chapter 6](#).

Chapter 2

Experimental test case

In this chapter, the test case object of the study is presented. It falls within the category of MILD reactors, introduced in [Chapter 1](#). First, the experimental apparatus is described in detail (see [Section 2.1](#)). Then, the operational parameters regarding the inlet conditions which can be ranged in such a system are defined (see [Section 2.2](#)). Afterwards, the measurement techniques are reported and the uncertainties regarding the evaluation of the temperature inside the combustion chamber are discussed (see [Section 2.3](#)). Finally, the main mechanisms governing the heat transfer in this system (see [Section 2.4](#)) and its peculiar thermal uniformity (see [Section 2.5](#)) are addressed.

2.1 Cyclonic chamber

The Laboratory Unit CYclonic (LUCY) burner considered in this study is shown in Figure 2.1, where both a picture (at left) and a sketch (at right) are reported.

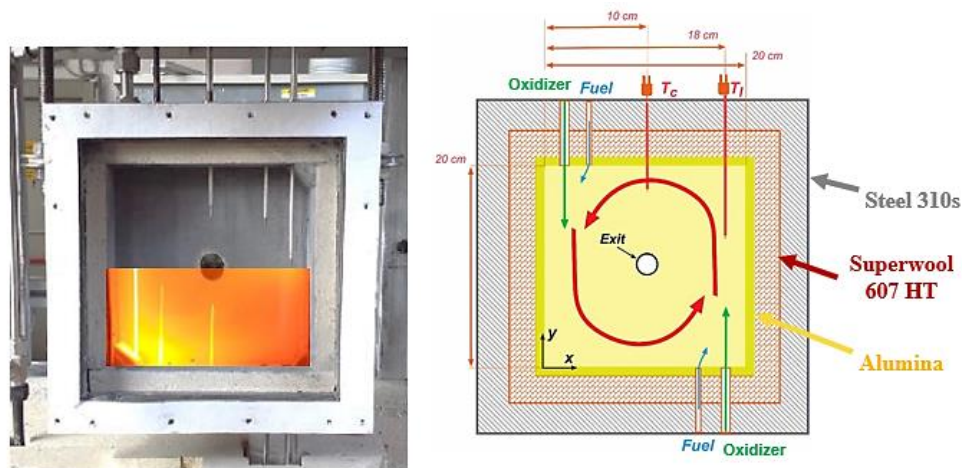


FIGURE 2.1 – PICTURE OF THE MIDPLANE SECTION OF THE CYCLONIC BURNER UNDER FROZEN (TOP) AND MILD (BOTTOM) CONDITIONS AT LEFT; SKETCH OF THE CYCLONIC CHAMBER, THE FEEDING SYSTEM, THE MOVABLE THERMOCOUPLES AND THE MATERIALS AT RIGHT.

The apparatus was designed and built in the laboratories of the Institute of Research on Combustion (IRC) of the National Research Council (CNR) of Naples [23,111]. It was already used, in the past, to characterize the occurrence of MILD Combustion [23,54,57,111]. Such a system lays under the definition of MILD reactor given in the first chapter, and, in particular, it refers to the category 3, where the Flameless conditions ($T_{in} > T_{ign}$ & $\Delta T < T_{ign}$) are fulfilled by means of high levels of internal EGR (see Table 1.1). The burner is based on a cyclonic flow configuration which is due to the geometry of the chamber and the position of the inlets. In Figure 2.1, a picture and a sketch of the frontal view at the midplane section (2.5 cm from the bottom) are reported. The LUCY burner consists of a prismatic chamber with a square section of $20 \times 20 \text{ cm}^2$ and a height of 5 cm. It is fed with two pairs of coaxial oxidant/fuel jets placed in an anti-symmetric configuration thus realizing a centripetal cyclonic flow field. The oxidant injector is located at 2 cm from the lateral wall, whereas the fuel injector is at 4.5 cm. The round section outlet is placed at a central position, perpendicular to the frontal view. The combustor chamber walls have a three layers structure: a 0.5 cm thick inner shell of alumina (99.7% Al_2O_3); a 1.5 cm thick layer of heat-insulating material, the Superwool 607 HT; and a 1.5 cm thick outer shell of stainless steel 310s. The inner and outer layer are shown in detail in Figure 2.2.

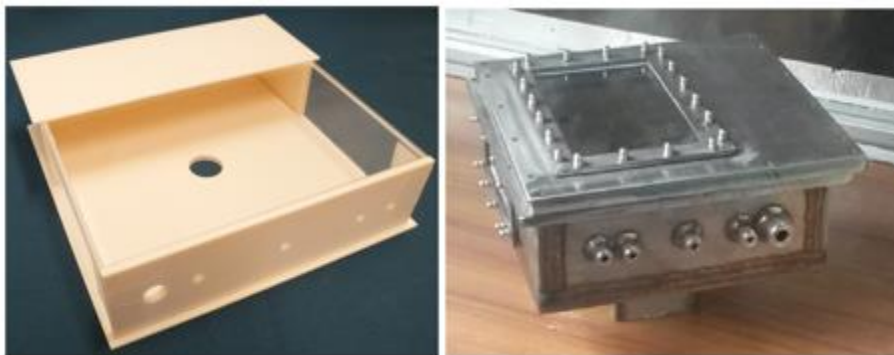


FIGURE 2.2 – INNER ALUMINA LAYER (LEFT) AND OUTER STEEL CASE (RIGHT) OF THE CYCLONIC CHAMBER

The cyclonic burner is equipped with a set of thermocouples (type N) and optical accesses (quartz windows). The quartz windows position is shown in Figure 2.2. At the left side of Figure 2.1, moreover, a view of the cyclonic chamber under MILD regime, through the quartz window at the frontal position, is reported. The two type N-thermocouples located at the midplane, depicted in Figure 2.1, can be moved along the y-direction. The lateral one, placed at 2 cm from the wall along the oxidizer inlet position, monitors the temperature T_l while the central one, located at the centerline of the combustion chamber, reads the temperature T_c .

2.2 Operative parameters

The LUCY burner is located within an electrically heated ceramic oven. The main oxidizer stream passes through heat exchangers which are placed within the electrical ceramic fibre heaters to increase the inlet temperature to the desired values (T_{in}). Therefore, both preheated and non-preheated conditions can be obtained. In Table 2.1, all the external operational parameters regarding the feeding conditions and the operating ranges are reported.

TABLE 2.1 - LIST OF THE EXTERNAL OPERATIONAL PARAMETERS AND THEIR OPERATING RANGES.

PARAMETER	DESCRIPTION	OPERATING RANGE
T_{in}	Preheating temperature of the oxidizer	300 (Ambient) ÷ 1300 K
d	External dilution level	71.48 (air) ÷ 98
Φ	Equivalence ratio	0.05 ÷ 5
τ	Residence time	0.1 ÷ 5 s
P	Thermal power	0.3 ÷ 15 kW

The oxidizer stream is composed of oxygen and diluent and flows in the chamber at T_{in} , which is an operating parameter that can be controlled by the heaters, whereas the fuel stream is fed at environmental conditions. The pressure is fixed at 1 bar. The

external dilution level is accounted by defining a parameter d for the oxidizer inlet mixture, which reads

$$d = \frac{mol_D}{mol_D + mol_{O_2} + mol_F} \cdot 100 \quad (2.1)$$

Where mol_D , mol_{O_2} and mol_F are the overall inlet moles of diluent, oxygen and fuel, respectively. The global equivalence ratio Φ is defined as

$$\Phi = \frac{mol_F / mol_{O_2}}{(mol_F / mol_{O_2})_{st}} \quad (2.2)$$

where the subscript st stands for stoichiometric condition. Finally, the residence time τ and the nominal thermal power P of the system are expressed by the following equations

$$\tau = \frac{V}{\dot{m}} \quad (2.3)$$

$$P = \dot{w}_F H_i \quad (2.4)$$

where V is the volume of the chamber, \dot{m} is the overall inlet volumetric flow rate, \dot{w}_F is the mass flow rate of the fuel and H_i is the fuel lower heating value.

2.3 Measurements and uncertainties

The thermocouples system is depicted in detail in Figure 2.3. The movable N-thermocouples, introduced in the first section, read the temperature profiles T_c and T_l . Furthermore, a set of fixed N-thermocouples placed on the inner alumina wall and at the outlet section, are used as well. The thermocouples on the wall, in particular, evaluate the inner wall temperature, T_w , and, together with other thermocouples placed on the outer steel case, allow estimating the global heat loss flux from the system, Q_w . Such a value is also confirmed by the global enthalpy balance carried out by measuring the temperature at the outlet, T_{out} .

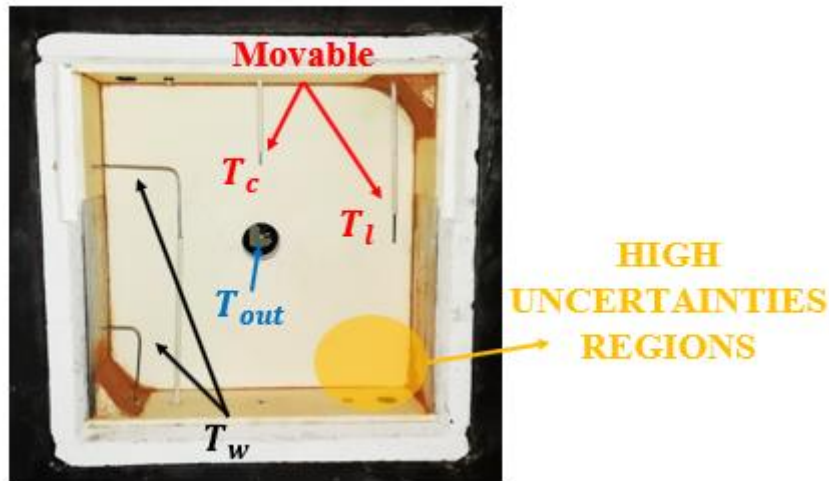


FIGURE 2.3 – THERMOCOUPLES SYSTEM

The uncertainties regarding the temperature measurement are experimentally obtained by monitoring the gas temperature through the thermocouple for 5 minutes in each case. Therefore, the average value is evaluated and both the minimum and maximum deviations from it are reported. The yellow areas in Figure 2.3 show the maximum uncertainties. These systematic errors are due both to the strong turbulent mixing between the fresh mixture and recirculating exhausts (convective effect) and to the radiative flux coming from the walls and the combustion products at high temperature (radiative effect). In order to separate such effects, the convective part of the uncertainty is evaluated under non-preheated and non-reacting conditions at ambient temperature (heaters off). In this case, the wall radiative effects are minimized and therefore the temperature errors are mainly due to perturbations of the thermocouple due to the flow-field. On the other hand, the uncertainty related to radiation is estimated from a steady-state energy balance on the thermocouple bead surface area, by neglecting conduction. The actual gas temperature, T_g , determined from the measured temperature, T_{tcb} , reads

$$T_g = T_{tcb} + \frac{\sigma \varepsilon_{tcb} (T_{tcb}^4 - T_w^4)}{h} \quad (2.5)$$

where ε_{tcb} is the thermocouple bead surface emissivity, σ is the Stefan-Boltzmann constant, T_w is the averaged surface temperature of the walls, and h is the convection coefficient calculated for a sphere. This approach leads to a maximum correction of

about 6% of the measured value due to radiation (in the yellow regions of Figure 2.3). In particular, the systematic errors related to the lateral thermocouple are ± 2 and $\pm 6\%$ of the mean value for convection and radiation, respectively. On the other hand, the uncertainties related to the central measurements are about $\pm 1\%$ for convection and $\pm 1.5\%$ for radiation. Such results are consistent with the uncertainties experimentally evaluated.

TABLE 2.2 OPERATING CONDITIONS TEST CASE FOR UNCERTAINTIES ANALYSIS.

T_{in}, K	Diluent	Fuel	d	Φ	τ, s	P, kW
1125	N ₂	C ₃ H ₈	94	1	0.2	2

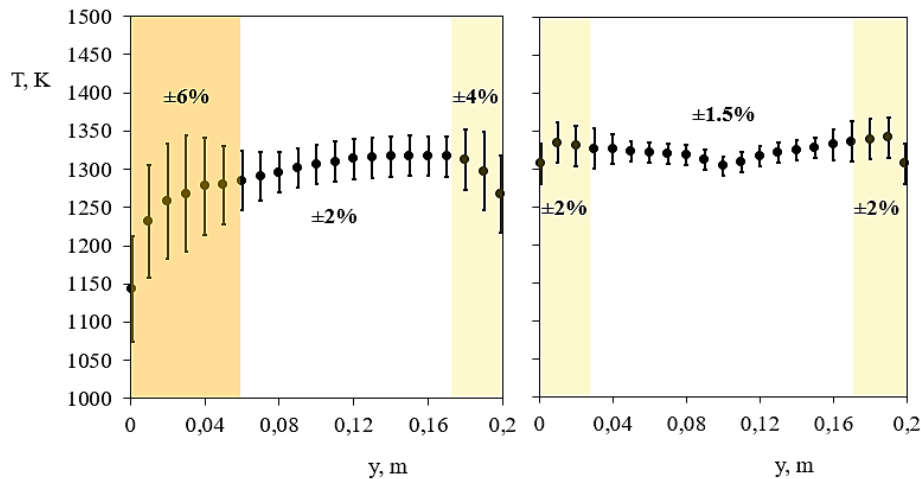


FIGURE 2.4 – MEASURED TEMPERATURE PROFILES TL (LEFT) AND TC (RIGHT) WITH THE RELATIVE UNCERTAINTIES UNDER A MILD CONDITION SAMPLE CASE.

In Figure 2.4, the lateral (T_l) and central (T_c) temperature profiles with the evaluated uncertainties for the MILD condition case reported in Table 2.2, are depicted. The experimental uncertainties, depicted as error bars, will be reported throughout this thesis from now on.

The exhausts were monitored at the exit of the combustion chamber through a water-cooled probe and the major species emissions (such as CO, CO₂ and H₂) were analyzed by means of a Gas Chromatograph (GC) analyzer.

2.4 Dominant heat transfer mechanisms

In order to identify the mechanisms governing the heat transfer inside the LUCY burner, the following considerations can be done.

In general, inside a combustion chamber the heat exchange between reacting mixture and walls, Q , can be expressed as the sum of a convective, Q_c , and a radiative term, Q_r , as

$$Q = Q_c + Q_r \quad (2.6)$$

where the convective and radiative terms read

$$Q_c = h_f(T_f - T_w) \quad (2.7)$$

$$Q_r = \varepsilon_g \sigma (T_g^4 - T_w^4) \quad (2.8)$$

where h_f is the average convection heat transfer coefficient over the heat transfer area, T_w the wall surface temperature, T_f the local near-wall fluid temperature, T_g and ε_g are the exhaust mixture H₂O/CO₂ mean temperature and emissivity, respectively [112]. For a MILD reactor, T_f can be approximated to the mean gas temperature inside the combustion chamber, T_g , because of the absence of steep gradients and peaks of temperature [41,57,58]. Doing this approximation, in order to compare the heat transfer contributions for those systems, the ratio between radiative and convective terms can be expressed as

$$\frac{Q_r}{Q_c} = \frac{\varepsilon_g \sigma T_w^3}{h_f} \left(\left(\frac{T_g}{T_w} \right)^2 + 1 \right) \left(\frac{T_g}{T_w} + 1 \right) \quad (2.9)$$

Therefore, it can be assumed that such a relation approximates the thermal behavior of each system operating as MILD reactor. Considering the case reported in Table 2.3, the equation 2.9 is applied in order to calculate the convective and radiative contributions under MILD conditions for the cyclonic burner.

TABLE 2.3 OPERATING CONDITIONS TEST CASE FOR HEAT TRANSFER ANALYSIS

T_{in}, K	Diluent	Fuel	d	Φ	τ, s	P, kW
1000	N ₂	CH ₄	71.48	1	1	2

In Figure 2.5, Q_r/Q_c for CO₂ and H₂O as a function of the gas temperature T_g , at different wall temperatures T_w (solid black lines) is depicted. The gas emissivity $\epsilon_g(T_g)$ is read from Hottel diagrams (see Figure 1.6). For the case reported in Table 2.3, a mean convective coefficient of 35 W/m²K is estimated, whereas T_g and T_w are the mean temperature measured by movable and fixed thermocouples, respectively.

For the considered case, the steady and stabilized MILD condition operating point is localized in the red regions of the Figure, where the radiative heat transfer between gases and walls is around 1.5 times the convective one, for both the combustion products. Therefore, for the cyclonic burner under MILD conditions, the radiative heat transfer plays a dominant role. In particular, the temperature of the walls appears to be essential to move from a convective-based to a radiative-based heat transfer mode. The latter, characterized by higher T_w , favors the stabilization of MILD conditions, as well proved by [41] by controlling the heat flux distribution at walls.

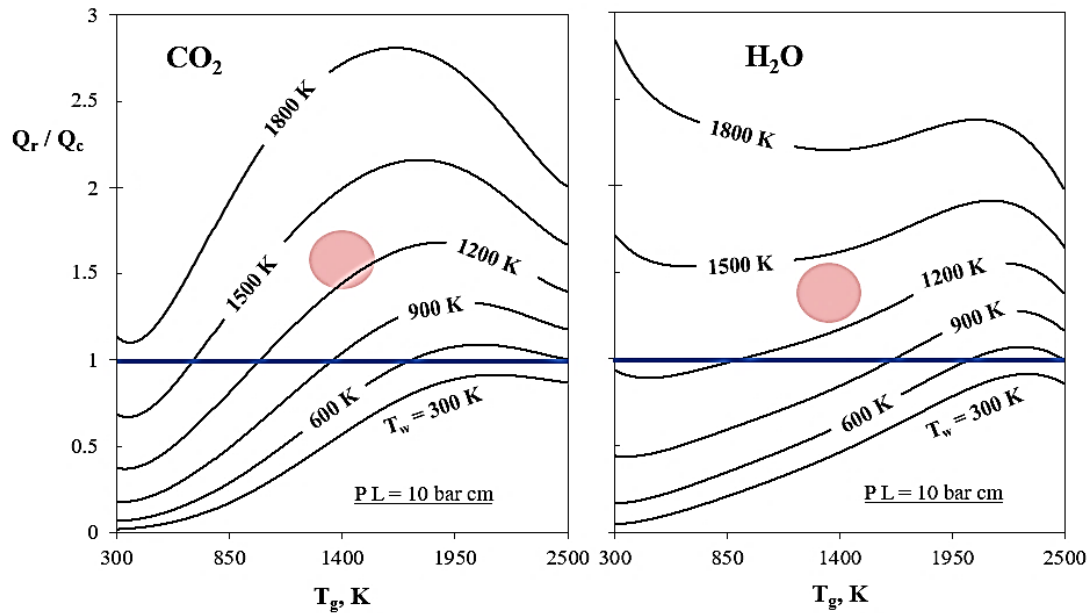


FIGURE 2.5 - RATIO BETWEEN RADIATION AND CONVECTION HEAT FLUX FOR CO₂ (LEFT) AND H₂O (RIGHT) AS A FUNCTION OF THE MEAN GAS TEMPERATURE AND AT DIFFERENT WALL TEMPERATURES AND OPERATING POINTS UNDER MILD CONDITION FOR LUCY BURNER (RED AREA).

The analysis carried out can be easily replicated for other operating conditions and for different MILD reactors with a large amount of internally recirculating combustion products [41,50,56,58,88].

2.5 Thermal uniformity

The thermal homogeneity consists in a tendency of the system to present a large-scale uniformity of the sensible enthalpy field (small temperature gradients). In general, the thermal uniformity of a combustion system can be characterized by a parameter T_u , defined by Cho et al. [113] as

$$T_u = 1 - \sqrt{\frac{1}{N} \sum_{i=1}^N \frac{(T_i - T_{mean})}{T_{mean}}} \quad (2.10)$$

Where T_i is the measured temperature at certain location i , N is the total number of locations and T_{mean} is the averaged value of all measured locations in the burner. The value of the T_u varies between 0 and 1, where 1 indicates a perfectly uniform temperature field.

The smoothness of the temperature field is a key feature of a MILD reactor. It is related both to the low heat released by the reaction due to dilution and to the radiative transfer between reacting mixture and walls. The temperature measurements inside the cyclonic chamber confirm such behavior. In Table 2.4, T_u is reported for several operating conditions of the LUCY burner.

TABLE 2.4 THERMAL UNIFORMITY EVALUATED INSIDE THE CYCLONIC CHAMBER FOR DIFFERENT OPERATING CONDITIONS.

T_{in}, K	Diluent	Fuel	d	Φ	τ, s	P, kW	T_u
1000	N ₂	CH ₄	71.48	1	1	2	0.96
1000	N ₂	CH ₄	80	1	0.75	2	0.97
1000	N ₂	CH ₄	90	1	0.36	2	0.98
300	N ₂	CH ₄	71.48	1	3.38	2	0.92

It is worth noting that T_u is higher than 0.95 for the conditions with preheating of the inlet oxidizer stream at 1000 K, whereas it is only slightly lower for the non-preheated case (0.92). This means that the cyclonic temperature uniformity under MILD regime is not severely affected by the inlet conditions because of a number of effects which tend to stabilize the system:

- The elevated recirculating flow rate of the combustion products (entrainment);
- The radiative heat transfer between exhausts and walls at high temperature (cavity effect);
- The radiative re-absorption of the mixture $\text{CO}_2/\text{H}_2\text{O}$ (optical thickness).

Chapter 3

Numerical methods

In this chapter, the numerical methodology considered to simulate the MILD combustion conditions in the LUCY burner (see [Chapter 2](#)) is presented in three main sections. In the first one (see [Section 3.1](#)) the turbulence-chemistry interaction model based on chemistry tabulation is described. Then, the CFD details and assumptions regarding computational grid, turbulence model and treatment of the heat transfer are reported (see [Section 3.2](#)). Finally, the coupling between the tabulated model and the CFD solver is shown and discussed (see [Section 3.3](#)).

3.1 Flamelet Generated Manifolds

In this Section, the approach used in this thesis work to model the strong turbulence-chemistry interaction of the LUCY burner is described in detail. First, the main assumptions of the model are introduced (see [Paragraph 3.1.1](#)). Afterwards, the configurations used to solve the chemistry with detailed mechanisms are described (see [Paragraph 3.1.2](#)). Lastly, the tabulation technique is presented (see [Paragraph 3.1.3](#)).

3.1.1 BASIC PRINCIPLES AND OPERATIONAL STEPS

The first concept of Flamelet Generated Manifold model is that a turbulent flame can be assumed as an ensemble of 1D laminar flames [114]. In Figure 3.1 this statement is illustrated using a 2D DNS solution from [7]. The black thick curve perpendicular to the isoline of a mixture fraction Z , a conserved scalar representative of the mixing between oxidizer and fuel (see [Paragraph 3.1.3](#)), is drawn at the left side of the Figure, whereas the correspondent profile along Z of the molar fraction of H_2 is reported at right. It is worth noting that the extracted data exhibits quite a 1D behavior, which supports the Flamelet assumption.

The second idea in FGM is that in a combustion system, the N-dimensional composition space, composed of the molar (or mass) fractions of the species and the enthalpy, can be represented with a lower N-M dimensional manifold [115]. The coordinates of the composition space, in fact, according to FGM, can be assumed as a function of a few controlling variables allowing the manifold reduction. The choice of which and how many controlling variables to consider, therefore, represents a key point for the modelling of the given combustion system. Usually, for a non-premixed configuration, two variables are chosen: one representing the mixing between fuel and oxidizer; and the other representative of the progress of the reaction.

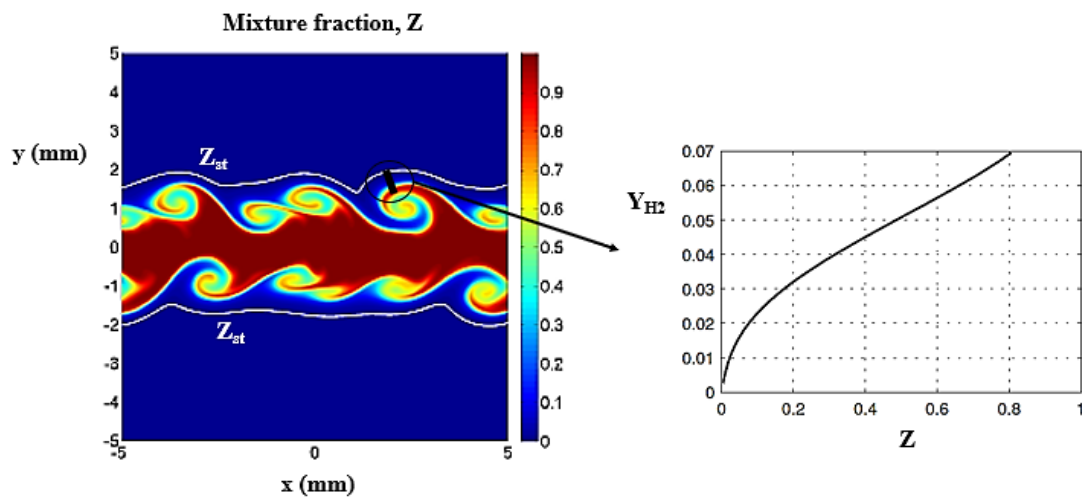


FIGURE 3.1 - DISTRIBUTION OF MIXTURE FRACTION IN A 2D DNS CALCULATION FROM [7] (LEFT) AND DISTRIBUTION OF HYDROGEN MOLAR FRACTION ON THE FLAMELET EXTRACTED FROM THE THICK BLACK CURVE (RIGHT).

Depending on the configuration of the combustion system to be modelled, other controlling variable might be needed such as enthalpy, pressure, others progress variables and internal dilution. In order to generate the manifolds, the 1D Flamelet equations are solved and all thermochemical variables are stored in so called look-up tables as functions of controlling ones. The choice of the canonical flame configuration is another key point which depends on the type of process to simulate. Once the look-up tables are created, the transport equations for the controlling variables are solved and all the required variables are retrieved from the tables.

Therefore, FGM allows to avoid the resolution in the CFD run-time of the transport equations of all the species involved, where the related source terms are calculated for each reaction from the chemical reaction mechanism. In fact, only the transport equations for the controlling variables need to be solved and the source terms are looked up from the tables. As a result, the required computational time is reduced by orders of magnitude keeping an acceptable prediction accuracy if the Flamelet configuration and the controlling variables are correctly chosen.

To summarize, there are three basic steps in the implementation of FGM model:

- The resolution of the 1D flame equations either in Flamelet or in space and time coordinates;
- The storage of all the relevant thermo-chemical variables from the Flamelet equations resolution into FGM tables as functions of few controlling variables;
- The calculation, during the run-time, of the controlling variables transport equations, and the retrieving of the required thermo-chemical variables from the look-up tables.

3.1.2 FLAMELET EQUATIONS

In this study, two different 1D Flamelet configurations are investigated: The Igniting Mixing Layer (IML) [57,87,116] and the steady premixed flame [84,85]. In Figure 3.2, the temperature profiles along the spatial coordinate s for the stoichiometric air/methane mixture and both the configurations are depicted. IML (left side of the Figure) is an unsteady non-premixed configuration where fuel and oxidizer, completely separated at the initial time ($t = 0$), mix and react in time ($t > 0$). This 1D flame is similar to the commonly used Igniting Counter Flow (ICF) diffusion Flamelet except for the initial condition and inflow momentum. In fact, for ICF, a steady-state mixing field is reached before any chemical reaction takes place. This assumption is mainly valid if the time scale of mixing is much shorter than the chemical time scales. Such an assumption, as discussed in [Section 1.2](#), cannot be accepted for a strong diluted MILD condition. Therefore, IML is a time dependent ignition-diffusion layer, evolving from an initial unmixed state. Such an unmixed profile is adopted to include diffusive effects in the pre-ignition stage. In this situation, the initial thermo-chemical properties have a step-function profile in physical space with fuel at one side of the

domain and oxidizer at the other. The scalar dissipation rate, thus, is initially very large and decreases during the molecular mixing process, when the chemical reactions can start at any time.

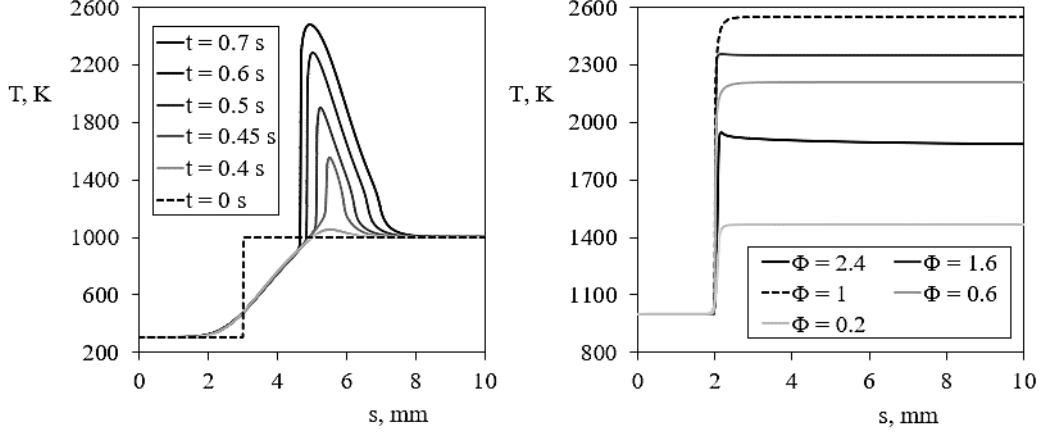


FIGURE 3.2 - TEMPERATURE EVOLUTIONS ALONG THE SPATIAL COORDINATE, IN TIME FOR AN IGNITING MIXING LAYER CONFIGURATION (LEFT), AND AT DIFFERENT COMPOSITIONS FOR A PREMIXED FLAME (RIGHT). FOR BOTH CONFIGURATION THE STOICHIOMETRIC AIR/METHANE CASE WITH THE C1C3 KINETIC MECHANISM [8] IS REPORTED.

Thus, in the IML Flamelet, the gradient of the mixture fraction is not enforced by an inflow momentum (i.e. an applied strain) and it is governed purely by molecular diffusion. The transport equations that describe a one-dimensional unsteady counterflow are given by [117]

$$\frac{\partial \rho}{\partial t} + \frac{\partial \rho u}{\partial x} = -\rho G, \quad (3.1)$$

$$\rho \frac{\partial Y_i}{\partial t} + \rho u \frac{\partial Y_i}{\partial x} - \frac{\partial}{\partial x} \left(\rho U_i \frac{\partial Y_i}{\partial x} \right) = \dot{\omega}_i, \quad (3.2)$$

$$\rho \frac{\partial h}{\partial t} + \rho u \frac{\partial h}{\partial x} - \frac{\partial}{\partial x} \left(\frac{\lambda}{C_p} \frac{\partial h}{\partial x} \right) = \frac{\partial}{\partial x} \left(\sum_{i=1}^{N_{sp}} h_i \left(\rho Y_i U_i - \frac{\lambda}{C_p} \frac{\partial Y_i}{\partial x} \right) \right), \quad (3.3)$$

where ρ , C_p and λ stand for mass density, specific heat at constant pressure and thermal conductivity, respectively. U_i represents the diffusion velocity u the velocity

x direction. Y_i and $\dot{\omega}_i$ are the mass fraction and the chemical production rate ($\text{kg}/\text{m}^3\text{s}$) of the i^{th} species where i ranges from 1 to N_{sp} , the total number of species. The momentum balance is modelled through solving a transport equation for the tangential velocity gradient or strain rate, G [117]:

$$\rho \frac{\partial G}{\partial t} + \rho u \frac{\partial G}{\partial x} - \frac{\partial}{\partial x} \left(\mu \frac{\partial G}{\partial x} \right) = J - \rho G^2, \quad (3.4)$$

where μ is the viscosity and $J = \rho_{ox} a^2$, with a being the applied strain rate and ρ_{ox} the density at the oxidizer side. The computational time is set to 1 s within which the flame attains a near steady-state. In practice, for an IML configuration is achieved by solving the equations from 3.1 to 3.4 with a low the applied strain rate ($a = 10 \text{ s}^{-1}$), using as initial condition a steady counterflow with no reaction and $a = 10^4 \text{ s}^{-1}$ (dashed line at left side of Figure 3.2), as reported in [116]. IML was already used for the cyclonic burner modelling through FGM in previous works [57,118] since it reproduces the non-premixed feeding system.

At the right side of Figure 3.2, the temperature profiles for the 1D steady premixed flame are reported. In this case, the Flamelet equations are solved for different compositions (different equivalence ratios Φ) [85]. In such a case, the equations read

$$\frac{\partial \rho u}{\partial x} = 0, \quad (3.5)$$

$$\rho u \frac{\partial Y_i}{\partial x} - \frac{\partial}{\partial x} \left(\rho U_i \frac{\partial Y_i}{\partial x} \right) = \dot{\omega}_i, \quad (3.6)$$

$$\rho u \frac{\partial h}{\partial x} - \frac{\partial}{\partial x} \left(\frac{\lambda}{C_p} \frac{\partial h}{\partial x} \right) = \frac{\partial}{\partial x} \left(\sum_{i=1}^{N_{sp}} h_i \left(\rho Y_i U_i - \frac{\lambda}{C_p} \frac{\partial Y_i}{\partial x} \right) \right). \quad (3.7)$$

Although the burner has a non-premixed inlet configuration, the high internal recirculation due to the cyclonic flow leads to a rapid mixing between the inlet jets, explaining the choice of the authors to investigate the premixed configuration as well. Moreover, it can be argued that the use of homogeneous reactors would be a better option considering the high mixing levels inside the cyclonic chamber. However, the preignition chemistry takes place as the streams start to mix and such an effect cannot be captured with 0D models.

In this thesis work, the 1D Flamelet equations in spatial and temporal coordinates (see Equations 3.1-3.7) are solved using an in-house code developed at the University of Technology of Eindhoven (TU/e), called Chem1D [119].

3.1.3 MANIFOLD GENERATION

In Chem1D the detailed chemistry solutions are computed in physical space and time. These flame solutions are tabulated as a function of the chosen controlling variables. Two controlling variables were adopted: a progress variable \mathcal{J} , to follow the progress of the reaction and a mixture fraction Z to represent the mixing between fuel and oxidizer. Therefore, a coordinate transformation from space and time to Z and \mathcal{J} is performed.

The mixture fraction is a conserved scalar. In particular, the following definition from [120] is adopted:

$$Z = \frac{2 \frac{Z_C - Z_{C,2}}{M_C} + \frac{1}{2} \frac{Z_H - Z_{H,2}}{M_H} - \frac{Z_O - Z_{O,2}}{M_O}}{2 \frac{Z_{C,1} - Z_{C,2}}{M_C} + \frac{1}{2} \frac{Z_{H,1} - Z_{H,2}}{M_H} - \frac{Z_{O,1} - Z_{O,2}}{M_O}}, \quad (3.8)$$

where Z_i is the element mass fraction and M_i is the molar mass of the elements carbon (C), hydrogen (H) and oxygen (O). The subscripts 1 and 2 refer to the constant mass fraction in the defined fuel and oxidizer stream, respectively.

The progress variable is usually defined as a (linear) combination of reaction product species. Such a definition should satisfy the requirement for monotonicity and should represent the various stages during the reaction progress in a balanced way. Usually, under traditional combustion conditions, the standard FGM model adopts CO_2 and H_2O to define the progress variable. However, in this work HO_2 was also included in \mathcal{J} definition. In fact, according to Medwell et al. [121], in a MILD combustion system first the preignition chemistry takes place and the precursor species like HO_2 and CH_2O are produced, while the final products are not formed in considerable quantities. Therefore, a combination of CO_2 , H_2O and HO_2 was selected as a progress variable to include the effects of both preignition and oxidation chemistries. The general form for the linear combination of the combustion product Y_c reads

$$Y_c = \sum_{i=1}^{N_{sp}} \alpha_i Y_i, \quad (3.9)$$

where α_i refers to the weight factors of the specie i , which are optimized to yield a smooth mapping of the variables with respect to the controlling ones. The coefficients are chosen as $\alpha_{H_2O}=100/M_{H_2O}$, $\alpha_{CO_2}=100/M_{CO_2}$ and $\alpha_{HO_2}=1000/M_{HO_2}$, whereas $\alpha_i=0$ for all other species. Then, the progress variable \mathcal{J} is obtained by scaling Y_c between 0 and 1 using its maximum and minimum values, Y_c^{max} and Y_c^{min} , respectively, as follows

$$\mathcal{J} = \frac{Y_c - Y_c^{min}}{Y_c^{max} - Y_c^{min}}. \quad (3.10)$$

Accordingly, a scaled production rate of the progress variable, $\dot{\omega}_J$, is defined as

$$\dot{\omega}_J = \frac{\sum_{i=1}^{N_{sp}} \alpha_i \dot{\omega}_i}{Y_c^{max} - Y_c^{min}}, \quad (3.11)$$

Thus, each thermochemical parameter ϕ calculated from Equations 3.1-3.4 or 3.5-3.7 (depending on the Flamelet configuration chosen), is tabulated as a function of Z and \mathcal{J}

$$\phi = \phi(Z, \mathcal{J}). \quad (3.12)$$

The controlling variables definitions, the coordinate transformation and the storage in the look-up tables were carried out by means of Matlab R2019a scripts [122]. In the resulting 2D table, 50 grid points were chosen for both mixture fraction and progress variable. In Figure 3.3, as an example, the manifolds in the Z, \mathcal{J} space of $\dot{\omega}_J$ and T , calculated for the stoichiometric air/methane case and the IML configuration, are reported. It can be observed that the maximum production rates and temperatures are gathered at the stoichiometric mixture fraction Z_{st} .

In order to include the effect of the turbulence, the dimension of the defined laminar look-up tables needs to be enhanced by including the variances of the controlling variables. Before that, the progress variable must be made statistically independent of Z . In particular, \mathcal{J} can be transformed in C as follows

$$C = \frac{J - J^u}{J^b - J^u}, \quad (3.13)$$

where J^u and J^b are the progress variable in unburned state and burned state, respectively.

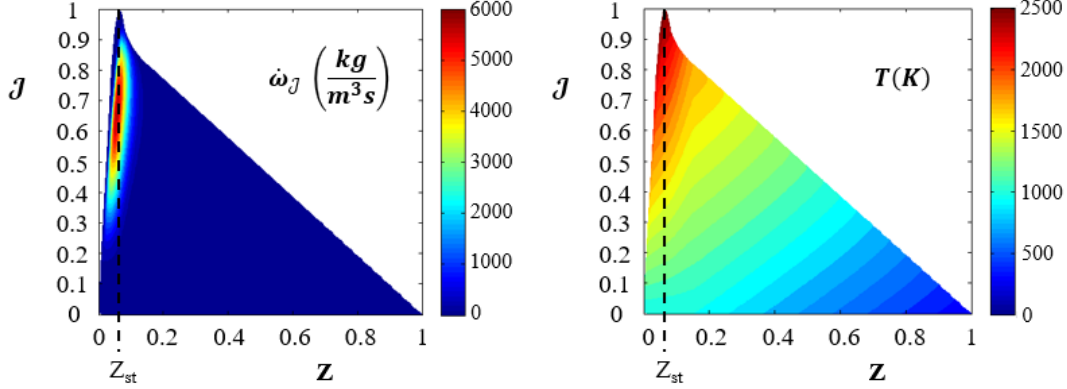


FIGURE 3.3 - MANIFOLDS IN THE Z, J SPACE FOR THE PROGRESS VARIABLE PRODUCTION RATE (LEFT) AND THE TEMPERATURE (RIGHT) CALCULATED FOR THE STOICHIOMETRIC AIR/METHANE CASE WITH THE C1C3 KINETIC MECHANISM [8] AND THE IML CONFIGURATION.

Therefore, the laminar flame solutions are integrated with presumed β -PDF functions [123] \tilde{P} of the mixture fraction Z and the scaled progress variable C , to account for turbulent fluctuations. The mean quantities are defined as:

$$\tilde{\phi} = \int_0^1 \int_0^1 \phi(Z, C) \tilde{P}(Z, \tilde{Z}, \tilde{Z}''^2) \tilde{P}(C, \tilde{C}, \tilde{C}''^2) dZ dC, \quad (3.14)$$

where $\tilde{\phi}$ is the fluctuation of the generic thermochemical variable, \tilde{Z} and \tilde{C} are the mean values and \tilde{Z}''^2 and \tilde{C}''^2 are the variances of mixture fraction and scaled progress variable, respectively. Such explicit formulation is valid because Z and C are statistically independent. Thus, the final FGM look-up table has four dimensions and each fluctuation of the generic thermochemical variable is tabulated as

$$\tilde{\phi} = \tilde{\phi}(\tilde{Z}, \tilde{Z}''^2, \tilde{C}, \tilde{C}''^2). \quad (3.15)$$

The global grid consists of 50 points for the mean values and 11 points for the variances ($50 \times 50 \times 11 \times 11$ grid points).

3.2 CFD setup

The Reynolds-Averaged Navier-Stokes (RANS) equations for continuity, momentum, total enthalpy and controlling variables (defined in the previous Section) are implemented on the CFD solver, where the coupling between with the FGM model is obtained. Before explaining how this is achieved, in this Section the details regarding the computational grid (see [Paragraph 3.2.1](#)), the turbulence (see [Paragraph 3.2.3](#)) and the radiative heat transfer model used (see [Paragraph 3.2.3](#)) are presented.

3.2.1 GRID INDEPENDENCE STUDY

A complete 3D geometry of the combustion chamber is considered for the RANS simulations of the cyclonic chamber. An optimized hexahedral structured computational grid, composed of about 400k elements, has been developed with ANSYS Icem 18.1 [124]. The computational domain, depicted in Figure 3.4, covers the complete inner volume of the cyclonic chamber. Its size is $20 \times 20 \times 5 \text{ cm}^3$ plus the nozzles, which are long enough to guarantee a fully developed speed profile at the inlet. The O-grid method was used to handle the round orifices at inlets and outlet of the burner. A consistent refinement in the inlet region was carried out in order to enhance the simulation of the mixing under turbulent conditions between fresh reactants and recirculating exhausts.

To evaluate the reliability of the computational grid, a study of independence is performed. In particular, the dependence of the CFD runs on the grid size is assessed by considering two additional meshes: a sparser cell with 300k hexahedral elements and a denser one with 600k cells. In Figure 3.5 the comparison between the predicted temperature profiles at the midplane for the three grids is shown for the case reported in Table 2.3.

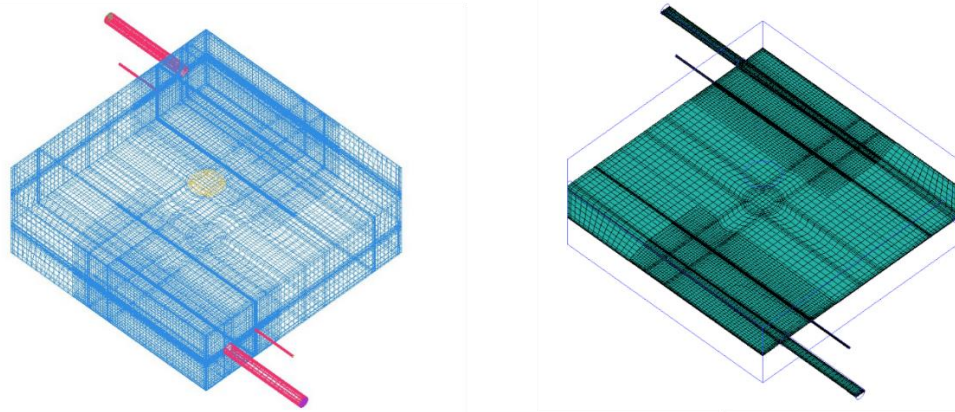


FIGURE 3.4 – STRUCTURED COMPUTATIONAL GRID OF THE LUCY BURNER DEPICTED FOR THE EXTERNAL DOMAIN (LEFT) AND THE INTERNAL MIDPLANE SECTION (RIGHT).

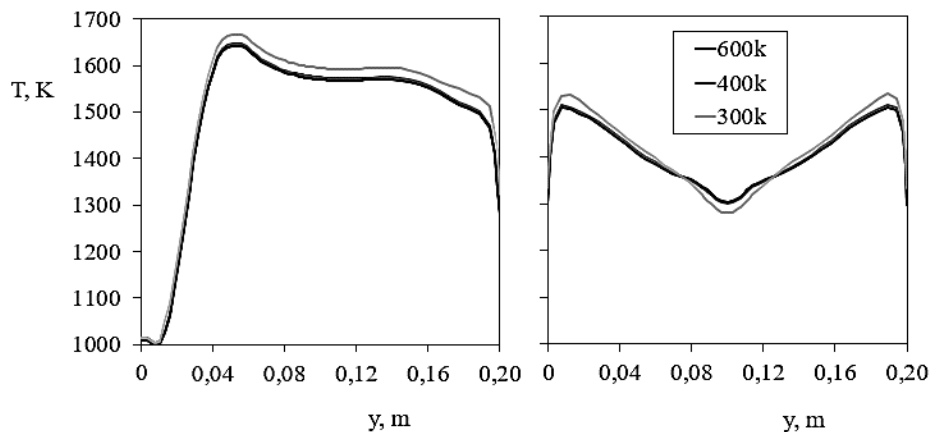


FIGURE 3.5 – STUDY OF INDEPENDENCE ON THE NUMBER OF GRID CELLS.

Such a study reveals that a number of hexahedral cells higher than 400k do not affect the numerical results. On the other hand, 300k elements lead to a temperature field less homogeneous compared to the other grids, likely due to a not accurate computational calculation. The choice of the mesh with 400k cells for the cyclonic chamber, therefore, is justified.

3.2.2 TURBULENCE MODEL

The pressure-velocity coupling is ensured using the SIMPLE scheme whereas the second-order upwind discretization is used for all the transported variables. The RANS equations are solved using the $k - \varepsilon$ turbulence model with re-normalization group

(RNG) [125] theory. The RNG introduces a new term in the equation of the turbulence kinetic energy dissipation rate ε , which depends on the rate of strain of the turbulence, thus improving the accuracy for rapidly strained flows. The standard $k - \varepsilon$ model is a high-Reynolds number model whereas the RNG $k - \varepsilon$ provides an analytically derived differential formula for effective viscosity that accounts for low-Reynolds number effects. Moreover, the swirl-dominated-flow option is included in order to account for the effects of swirl or rotation by modifying the turbulent viscosity appropriately. The effective use of this feature, however, depends on the appropriate treatment of the near-wall region. The Enhanced wall treatment (EWT) [125], therefore, is adopted as a near-wall modelling method. It combines a two-layer model with the so-called enhanced wall functions, increasing the accuracy of the simulations near the walls and reducing the mesh-dependency effects. In order to support the choice of the $k - \varepsilon$ model, in Figure 3.6 the comparison between the flow-field measurements obtained by means of Particle Image Velocimetry (PIV) and the numerical simulation carried out with three different turbulence models is reported. The PIV results are obtained under non-reactive conditions with a cold-flow cyclonic configuration able to mimic the same fluid-dynamic patterns of reactive conditions (same inlet Reynolds number and inlet average velocity).

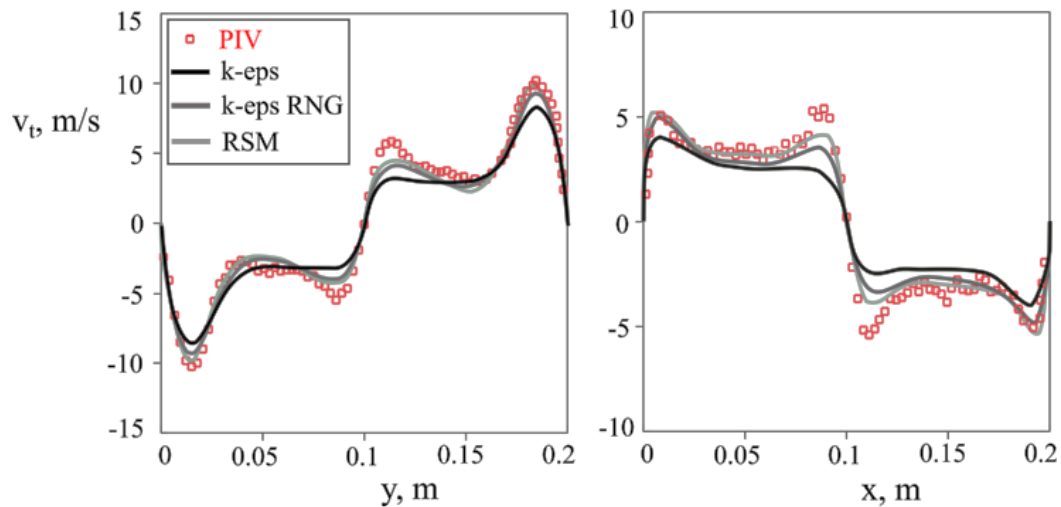


FIGURE 3.6 – COMPARISON BETWEEN THE MEASURED AND SIMULATED TANGENTIAL VELOCITY PROFILES IN THE MID-PLANE ALONG THE DIRECTION AT $x=0.1$ M (LEFT) AND AT $y=0.1$ M (RIGHT).

The turbulence models used, in particular, are the standard $k - \varepsilon$, the RNG $k - \varepsilon$ with swirl correction and the Reynolds Stress Model (RSM). The tangential velocity v_t is reported for two reference lines, at $x=0.1$ m and $y=0.1$ m (see Figure 2.1), on the mid-plane of the burner. It is worth noting that the models RSM and k-eps RNG with swirl correction provide the best agreement with PIV data depicting very similar results. On the other hand, the standard $k - \varepsilon$ model shows a worse agreement than the others. Therefore, the k-eps RNG model with swirl correction is chosen for this thesis work because of its lower computational cost with respect to RSM.

The inlet turbulence intensity level affects simulation results, similarly to other configurations, such as JHC [126]. In particular, such parameter plays a relevant role in the temperature field predictions, especially along the lateral thermocouple position. In Figure 3.7 a sensitivity analysis on the inlet turbulence levels (TI) is reported in order to support the choice of the value used for the cyclonic flow-field. Four different values of the inlet turbulence intensity are investigated: 4%, 5%, 7% and 10%. The results are reported by comparing the numerical temperature fields for each TI value with the measured ones for a diluted condition ($d=90$) of the mixture CH_4/Air .

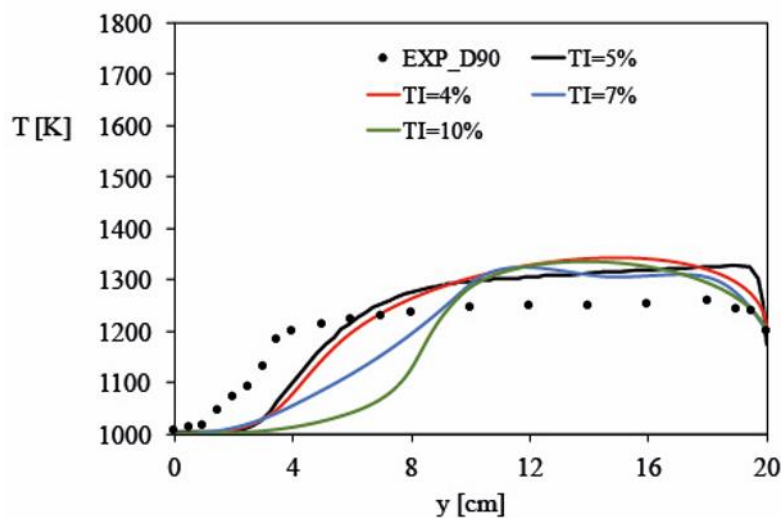


FIGURE 3.7 – EFFECT OF THE INLET TURBULENCE LEVELS (TI) ON THE TEMPERATURE PREDICTIONS.

The profiles are reported for the lateral thermocouple position (T_1). The best agreement with the temperature measurements is obtained for $TI=5\%$ and therefore this value is chosen for the velocity inlet boundary in the CFD calculation.

3.2.3 RADIATION MODEL

The modelling of the radiative source term in the energy balance involves both the evaluation of the gas radiative properties, ε_g and the resolution of the radiative transfer equation (RTE) [109].

In this work, in order to model the radiative properties of the mixture H_2O/CO_2 , a modified Weighted-sum-of-grey-gases (WSGG) model with four gray gases and one clear gas is implemented. The basic assumption of the WSGGM [127] is that the total emissivity ε_g of a given non-gray gas over a distance s can be presented as the sum of the emissivities of a fixed number N of gray gases, as follows

$$\varepsilon_g = \sum_{j=0}^N a_j [1 - \exp(-k_j p s)], \quad (3.16)$$

where a_j and k_j are the emissivity weighting factor and the absorption coefficient for the j^{th} fictitious gray gas, respectively. In particular, the bracketed quantity is the emissivity of the j^{th} fictitious gray gas, where p is the sum of the partial pressures of all the absorbing gases and s is the path length. The absorption coefficient for clear gas ($j = 0$) is zero. The modification of the WSGG is based on the use of the coefficients proposed by R. Johansson et al. [106] in order to account for variations of temperatures and concentrations of H_2O and CO_2 in each computational cell. Both the absorption coefficients and the weights depend on mole ratio, while only the weights depend on temperature.

$$a_j = \sum_{i=1}^3 c_{j,i} \left(\frac{T}{T_{ref}} \right)^{i-1}, \quad \text{with } T_{ref} = 1200 \text{ K}, \quad (3.17)$$

$$k_j = K1_j + K2_j \frac{Y_{H2O}}{Y_{CO2}}, \quad (3.18)$$

$$c_{j,i} = C1_{j,i} + C2_{j,i} \frac{Y_{H2O}}{Y_{CO2}} + C3_{j,i} \left(\frac{Y_{H2O}}{Y_{CO2}} \right)^2, \quad (3.19)$$

where Y_{H_2O} and Y_{CO_2} are mole fraction in the medium. The values for coefficients $K1_j$, $K2_j$, $C1_{j,i}$, $C2_{j,i}$, and $C3_{j,i}$ can be found in reference [106]. The weighting factors for the clear gas are given by

$$a_0 = 1 - \sum_{j=1}^4 a_j \quad (3.20)$$

And makes the sum of the weights equal to unity. The total absorption coefficient is then estimated by

$$k = -\frac{\ln(1 - \varepsilon_g)}{s}, \quad (3.21)$$

where the mean beam length, according to the domain-based recommended by Hottel and Sarofim [127], reads

$$s = \frac{3.6V}{A}, \quad (3.22)$$

where V is the volume of the domain and A the corresponding surface area. The use of such modified WSGG to evaluate the absorption coefficient of the exhausts derives from an optimization between accuracy and computational cost. In fact, the Spectral-Line Weighted-sum-of-gray-gases (SLW) model [107], which allows a more advanced modelling of the radiative heat transfer, was proved to give significant improvements with respect to WSGG only in the flame front region, where high gradients of temperature are located. Therefore, the flameless nature of the MILD process and the low gradients within the combustion chamber support the use of a modified WSGG to obtain reliable results for such systems.

On the other hand, the RTE is solved by using the Discrete Ordinate Method (DOM) [99]. The RTE is a mathematical statement which expresses the conservation of a beam of radiation (ray) travelling along a path through a medium. Radiation travelling along a path is reduced by absorption and scattering (out-scattering) and is enhanced by emission and by radiation in-scattered from other directions. The RTE for non-scattering media reads

$$\frac{dI_\lambda}{ds} = k_\lambda(I_{b\lambda} - I_\lambda), \quad (3.23)$$

where I_λ is the spectral radiation intensity, $I_{b\lambda}$ is the spectral radiation intensity for a black body and k_λ is the spectral absorption coefficient of the medium. The DOM solves the RTE for a set of discrete rays spanning a full sphere around their origin. Thus, the whole solid angle surrounding each point is split into a certain number of smaller solid angles, each of them with its related direction. The resolution of the RTE along each direction yields differential equations in terms of the new directions [110].

Therefore, for non-scattering media and evaluating the spectral radiative properties of the exhaust mixture from equation 3.15, the equation 3.16 may be rewritten in terms of the cartesian coordinate system (x, y, z) , for any discrete direction s_i , as follows

$$\xi_i \frac{\partial I}{\partial x} + \eta_i \frac{\partial I}{\partial y} + \zeta_i \frac{\partial I}{\partial z} = k(I_b - I), \quad (3.24)$$

where ξ_i , η_i and ζ_i are the directional cosines, which are the scalar products of s_i and the unit vector of the respective axis in the coordinate system. Thus, the radiation intensity I , solution of the RTE (equation 3.23), modifies the radiative source term $\nabla \cdot q$ in the enthalpy equation, which represents the conservation of the overall radiative energy of the system and can be expressed as

$$\nabla \cdot q = \int_0^{+\infty} k(4\pi I_b - \int_{4\pi} I d\Omega), \quad (3.25)$$

where q is the radiative heat flux and Ω the solid angle. Finally, the walls of the burner are treated as gray (opaque) with an emissivity of 0.6 (emissivity of the alumina layer). The diffuse fraction is set to 1, indicating that all the radiation is diffused, and none is reflected.

3.3 CFD code and FGM interaction

During the run-time, the RANS equations based on $k - \varepsilon$ are for controlling variables, mass, momentum and energy, in addition to the RTE (see Equation 3.24), are solved on the commercial software ANSYS Fluent [125]. In particular, the transport equations for the Favre-averaged means and variances of the mixture fraction Z and the un-scaled progress variable \mathcal{J} , read

$$\frac{\partial}{\partial x_i} (\bar{\rho} \tilde{u}_i \tilde{Z}) = \frac{\partial}{\partial x_i} \left[\left(\bar{\rho} D + \frac{\mu_t}{Sc_t} \right) \frac{\partial \tilde{Z}}{\partial x_i} \right], \quad (3.26)$$

$$\frac{\partial}{\partial x_i} (\bar{\rho} \tilde{u}_i \tilde{J}) = \frac{\partial}{\partial x_i} \left[\left(\bar{\rho} D + \frac{\mu_t}{Sc_t} \right) \frac{\partial \tilde{J}}{\partial x_i} \right] + \overline{\dot{\omega}_J}, \quad (3.27)$$

$$\begin{aligned} \frac{\partial}{\partial x_i} (\bar{\rho} \tilde{u}_i \tilde{Z}''^2) &= \frac{\partial}{\partial x_i} \left[\left(\bar{\rho} D + \frac{\mu_t}{Sc_t} \right) \frac{\partial \tilde{Z}''^2}{\partial x_i} \right] + B \frac{\mu_t}{Sc_t} \left(\frac{\partial \tilde{Z}}{\partial x_i} \right)^2 \\ &- A \bar{\rho} \frac{\varepsilon}{k} \tilde{Z}''^2, \end{aligned} \quad (3.28)$$

$$\begin{aligned} \frac{\partial}{\partial x_i} (\bar{\rho} \tilde{u}_i \tilde{J}''^2) &= \frac{\partial}{\partial x_i} \left[\left(\bar{\rho} D + \frac{\mu_t}{Sc_t} \right) \frac{\partial \tilde{J}''^2}{\partial x_i} \right] + 2 \frac{\mu_t}{Sc_t} \left(\frac{\partial \tilde{J}}{\partial x_i} \right)^2 - A \bar{\rho} \frac{\varepsilon}{k} \tilde{J}''^2 \\ &+ 2 \overline{\tilde{J}'' \dot{\omega}_J}. \end{aligned} \quad (3.29)$$

In Equations 3.26-3.29, $\bar{\rho}$ is the Reynolds-averaged density, \tilde{u}_i the Favre-averaged mean velocity vector, D the molecular diffusion coefficient, μ_t the turbulent viscosity, Sc_t the turbulent Schmidt number, $\overline{\dot{\omega}_J}$ the Reynolds-averaged mean chemical source term of the progress variable (see Equation 3.11), A and B the modelling constants, k and ε are the turbulent kinetic energy and the corresponding dissipation rate from the turbulent model. In the equations given above, the gradient transport assumption [128] coupled with unity Lewis numbers for all variables, is used to model the turbulent diffusion terms.

In Figure 3.8 a schematic representation of the numerical method is summarized. In particular, the model can be viewed as consisting of two separate parts. One being a chemistry pre-processing part and the other an online calculation procedure where the pre-processed chemistry is used in the form of a lookup database. This explicit separation of the chemistry computation from the 3D flow field computation is the reason for the gain in computational efficiency. Each run-step, the averages and variances of the mixture fraction and the progress variable ($\tilde{Z}, \tilde{Z}''^2, \tilde{J}, \tilde{J}''^2$) are computed and used to interpolate in the FGM database in order to retrieve the desired quantities. Then the progress variable is scaled ($\tilde{J}, \tilde{J}''^2 \rightarrow \tilde{C}, \tilde{C}''^2$) and the chemical

sources for the mean and the variance of the progress variable and for the variance of the mixture fraction are calculated and returned to the transport equations in question.

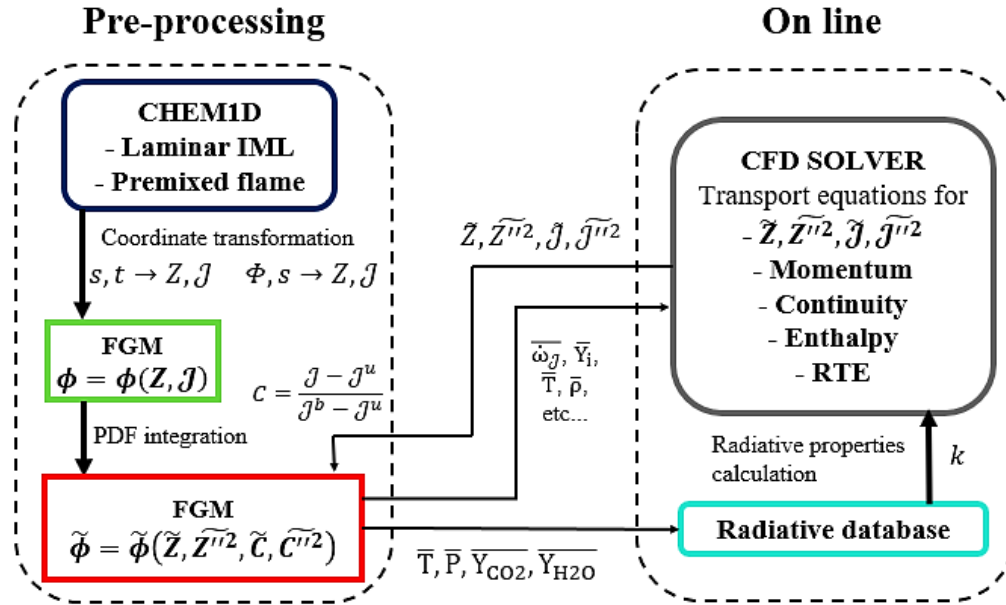


FIGURE 3.8 - SCHEMATIC REPRESENTATION OF THE NUMERICAL MODEL SEPARATED IN A PRE-PROCESSING AND AN ONLINE CALCULATION PART

Also, the species mass fractions are returned to the solver to compute the temperature via the enthalpy conservation equation. Indeed, since the look-up table is created from the computation of adiabatic Flamelet, the heat loss is not included in the manifold and, therefore, it must be considered only in the CFD calculation. To this end, Fluent simply freezes the species from the adiabatic table and recalculates the temperatures and the source terms for the new enthalpy. The total enthalpy equation reads

$$\frac{\partial}{\partial x_i} (\bar{\rho} \tilde{u}_i \tilde{h}) = \frac{\partial}{\partial x_i} \left[\left(\bar{k} + \frac{\mu_t \bar{c}_p}{Pr_t} \right) \frac{\partial \tilde{h}}{\partial x_i} \right] + \bar{\nabla} \cdot \bar{q}, \quad (3.30)$$

where \bar{k} is the mean thermal conductivity, \bar{c}_p the mean heat capacity, Pr_t the turbulent Prandtl number and $\bar{\nabla} \cdot \bar{q}$ the mean radiative source term (equation 3.25). Therefore, the enthalpy equation is modified by radiation by means of the radiative source term which is a function of the radiation intensity I evaluated by the RTE (equation 3.24). In order to calculate I in each run-step, the absorption coefficient of the medium k is

retrieved from the radiative database [106] by using the mass fractions of the combustion products, the temperature and the total pressure, which are looked-up from the FGM table $(\bar{T}, \bar{P}, \bar{Y}_{\text{CO}_2}, \bar{Y}_{\text{H}_2\text{O}})$.

Chapter 4

Results of the CFD Modelling

The main results of the numerical simulation of the LUCY burner by using the methodology presented in the former Chapter (see [Chapter 3](#)), are reported here and discussed in detail. In the first section, some general results of the model are presented and remarked (see [Section 4.1](#)). Then, to understand how the predictions of FGM are affected by the chemistry, the role of the detailed mechanism and the Flamelet configuration is investigated (see [Section 4.2](#)). Afterwards, the influence of the inlet conditions on the model prediction is assessed. In particular, the numerical results are compared with experiments, for different external operative parameters (see [Section 4.3](#)). Then, the effect of the radiative heat transfer on the model performance is highlighted and discussed (see [Section 4.4](#)). In conclusion, in [Section 4.5](#), the FGM performances are compared to those obtained with the tabulation of a non-adiabatic Perfectly Stirred Reactor (PSR).

4.1 CFD simulation of the MILD cyclonic burner

In this section, the main characteristics of the CFD simulations of the cyclonic chamber with the FGM model are shown for case A, reported in Table 4.1. In the table, in particular, the operative parameters (see [Section 2.2](#)) are listed.

TABLE 4.1 - BOUNDARY CONDITIONS OF CASE A.

CASE	Fuel	Diluent	d	T _{in} , K	Φ	P, kW	Q _w , kW/m ²	T _{out} , K
A	CH ₄	N ₂	71.4	1000	1	2	12	1250

The pathlines of the simulated flow field are depicted in Figure 4.1. From the figure, it is worth noting that the CFD results confirm the presence of a strong recirculation which ensures high residence times within the chamber. In fact, the pathlines show that the by-pass flow leaving the system at the outlet section as soon as it gets inside

the cyclonic chamber is nearly absent. The high-speed oxidizer jet leads to a robust swirl within the reactor and the fuel jet is strongly bent by EGR, guaranteeing an efficient mixing between the streams. Moreover, a large toroidal recirculation zone is established inside the combustor, and the high gas recirculation rates promote the attainment of the high-temperature and low-oxygen-concentration conditions required for the stabilization of the MILD regime.

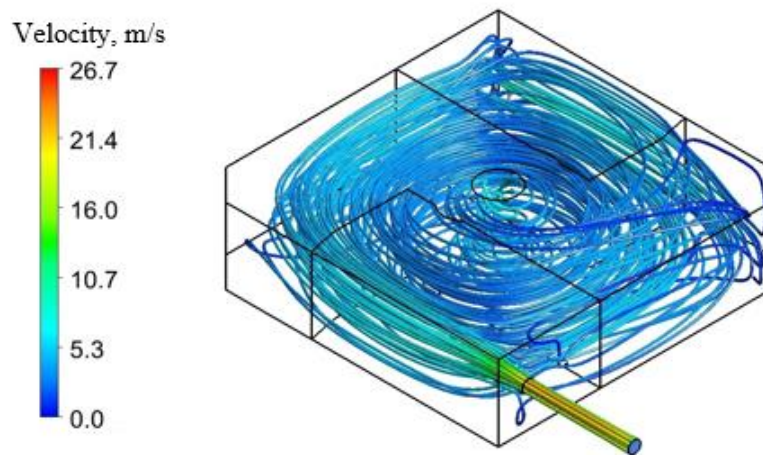


FIGURE 4.1 – SIMULATED PATHLINES OF THE CYCLONIC FLOW FIELD FOR CASE A.

In Figure 4.2 the main boundary conditions and the contours of velocity and temperature on two inner surfaces are reported for methane-fired conditions. At the two couples of inlets, the velocities (velocity inlet boundary condition) of oxidant and fuel are fixed at v_{ox} and v_f , respectively, whereas the preheating temperature of the oxidizer is set to T_{in} whereas the temperature of the fuel to 300 K. At the outlet section (pressure outlet boundary condition) the temperature measured by a fixed N-thermocouple, T_{out} (see [Section 2.3](#)), is used. Furthermore, the heat loss flux at walls Q_w , evaluated by means a global enthalpy balance (see [Section 2.3](#)), is set as a boundary condition. The velocity field (left side of the figure) confirms the considerations on the cyclonic flow field made in the pathlines analysis. The simulated thermal field (right side of the figure) highlights the very homogeneous temperature

distribution inside the chamber, as one would expect for MILD combustion, except for the inlet zone.

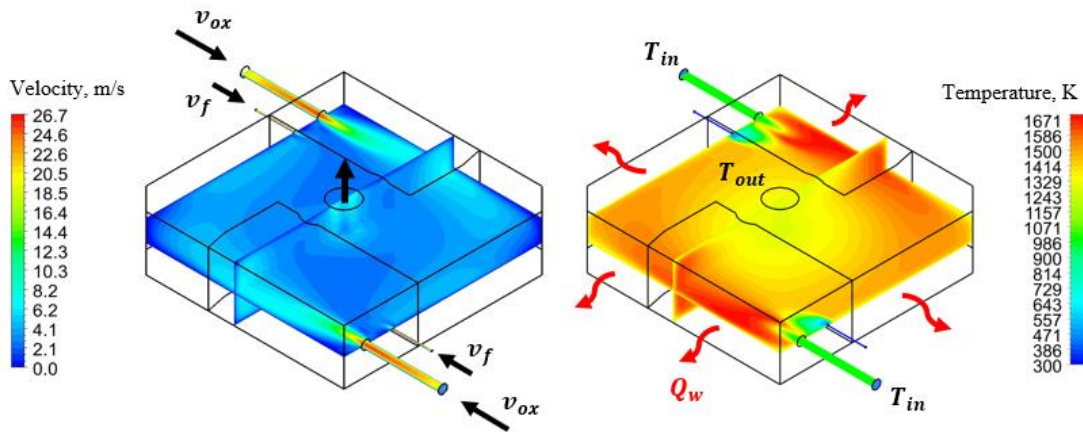


FIGURE 4.2 - SIMULATED VELOCITY (LEFT) AND TEMPERATURE (RIGHT) FIELDS OF THE CYCLONIC CHAMBER FOR CASE A.

In Figure 4.3, the contours of mean and variance of the mixture fraction, mean and source term of the progress variable and for the mass fractions of H_2O , CO_2 , HO_2 and OH , are depicted. The distribution of the mixture fraction shows that the fuel stream is promptly mixed with the oxidizer and the recirculating flow as soon as it gets into the chamber. Therefore, except for the inlet region, the value of the mixture fraction is uniform and equal to Z_{st} (because of the stoichiometric inlet condition of the case considered). Consequently, the variance $\widetilde{Z''^2}$ is concentrated in the inlet area and is almost zero in the rest of the chamber volume. The field of the mean progress variable \widetilde{J} , on the other hand, evolves from the zero value at the inlets to the maximum value in the centre of the burner. Indeed, in this region, the combustion products at equilibrium recirculate, as shown by the contours of $\overline{Y_{CO_2}}$ and $\overline{Y_{H_2O}}$. In the figure, it can be also noted that the maximum production rate of the progress variable is located in the mixing zone between the fuel and oxidizer streams, whereas it approaches zero in the rest of the reactor. Such location for the reactivity of the system is also confirmed by the peaks in the mass fractions of the combustion products and of OH and HO_2 . The mass fraction of HO_2 , Y_{HO_2} , identifies the ignition region near to the fuel inlet,

supporting the choice of using such a variable in the definition of the progress variable (see Equation 3.9).

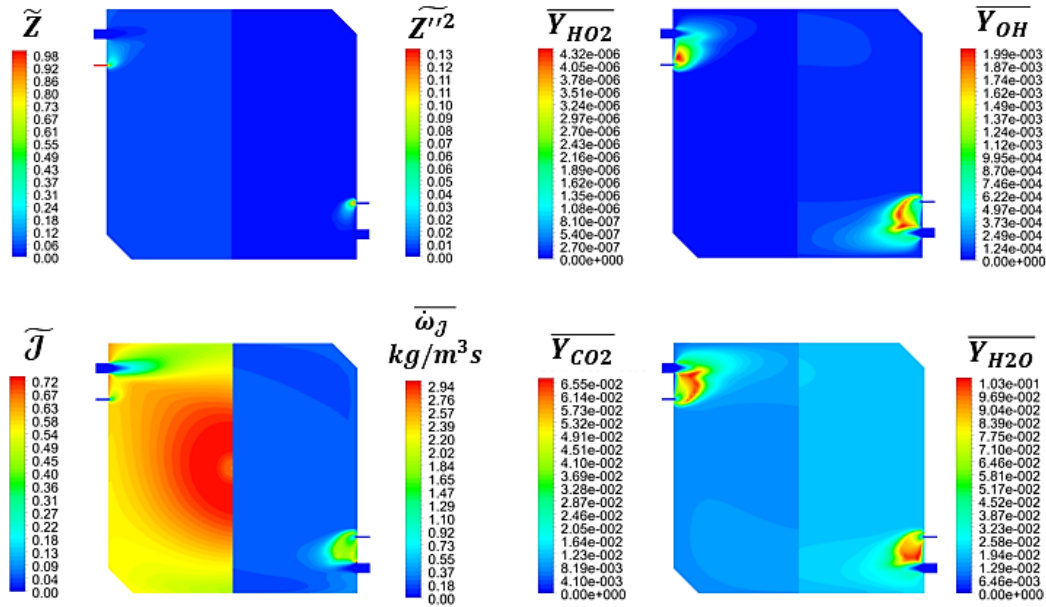


FIGURE 4.3 - SIMULATED FIELDS FOR SEVERAL QUANTITIES ON THE MIDPLANE OF THE CYCLONIC CHAMBER FOR CASE A

In order to assess the reliability of such numerical results and the dependency of the prediction on the cyclonic burner boundaries, in the following sections, the simulations will be compared to the experimental data obtained for a wide range of operative conditions.

4.2 Sensitivity on the chemistry resolution

In this section, the sensitivity of the model on the kinetic mechanism (see [Paragraph 4.2.1](#)) and the 1D flame configuration (see [Paragraph 4.2.2](#)) chosen for the computation of the Flamelet equations (see Equations. 3.1-3.7), is discussed.

TABLE 4.2 BOUNDARY CONDITIONS OF CASES A, B AND C.

CASE	Fuel	Diluent	d	T _{in} , K	Φ	P, kW	Q _w , kW/m ²	T _{out} , K
B	C ₃ H ₈	N ₂	94	1045	1	1	5.1	1220

A	CH ₄	N ₂	AIR	1000	1	2	13	1250
C	CH ₄	N ₂	90	1000	1	2	11	1210

To this end, the simulated thermal field is compared to the temperature measurements of the two movable thermocouples, T_1 and T_c (see [Section 2.3](#)). The operative conditions investigated are reported in Table 4.2.

4.2.1 EFFECT OF THE KINETIC MECHANISM

To assess the role of chemistry in MILD conditions using the FGM model, different kinetic mechanisms are tested for case B. In particular, a propane-fuel case is chosen to carry out this analysis because of its more complicated kinetics compared to methane, which is the other fuel object of this thesis study. In Figure 4.4, the comparison between measured (with the relative uncertainties evaluated as reported in [Section 2.3](#)) and simulated temperature profiles at the midplane is shown for three different chemical kinetic mechanisms: C1C3 from Polimi [8], San Diego [129] and the Lindstedt mechanism [130].

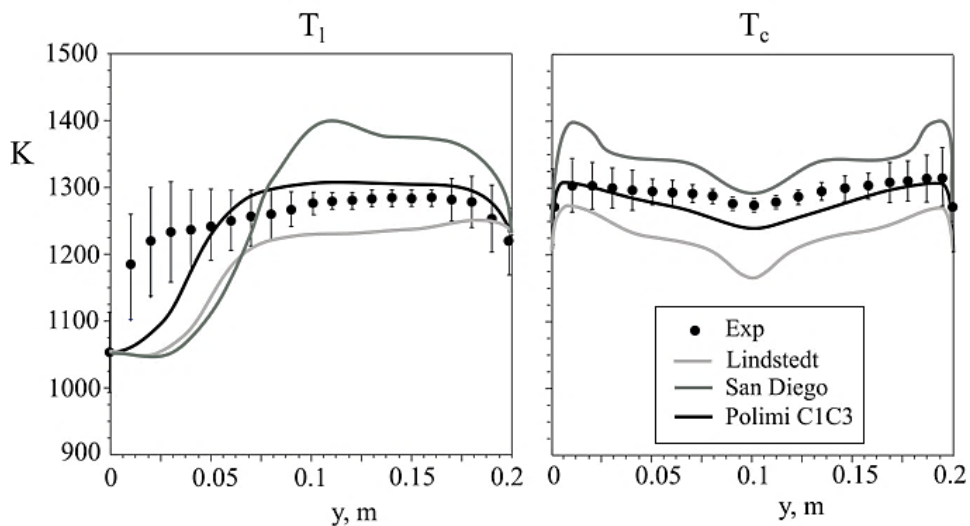


FIGURE 4.4 - MEASUREMENTS WITH UNCERTAINTIES (SYMBOLS WITH ERROR BARS) AND PREDICTED TEMPERATURE BY FGM (SOLID LINES) USING THREE DIFFERENT KINETIC MECHANISMS FOR CASE B.

The IML configuration is used. As expected, the more detailed C1C3 reaction mechanism from Polimi reproduces the measured temperature field with high accuracy respect to the other two. In particular, San Diego overestimates the mean temperature and presents a high inhomogeneity in the thermal field, whereas the Lindstedt mechanism underpredicts the thermal field but preserves the uniformity of the temperature. Moreover, both the San Diego and Lindstedt mechanisms predict a delayed temperature increase in the region close to the oxidizer nozzle.

Based on these results, the C1C3 mechanism from Polimi was chosen for the numerical simulations reported in the following sections (both for propane and methane) because of its more reliable predictions for the considered hydrocarbon fuels.

4.2.2 EFFECT OF FLAMELET CONFIGURATION

In order to investigate the influence of the Flamelet configuration chosen to solve the chemistry, here a comparison between the numerical results obtained with IML and premixed flame (see [Paragraph 3.1.2](#)) is reported for cases A and C of Table 4.2. First, in Figure 4.5, the manifolds of source term of the progress variable and temperature are depicted for case A using both the 1D flames.

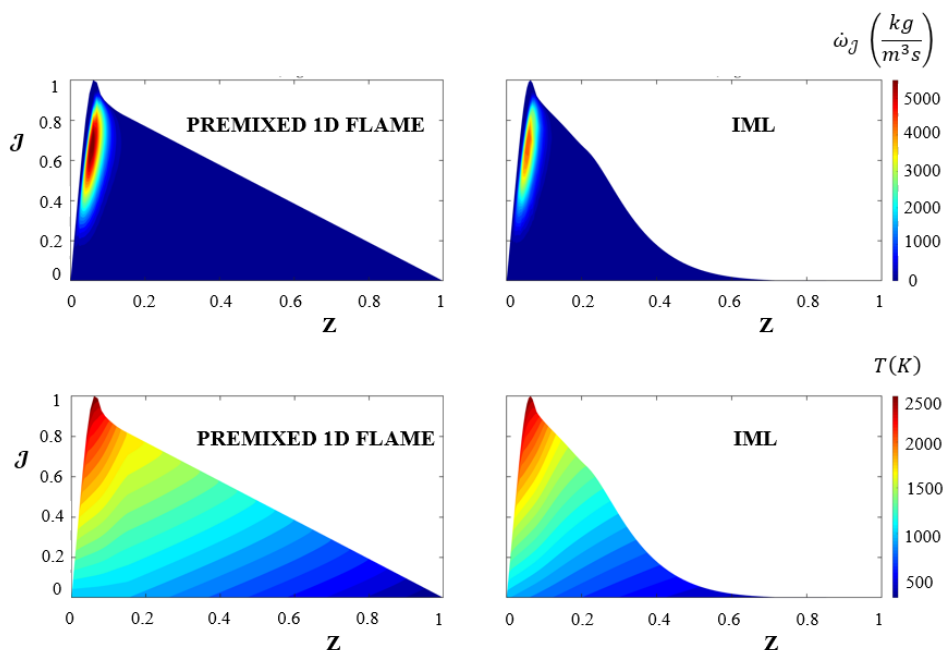


FIGURE 4.5 - MANIFOLDS IN THE Z, J SPACE FOR $\dot{\omega}_j$ AND TEMPERATURE CALCULATED FOR CASE A WITH PREMIXED 1D FLAME (LEFT) AND IML (RIGHT).

It is worth noting that in order to extend the manifold to the mixture fractions located outside the flammability limits, for the premixed case, a linear interpolation was made, as it is clear in the figure, especially for the rich area. The premixed flame shows higher values of the $\dot{\omega}_j$ compared to IML, due to the absence of diffusive transport. On the other hand, the same temperature range is observed, because of the adiabaticity of both Flamelet equations. However, for the premixed flame, an overestimation of the temperature is predicted for mixture fractions near to 1, due to the interpolation.

In Figure 4.6, the predicted temperature profiles along the central and lateral positions, T_c and T_l , using both IML and the 1D premixed flame, are compared to the measured data for cases A and C. The experimental data (symbols) emphasize the high isothermality of the system with very small temperature gradients.

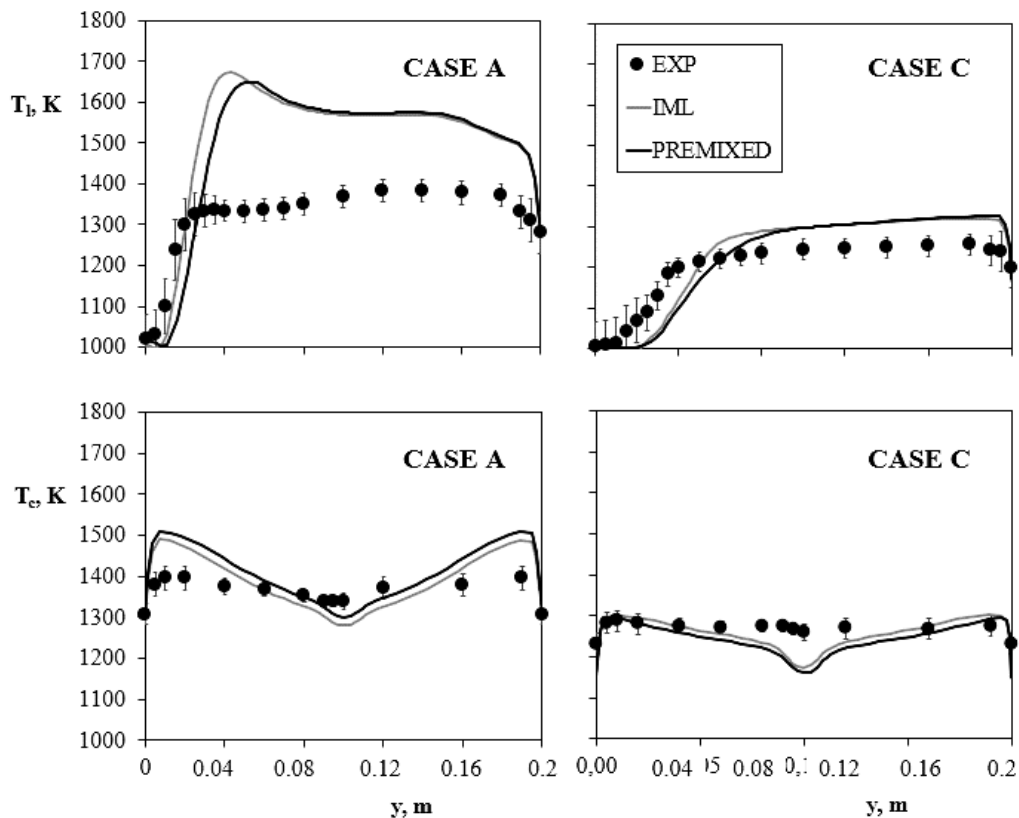


FIGURE 4.6 - MEASUREMENTS WITH UNCERTAINTIES (SYMBOLS WITH ERROR BARS) AND PREDICTED TEMPERATURE BY FGM (SOLID LINES) USING TWO DIFFERENT FLAMELET CONFIGURATION FOR CASE A AND C.

The numerical results are in better agreement for case C compared to case A (the reasons will be discussed in detail in the following sections). For both the cases, the T_c profile shows no noticeable difference between the simulated temperature adopting the IML or the premixed 1D flame in FGM computation. Regarding the T_1 profile, the effect of the Flamelet configuration is noticeable only in the inlet zone ($y < 0.04$ m). In fact, the use of the IML flame structure leads to an early ignition and a higher peak compared to the premixed one. This can be explained by the effect of the diffusion in IML, which moves the temperature towards the hot oxidizer side. However, such an effect is less marked for the most diluted case C. Following these findings, the numerical results reported in the following sections will be related to the IML configuration, in order to account for the diffusion effects in the mixing zone and to avoid the errors given by interpolation.

4.3 Sensitivity on the external operating parameters

In this section, it is studied how the inlet boundaries (operative parameters) affect the predictivity of FGM for the cyclonic burner. In the following paragraphs is reported the effect of inlet mixture composition (see [Paragraph 4.3.1](#)), inlet preheating temperature (see [Paragraph 4.3.2](#)), inlet dilution level (see [Paragraph 4.3.3](#)) and diluent nature (see [Paragraph 4.3.4](#)). The cases considered are listed in Table 4.3.

TABLE 4.3 BOUNDARY CONDITIONS OF THE CASES USED IN THE SENSITIVITY STUDY.

CASE	Fuel	Diluent	d	T_{in} , K	Φ	P, kW	Q_w , kW/m ²	T_{out} , K
B	C ₃ H ₈	N ₂	94	1045	1	1	5.1	1220
D	C ₃ H ₈	N ₂	94	1045	0.33	0.35	3.5	1140
E	C ₃ H ₈	N ₂	94	1045	1.67	1.5	3.8	1180
F	C ₃ H ₈	N ₂	94	1075	1	1	5.3	1250
G	C ₃ H ₈	N ₂	94	1125	1	1	5.6	1290
A	CH ₄	N ₂	71.4	1000	1	2	13	1250
E	CH ₄	N ₂	80	1000	1	2	12	1230
C	CH ₄	N ₂	90	1000	1	2	11	1210
H	CH ₄	CO ₂	71.4	1000	1	2	12	1250

4.3.1 INLET MIXTURE COMPOSITION

In order to investigate the effect of the inlet composition of the fresh mixture, both the thermocouples profiles at the mid-plane and the major species composition at the outlet are examined and compared to the numerical results of FGM. In Figure 4.7, the comparisons between modelled and experimental thermal field are shown for a lean, a rich and a stoichiometric composition, respectively cases D, E and B (see Table. 4.3).

The experimental data (symbols) underline the elevated thermal uniformity of the MILD combustion regime for all the three compositions. Indeed, the difference between the maximum temperature in the burner and the average measured temperature is less than 60 K. Such uniformity is particularly marked because of the high inlet dilution of the conditions under attention ($d=94$). The stoichiometric case B shows the maximum mean temperature. In particular, after the mixing ($0 < y < 0.025 m$) the T_1 profile depicts a steep increase before reaching an almost constant value of 1290 K, whereas the T_c trend is nearly isothermal. As expected, the lean and rich fuel conditions (cases D and E) lead to lower temperatures with respect to the stoichiometric condition B. In particular, the mean temperature for case E is about 50 K lower, whereas, for case D, the decrement is of around 100 K. It can be noted that the more the mean temperature decreases, the more the thermal field is uniform, especially in the central region ($y \approx 0.1 m$).

Regarding the numerical results, they are in a very good agreement with experiments. Nevertheless, the stoichiometric case B is slightly overpredicted along T_1 and underpredicted in the central region of the T_c profile. Such discrepancies are reduced for the rich case E. The case D, on the other hand, shows a very good agreement. For all the cases, however, the very rapid temperature increase near the inlet region is not captured. In this region, in fact, there are high turbulence levels and radiative heat fluxes that, on one side, lead to elevated measurements uncertainties, and, on the other, highlight the weaknesses of the turbulence and radiation models adopted.

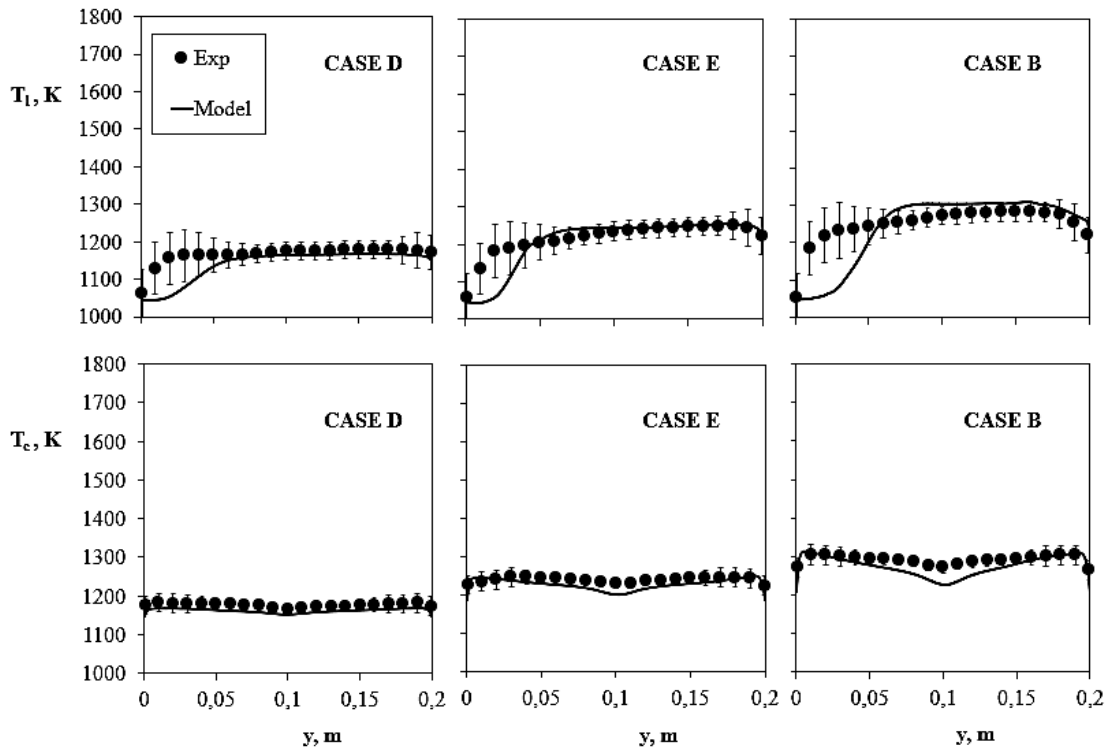


FIGURE 4.7 - MEASUREMENTS WITH UNCERTAINTIES (SYMBOLS WITH ERROR BARS) AND PREDICTED TEMPERATURE BY FGM (SOLID LINES) AT DIFFERENT INLET COMPOSITIONS.

In Figure 4.8, the major combustion products measured at the exit of the burner, CO_2 , CO , H_2 and C_2H_2 (volumetric percentage on a dry basis), were compared with the numerical results for the same three cases. For all the cases investigated, the compositions of NO_x species were negligible. The comparison is reported as a function of the equivalence ratio. It can be observed that the emissions of H_2 , CO and C_2H_2 are very low in lean and stoichiometric conditions, confirming one of the most important characteristics of MILD combustion. The emissions increase for fuel-rich conditions as expected. The modelled compositions are in good agreement for all the species except for CO in stoichiometric conditions (case B). The slight disagreement in the CO prediction for case B might be due to the thermodynamic equilibrium between CO and CO_2 , which strongly depends on the system temperatures [131,132]. Another possible source of disagreement may be related to the effect of recirculation on ignition. In fact, the flow field of the combustion chamber is highly convoluted, and the ignition is influenced by the dilution of the recirculating flow.

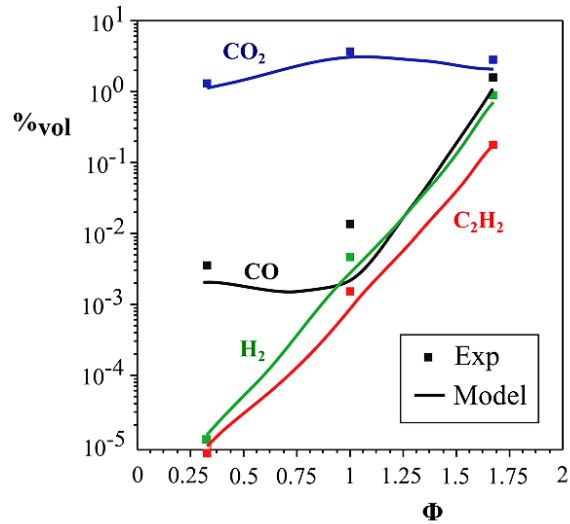


FIGURE 4.8 - COMPARISON BETWEEN THE MEASURED (SYMBOLS) AND MODELLED (SOLID LINES) VOLUMETRIC CONCENTRATIONS OF MAJOR SPECIES AT DIFFERENT INLET COMPOSITIONS.

4.3.2 PREHEATING TEMPERATURE

In a similar way to composition, the effect of the inlet preheating level of the oxidizer jet is investigated by comparing the measured and modelled thermal field at the midplane of the cyclonic chamber. In Figure 4.9 the temperature profiles measured by central and lateral thermocouples are reported as symbols for conditions B, F and G of Table 4.3, which correspond respectively to inlet temperatures of 1045, 1075 and 1125 K. The steep increase of the temperature along T_1 near the inlet is very similar for all the cases, displaying a slight decrease in the ΔT , defined as the difference between the reactor mean temperature and T_{in} , when the preheating temperature is higher. The same degree of isothermality is depicted along the central profile T_c with the trend that shifts toward higher temperatures moving from case B to case F and from the latter to case G. The simulated temperature profiles are reported and depicted with lines. They are in good agreement with the measurements, except for some regions. In fact, at the lateral position, the increase of temperature from the inlet value is delayed, whereas the underprediction along T_c in the central area ($y \approx 0.1 \text{ m}$) discussed for Figure 4.7, is more accentuated for high preheating cases (G and F). The same considerations

about the sources of disagreement between model and experiments made in the previous paragraph can be replicated for these cases.

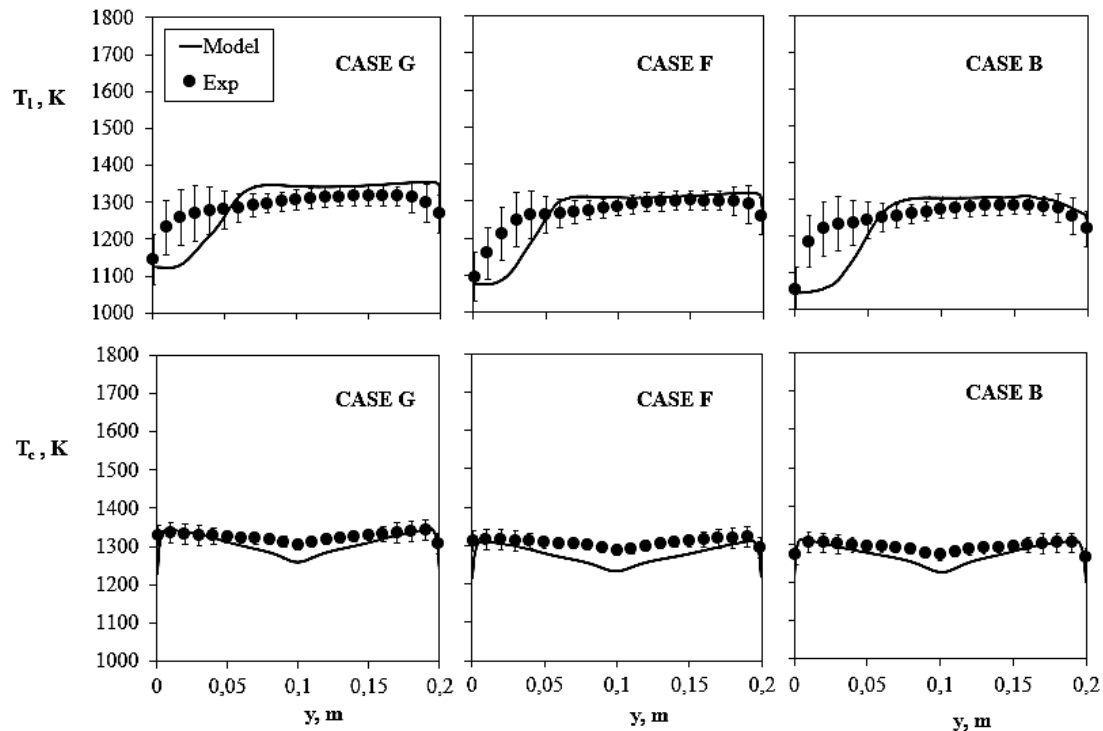


FIGURE 4.9 - MEASUREMENTS WITH UNCERTAINTIES (SYMBOLS WITH ERROR BARS) AND PREDICTED TEMPERATURE BY FGM (SOLID LINES) AT DIFFERENT INLET TEMPERATURES.

From the results shown in this paragraph and in the previous, it can be stated that the model is able to replicate the mean inner temperature of the cyclonic chamber for the conditions under attention. Moreover, an important consideration can be done regarding the performance of the model: FGM allows reproducing the thermal behavior of the cyclonic chamber in a better way for inlet cases with lower reactivity of the inlet mixture (lean and low preheated cases). Such a claim will be supported by the results presented in the following paragraphs.

4.3.3 DILUTION LEVEL

Here, the influence of the external dilution level d is presented by the investigation of three operating conditions reported in Table 4.3. They are related to different amounts

of N_2 in the oxidizer stream: from air condition (case A) to 80% (case E) and 90% (case C) of diluent in the whole fresh mixture. In Figure 4.10, the adiabatic and laminar manifolds of the source term of the progress variable ($\dot{\omega}_J$) and temperature (T), are shown for cases A, E and C. It is worth noting that by increasing the dilution level the maximum source terms and temperatures decrease and move with the stoichiometric mixture fraction. Therefore, the reactivity is strongly reduced by tabulating a highly diluted case, as expected. In particular, for case C, the adiabatic source term of $\dot{\omega}_J$ is about $500 \text{ kg/m}^3\text{s}$, two orders of magnitude lower than the air-dilution case A. The maximum temperature (for J approaching a unit value) goes from about 2500 K for case A to around 1800 K for case C.

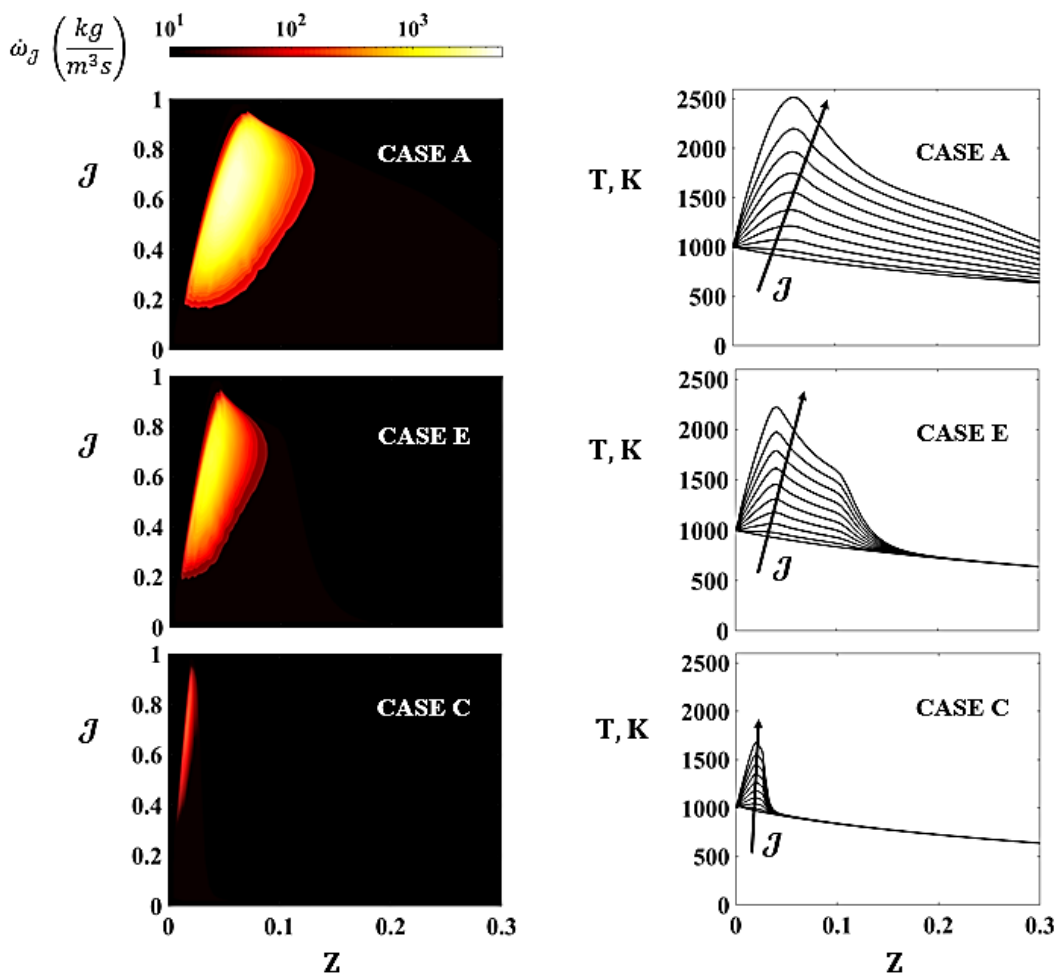


FIGURE 4.10 - MANIFOLDS IN THE Z, J SPACE FOR $\dot{\omega}_J$ (LEFT) AND TEMPERATURE TRENDS AGAINST Z CHANGING J (RIGHT), FOR THREE DIFFERENT DILUTION LEVELS.

In Figure 4.11, the predicted temperature profiles along T_c and T_l are compared to the measured data for the same conditions. The experimental data (closed symbols) show again the high isothermality of the system and the very small temperature gradients even for low dilution cases (A and E). In particular, the thermal field appears only slightly less homogeneous compared to the cases at 94% of the overall dilution level (see Figure 4.7 and 4.9). On the other hand, the numerical profiles (solid lines) present a worse agreement with the experiments, especially along the lateral thermocouple position. Regarding T_c , the cases A and E show an overestimation of about 100 K in the near-wall regions ($0 < y < 0.04$ and $0.16 < y < 0.2$ m). For case C such overprediction is strongly reduced. Such a case, therefore, depicts the best prediction of the data, which corresponds to the more uniform simulated profile.

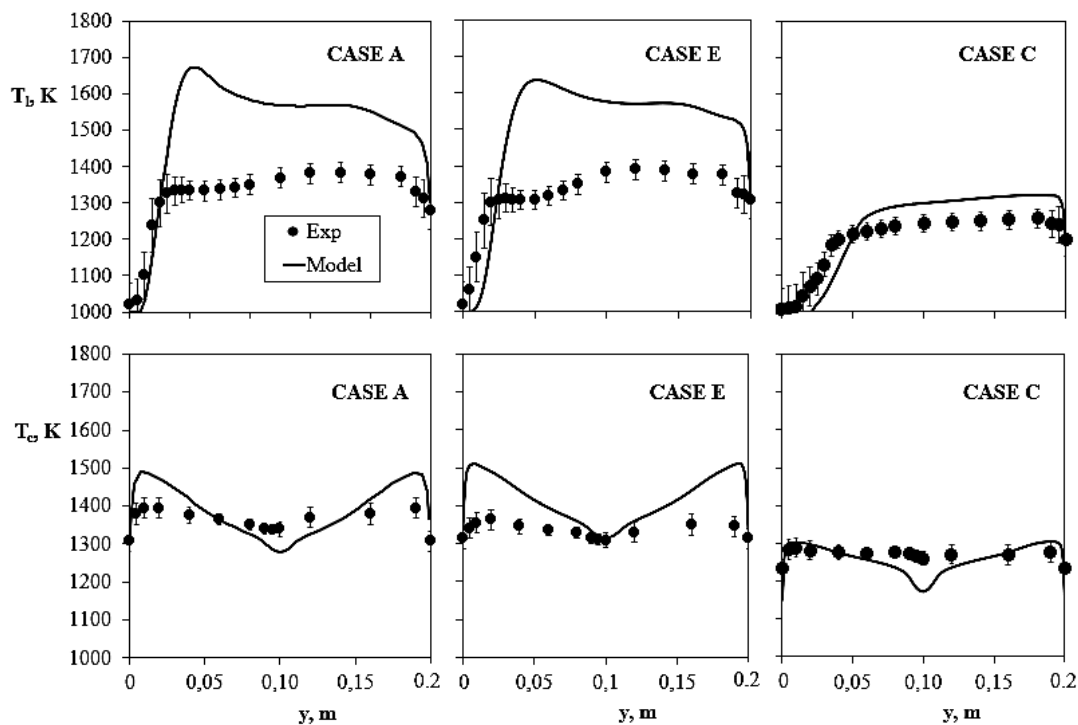


FIGURE 4.11 - MEASUREMENTS WITH UNCERTAINTIES (SYMBOLS WITH ERROR BARS) AND PREDICTED TEMPERATURE BY FGM (SOLID LINES) AT DIFFERENT INLET DILUTION LEVELS.

About the lateral position T_1 , it can be noted that the cases A and E present a strong overestimation of the experimental data (more than 200 K) throughout the y coordinate, with a peak near the inlet. In a similar way to T_c , such disagreement is reduced by increasing the inlet dilution level (case C). Therefore, only for $d = 90\%$, the model FGM predicts with a good agreement with the experimental data along T_1 . The results obtained pointed out that, on the contrary of composition and preheating temperature, the increase of the external dilution level d highly affects the modelling predictions of the cyclonic burner through FGM. As discussed in the previous paragraphs, a more reactive tabulated inlet condition leads to an overestimation of temperature under MILD conditions.

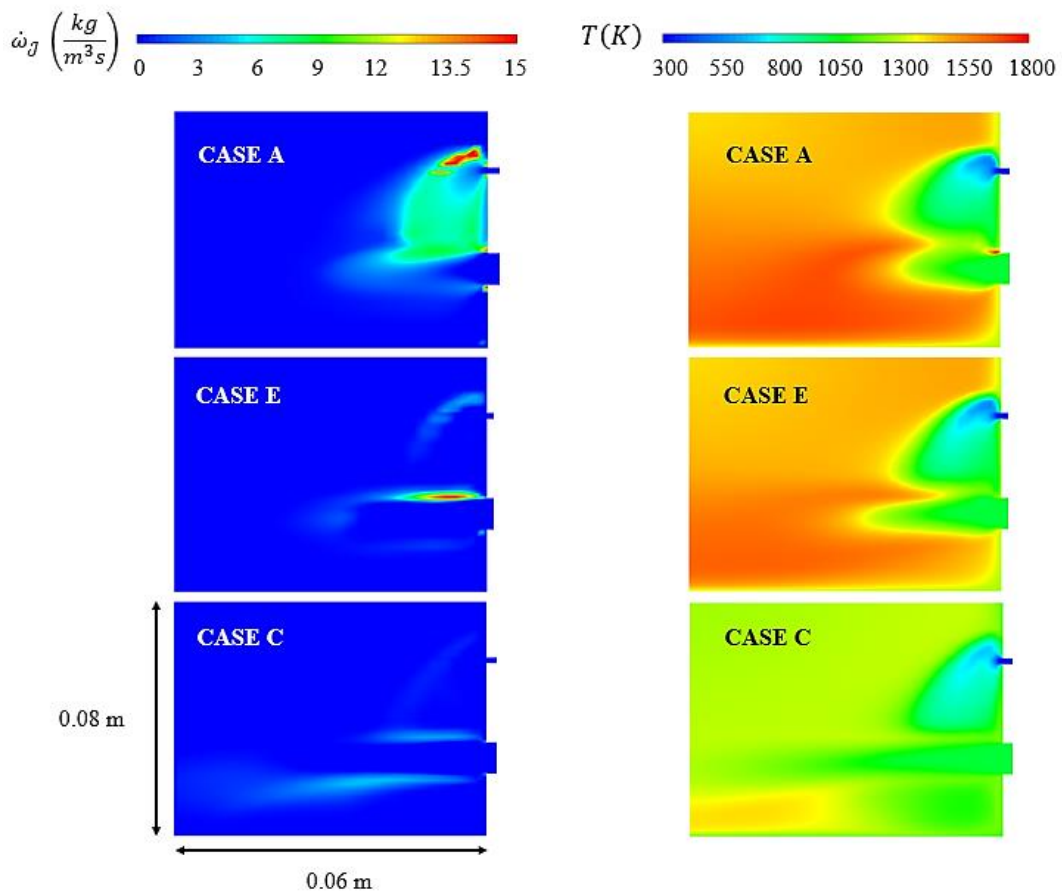


FIGURE 4.12 - CONTOURS OF $\dot{\omega}_j$ (LEFT) THE TEMPERATURE (RIGHT) AT THE INLET REGION FOR THREE DIFFERENT INLET DILUTION LEVELS.

To better understand the reasons for such behavior, the contours of $\dot{\omega}_J$ and the temperature fields in the inlet region are portrayed in Figure 4.12. The region near the inlets (0.08 m along the y-axis and 0.06 m along the x-axis) is illustrated, since, according to the model, this is the only area of the chamber where the system reactivity is located (source terms not negligible). Regarding $\dot{\omega}_J$, the air-diluted case A depicts a distributed source term in the zone between the two nozzles, whereas in the more diluted cases (E and C) this term has a lower magnitude but is more extended around the oxidizer flow. In particular, the most diluted case C presents a maximum value of the reaction rate of about $6 \text{ kg}/\text{m}^3\text{s}$, which is extended to a wide region at the sides of the oxidizer inlet jet. This transition of the reactivity location from the near-fuel region to the surroundings of the oxidizer is due to the modification of the manifolds at higher d , with the decreasing of the stoichiometric mixture fraction (see Figure 4.10). On the other hand, the stretching of the source terms is also related to higher velocities of the oxidizer inlet jet, which are needed to keep the same thermal power for each case. The thermal field, with the lower temperature gradients and the ignition that moves away from the inlet region as the dilution level increases (from case A to C).

In general, it can be concluded that the changing of the dilution level of the inlet fresh mixture affects in a consistent way the predictions of FGM. Particularly, the model is to be able to predict the reactivity of the system for the so-called “MILD external conditions”, i.e. MILD conditions inside the reactor realized by means of inlet operative boundaries (high inlet dilution and preheating). On the other hand, for “MILD internal conditions”, i.e. when the Flameless regime is achieved mainly thanks to the burned gas recirculation (low inlet dilution and no-preheating), the numerical model cannot account for the impact of the internal dilution on the reactivity and, therefore, FGM overpredicts the experimental data at the inlet zone, where the mixing with the exhausts and the following ignition occur.

4.3.4 DILUENT NATURE

Finally, the role of the diluent species is investigated. In Figure 4.13, the adiabatic and laminar manifolds of $\dot{\omega}_J$ and the profiles of T against Z for different J are reported for

cases A and H of Table 4.3. Such conditions related to N_2 and CO_2 as a diluent, respectively.

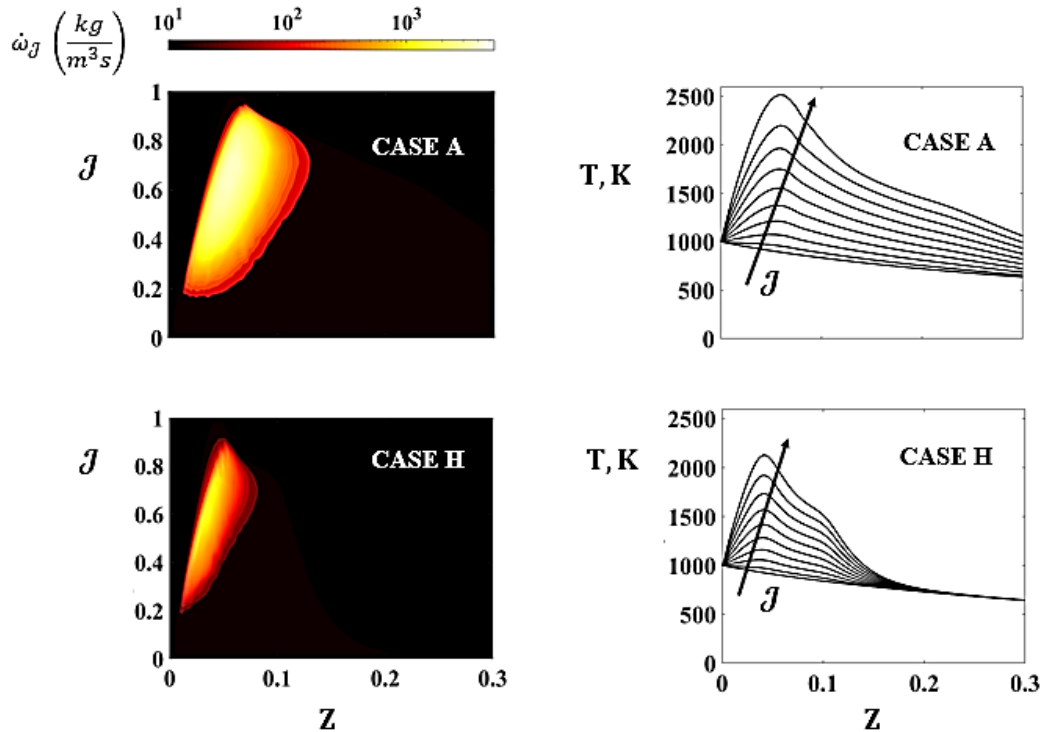


FIGURE 4.13 - MANIFOLDS IN THE Z, J SPACE FOR $\dot{\omega}_J$ (LEFT) AND TEMPERATURE TRENDS AGAINST Z CHANGING J (RIGHT), FOR N_2 (CASE A) AND CO_2 (CASE H) AS DILUENT SPECIES.

The replacing of N_2 with CO_2 (from case A to case H) leads to a decreasing of the reactivity and of the adiabatic temperatures at various progress variables. Therefore, the global effect is the same as that related to the decreasing of the inlet dilution level (see Figure 4.10).

In Figure 4.14, the predicted temperature profiles along T_c and T_1 are compared to the measured data for the two cases. The experimental data (closed symbols) show again the high isothermality of the system and the very small temperature gradients even for the other diluent species. The case H, moreover, indicates a more uniform temperature compared to A, due to the radiative properties of CO_2 . The mean temperature for case H is lower of about 50 K than case A. The general agreement of FGM with the

experiments is strongly improved for the CO₂ dilution. In particular, along the central thermocouple position, the isothermality of the system is reproduced with higher accuracy because of the radiative re-absorption due to the high concentration of carbon dioxide (absorbing/emitting species). The overprediction along T₁, however, is still present, although in a reduced quantity.

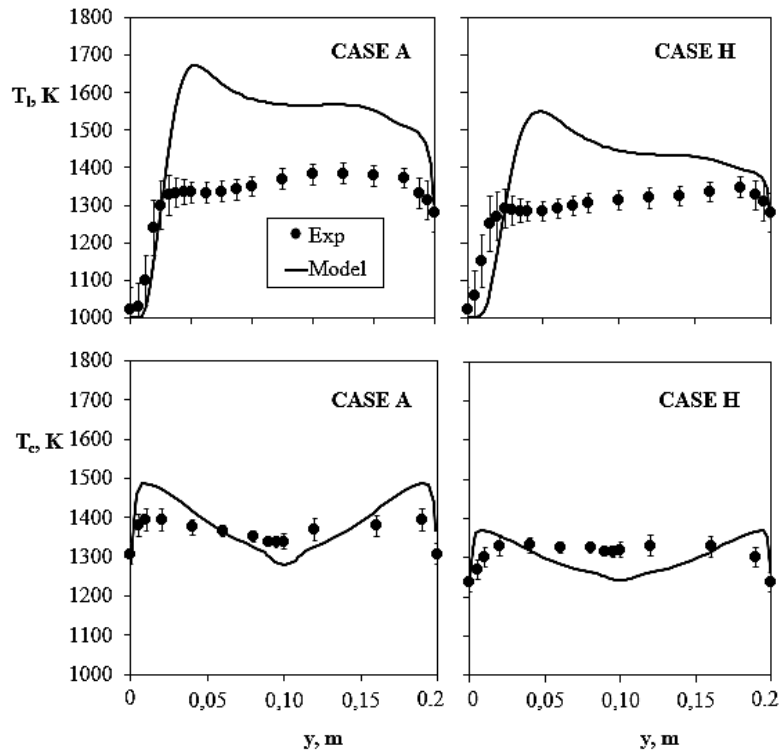


FIGURE 4.14 - MEASUREMENTS WITH UNCERTAINTIES (SYMBOLS WITH ERROR BARS) AND PREDICTED TEMPERATURE BY FGM (SOLID LINES) FOR N₂ (CASE A) AND CO₂ (CASE H) AS DILUENT.

In order to separate the relative contribution (chemistry, heat capacity and radiative properties), in addition to cases A and H, a case H* is numerically investigated as well. For such condition, in fact, a fictitious diluent N₂^{*}, which is N₂ with the radiative properties of the carbon dioxide, is considered in order to evaluate the role of the radiative re-absorption at the CFD level. In Figure 4.15 the contours of $\dot{\omega}_j$ and T for cases A, H and H* are illustrated. It is worth noting that the case H shows almost the same values of reaction rate and temperature as the case E ($d=80\%$) reported in Figure 4.12. This is mainly due to the similarity for their adiabatic and laminar manifolds (see

Figure 4.10 and 4.13), which demonstrate that the increasing of the dilution level d from 71.4 to 80 % produces almost the same reduction of the reactivity that replacing N_2 with CO_2 as the diluent species, for the case with $d=71.4\%$. However, unlike case E, case H shows no reaction rate near the fuel jet. Therefore, the use of CO_2 as diluent leads to the reduction of the reactivity and to the displacement of the reaction zone on the oxidizer jet side. These results are due to both the chemistry and physical properties of the carbon dioxide. Case H*, on the other hand, presents a reaction zone distribution similar to the one of case A but reduced in value.

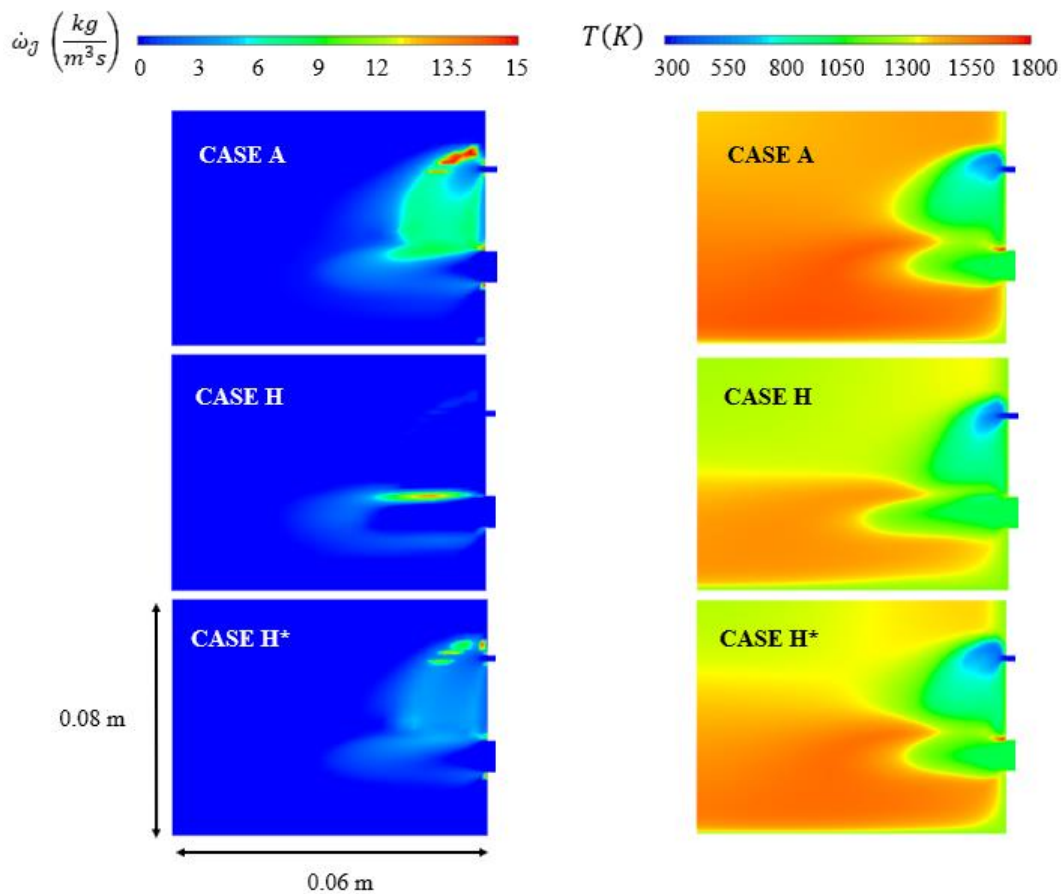


FIGURE 4.15 - CONTOURS OF $\dot{\omega}_j$ (LEFT) THE TEMPERATURE (RIGHT) AT THE INLET REGION FOR N_2 (CASE A), CO_2 (CASE H) AND THE FICTITIOUS SPECIES N_2^* (CASE H*) AS DILUENT.

In order to explain this finding, in Figure 4.16 the comparison between the simulated temperature profiles T_c and T_1 for the same conditions are depicted. Regarding T_c , the

case with fictitious diluent H^* is only slightly different from the case with CO_2 dilution H (around 40 K due to the difference between the heat capacity of CO_2 and N_2), because of in this region the reactivity is negligible and the radiative heat transfer is dominant. On the other hand, T_1 shows that in the inlet zone ($y < 0.08$ m) the temperature trend for H^* follows that of case A (N_2 dilution), confirming the dominant role of the chemistry in the inlet region.

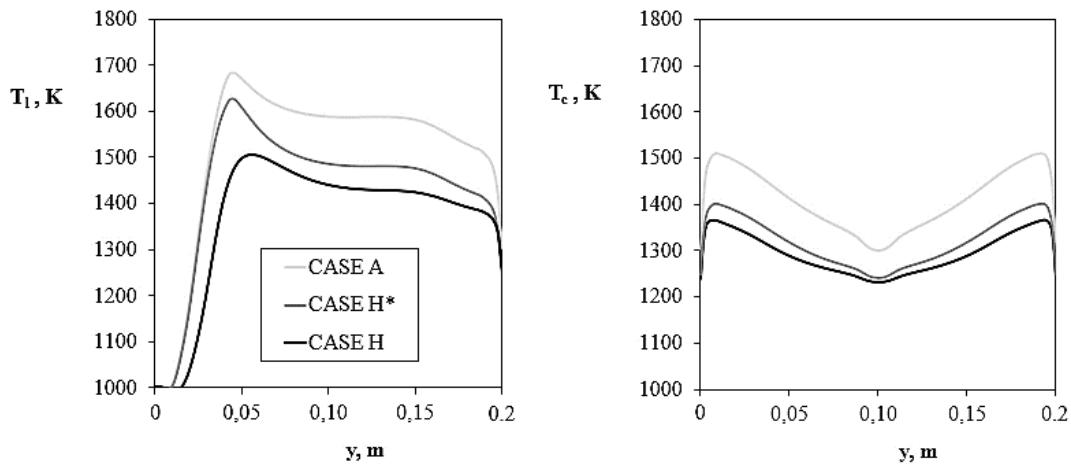


FIGURE 4.16 - NUMERICAL LATERAL (LEFT) AND CENTRAL (RIGHT) TEMPERATURE PROFILES FOR N_2 (CASE A), CO_2 (CASE H) AND THE FICTITIOUS SPECIES N_2^* (CASE H^*) AS DILUENT.

From the results reported and discussed in this section, three main conclusions can be summarized regarding the comparison, varying different operative parameters, between the FGM model and the experimental measurements inside the LUCY burner:

- The measured thermal field under MILD conditions is very uniform for a large range of operative conditions and, in particular, its isothermality is conserved in the absence of external dilution;
- The model is able to predict successfully the MILD temperature field observed experimentally only for cases where the inlet fresh mixture has a small reactivity due, for example, to high dilution, low thermal power and very lean compositions;

- The radiative heat transfer possesses a key role in reproducing the isothermality of the cyclonic chamber.

The last point, particularly, will be analysed in more detail in the next dedicated section.

4.4 Sensitivity on the radiative heat transfer

In order to highlight the importance of the heat transfer mechanism in the modelling of the cyclonic burner, the three conditions reported in Table 4.4 are investigated in this section. Cases A and B are related to a preheating condition with different dilution level, whereas case I represents a non-preheating and non-diluted (air stream as oxidizer) case.

TABLE 4.4 BOUNDARY CONDITIONS FOR CASES A, C AND I.

CASE	Fuel	Diluent	d	T _{in} , K	Φ	P, kW	Q _w , kW/m ²	T _{out} , K
A	CH ₄	N ₂	71.4	1000	1	2	13	1250
C	CH ₄	N ₂	90	1000	1	2	11	1210
I	CH ₄	N ₂	71.4	300	1	2	12.5	1050

In Figure 4.17 the simulated contours of temperature are depicted for case A for a CFD resolution with and without radiation model (see [Paragraph 3.2.3](#)). In particular, neglecting radiation in the CFD means that the total heat loss flux Q_w is only equal to the internal convective heat transfer (see Equation 2.7) and not to the sum between this term and the radiative one (see Equation 2.6). Moreover, in the total enthalpy equation (see Equation 3.30), the radiative source term $\nabla \cdot q$ is equal to zero. From Figure 4.17 it is clear the elevated impact of the radiation model on the uniformity of the simulated thermal field.

The influence of the radiation model is emphasized in Figure 4.18, where the comparisons between the measured temperatures (symbols) and the numerical profiles (lines) obtained with and without radiation model, are reported. The dashed lines represent the temperature profile obtained by considering that all the heat transfer between gases and walls is related to convection, whereas the solid lines refer to the

standard methodology used (with radiation). From this figure, it is confirmed that the radiative heat transfer is crucial to get a good agreement between experimental data and numerical results.

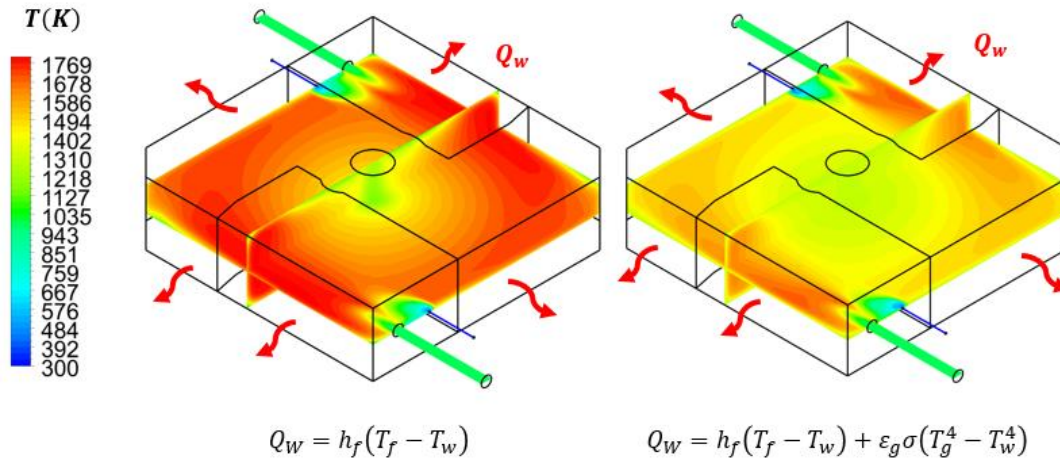


FIGURE 4.17 - SIMULATED TEMPERATURE FIELDS WITHOUT (LEFT) AND WITH (RIGHT) THE INCLUSION OF THE RADIATIVE MODEL. CASE A.

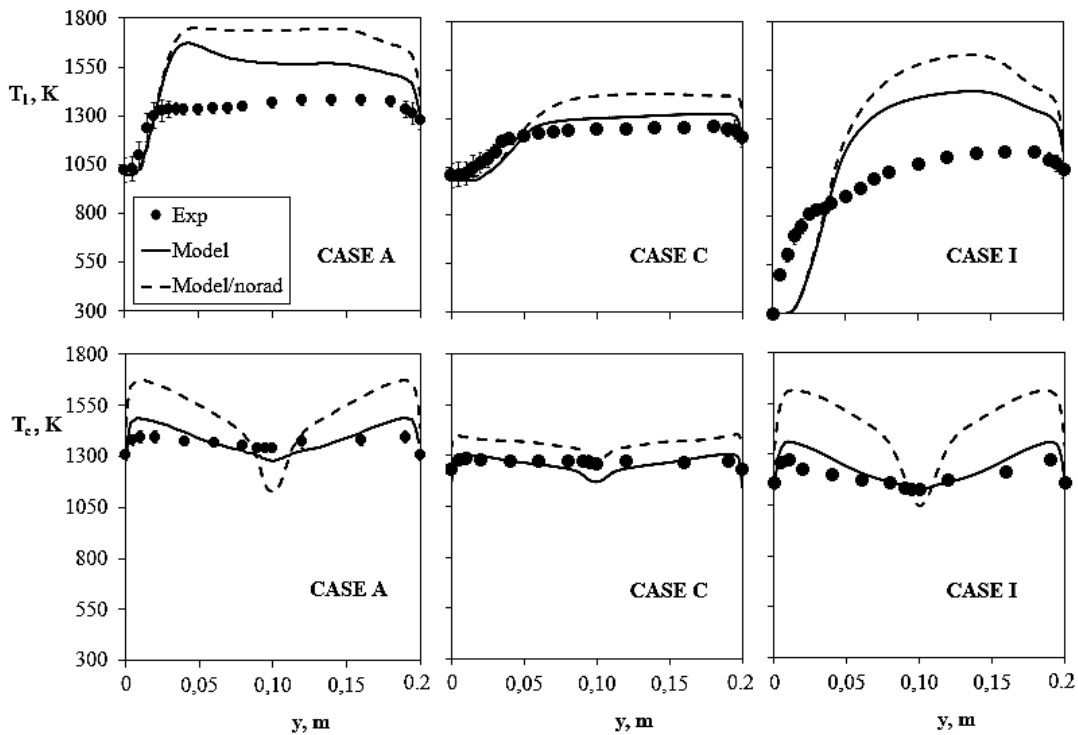


FIGURE 4.18 - MEASUREMENTS WITH UNCERTAINTIES (SYMBOLS WITH ERROR BARS) AND PREDICTED TEMPERATURE BY FGM WITH (SOLID LINES) AND WITHOUT (DASHED LINES) RADIATION MODEL AT DIFFERENT INLET CONDITIONS.

The radiation model allows reproducing the spatial uniformity of the thermal field inside the cyclonic chamber, one of the most important features of MILD Combustion regime. As already commented in the previous section, the low reactive case C shows the best fitting with the experiments. However, for this case the radiation contribute is lower respect to cases A and I. Such a result is expected because of the higher amount of the inert species in the absorbent spectrum N_2 .

In order to understand the reason for such a big impact of radiation in CFD modelling, in Figure 4.19 the contours along the midplane of the volumetric absorbed and emitted radiation are shown. As reported in Equation 3.25, the difference between these two terms gives the radiative heat flux, which modifies the energy equation (see Equation 3.30). The emitted radiation is very high in the ignition zone, where the highest temperature peak is detected, whereas the absorption is maximum in the central part of the cyclonic chamber. This explains how the inclusion of the radiation model leads, on one hand, to reduce the overestimation of the temperatures along T_1 and, on the other, to higher temperatures in the central position (see Figures 4.17 and 4.18).

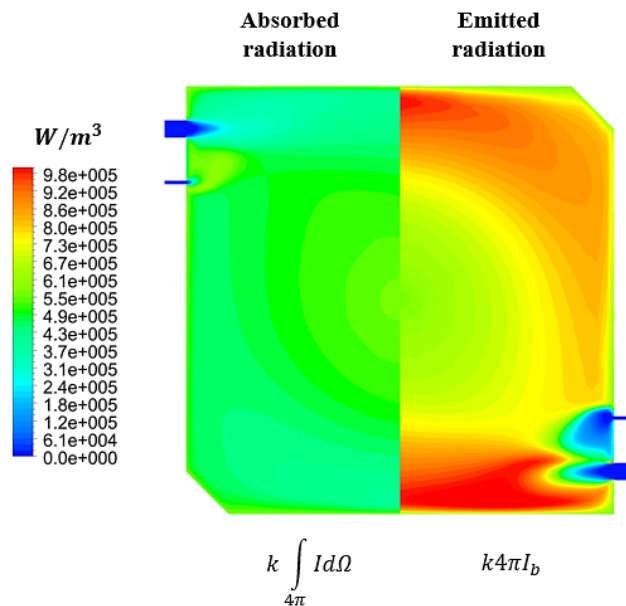


FIGURE 4.19 - SIMULATED FIELD OF THE VOLUMETRIC ABSORBED AND EMITTED RADIATION AT THE MIDPLANE OF THE CYCLONIC CHAMBER FOR CASE A.

In Table 4.5 the temperature uniformity T_u (see Equation 2.10), introduced in [Section 2.5](#), is reported both experimentally and numerically for the cases under attention (see Table 4.4). The measured temperature uniformity T_u^{exp} is very high for all the conditions studied, both for the preheated case A ($T_u^{exp} = 0.96$) and for the non-preheated case I ($T_u^{exp} = 0.92$). Regarding the model, it is estimated how T_u changes not including (T_u^{Norad}) and including (T_u^{FGM}) the radiative heat transfer mechanism. It is found that the gain in terms of thermal uniformity due to radiation is lower increasing the dilution level d (from case A to C), whereas it remains constant decreasing the preheating (from case A to I). In general, the experimental isothermality is better captured considering both radiation and convection mechanisms.

TABLE 4.5 - UNIFORMITY FACTOR FOR EXPERIMENTS AND SIMULATIONS INCLUDING AND NOT THE RADIATIVE HEAT TRANSFER MODELLING.

	CASE A	CASE C	CASE I
T_u^{Norad}	0.80	0.91	0.75
T_u^{FGM}	0.93	0.94	0.88
T_u^{exp}	0.96	0.98	0.92

Furthermore, the importance of radiation can be expressed through the evaluation, for each condition, of the parameter R, defined as

$$R = \frac{T_u^{FGM} - T_u^{Norad}}{T_u^{exp}} \cdot 100 \quad (4.1)$$

This parameter expresses the role of radiation, as a percentage, on reaching the measured temperature uniformity level. The dependence of R on the heat loss flux Q_w is numerically estimated for case A and reported in Figure 4.20. It is worth noting that for the range of heat loss of the system evaluated by experiments (gray band), the gain in terms of isothermality related to the radiative transfer presents a maximum. Near adiabatic conditions (lower Q_w), in fact, the internal heat exchanged in the cyclonic flow by convection makes the thermal field uniform. This also explains the reduced

influence of the radiative model on isothermality for more diluted case (see Figure 4.18 and Table 4.5), which have lower values of heat loss.

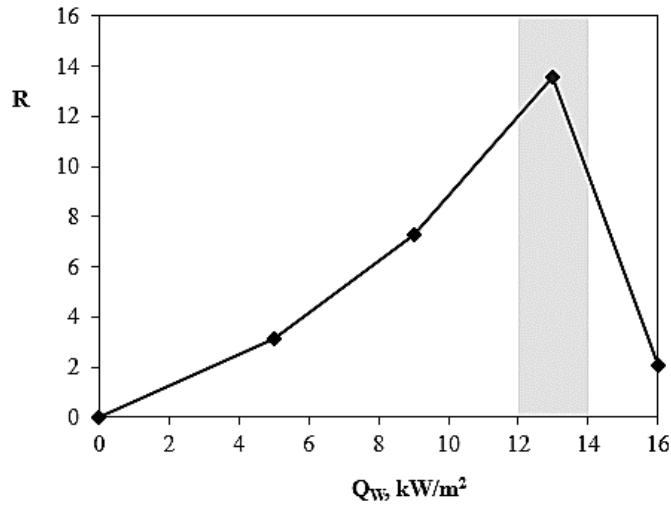


FIGURE 4.20 - ROLE OF RADIATION ON TEMPERATURE UNIFORMITY (EXPRESSED BY THE PARAMETER R) AS A FUNCTION OF THE OVERALL HEAT LOSS BY THE SYSTEM. CASE A.

On the other hand, a very high amount of Q_w means high gradients of temperature between reacting mixture and walls and then a dominant role of the convective heat transfer. Therefore, it is possible to claim that radiation, in this kind of systems, ensures isothermal conditions even for a high level of global heat loss. Such a consideration is very important because, for a MILD reactor, the right level of heat loss at walls is crucial to obtain the desired performance in terms of pollutant emissions.

From the results shown in this section, it can be discussed that, unlike traditional small-size combustion processes, the role of radiative heat transfer in high-EGR combustion systems cannot be ignored and needs to be addressed in a proper way in the modelling activity. The main conclusions can be summarized in the following two points:

- The high uniformity of the temperature observed experimentally under the operative conditions investigated can be numerically reproduced only by including the radiative heat transfer;

- The importance of the radiative heat transfer is amplified, in this kind of system, by the high amount of overall heat loss at walls.

4.5 Comparison with PSR tabulation

In this final section of the chapter, the numerical results of FGM are compared to those obtained by means of a non-adiabatic tabulated chemistry approach [83] for the operative conditions of high dilution and preheating (cases B, D, E, F and G) reported in Table 4.3. Such a model represents an extension of the approach proposed in [89] by performing the PSR calculations over a range of heat loss levels, in order to include the enthalpy as a controlling variable. In Figure 4.21 a scheme of the non-adiabatic PSR calculation performed is depicted. The standard set of unsteady 0D PSR equations are solved and the heat loss sink term Q is included in the enthalpy equation. All the details of the numerical methodology are reported in [83].

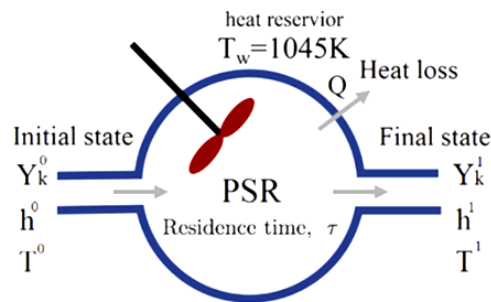


FIGURE 4.21 - SCHEMATIC OF THE NON-ADIABATIC PSR.

At the left side of Figure 4.22, the simulated fields at the half midplane of the mean reaction rate $\dot{\omega}$ and temperature, for case B, are shown. It can be noted that the numerical thermal field is similar to that found with FGM (see Figure 4.2). The reaction zone is located around the oxidized jet in agreement with the distribution of $\dot{\omega}_j$ predicted by the Flamelet model for highly diluted condition (see Figure 4.12), whereas the mean value of $\dot{\omega}$ is higher than the one of $\dot{\omega}_j$. Moreover, on the right side of Figure 4.22, the distribution of $\dot{\omega}$ is depicted in the inlet zone for different cases. It

is worth noting that case D shows a lower and more distributed mean reaction rate, which is stabilized at one side of the oxidizer jet. For such a case, indeed, the composition of the fresh mixture is lean, and the total thermal power is lower than the other cases (0.35 kW). Therefore, the low reactivity of the tabulated inlet condition results in leading to a wider distribution of the reaction rate along the sides of the oxidizer as well as seen for FGM (see Figure 4.12).

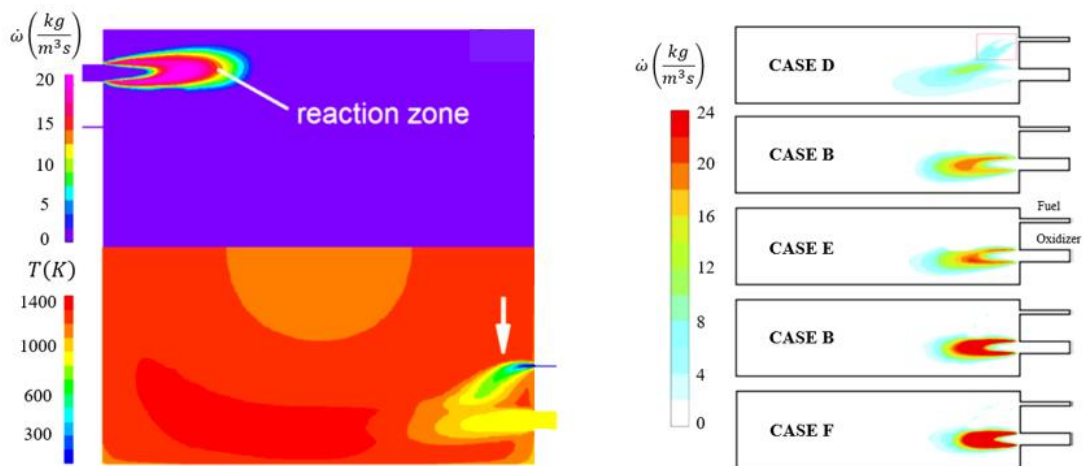


FIGURE 4.22 – MID-PLANE CONTOURS OF THE REACTION RATE AND TEMPERATURE (LEFT) AND REACTION ZONE BEHAVIOR UNDER DIFFERENT MILD CONDITIONS (RIGHT).

In Figures 4.23 and 4.24, the experimental data and the simulated temperature profiles along T_1 and T_c computed, for cases B, D, E, F and G, for the FGM model and the PSR tabulation, are reported. Regarding the cases at different compositions (see Figure 4.23) it can be observed that the non-adiabatic PSR model gives a very good prediction of the data for the lean case D while it overestimates the measured temperatures for the rich and the stoichiometric case E and B. Conversely, the FGM model shows a very good agreement for all the cases as already discussed in [Paragraph 4.3.1](#). The better prediction of the lean case can be explained by the lower reaction rate $\dot{\omega}$ tabulated (see Figure 4.22), which is due to the very low thermal power P (0.35 kW) related to this condition. For the others, the overestimation of the temperatures along the lateral position, of the PSR tabulation compared to FGM is due to the absence of a radiation model for this method. The effect of radiation, in fact, can be safely neglected

for case D due to the very fuel-lean condition and, therefore, the low concentrations of the absorbing species CO_2 and H_2O within the chamber, thus explaining the good agreement with data obtained for case D respect to cases E and B.

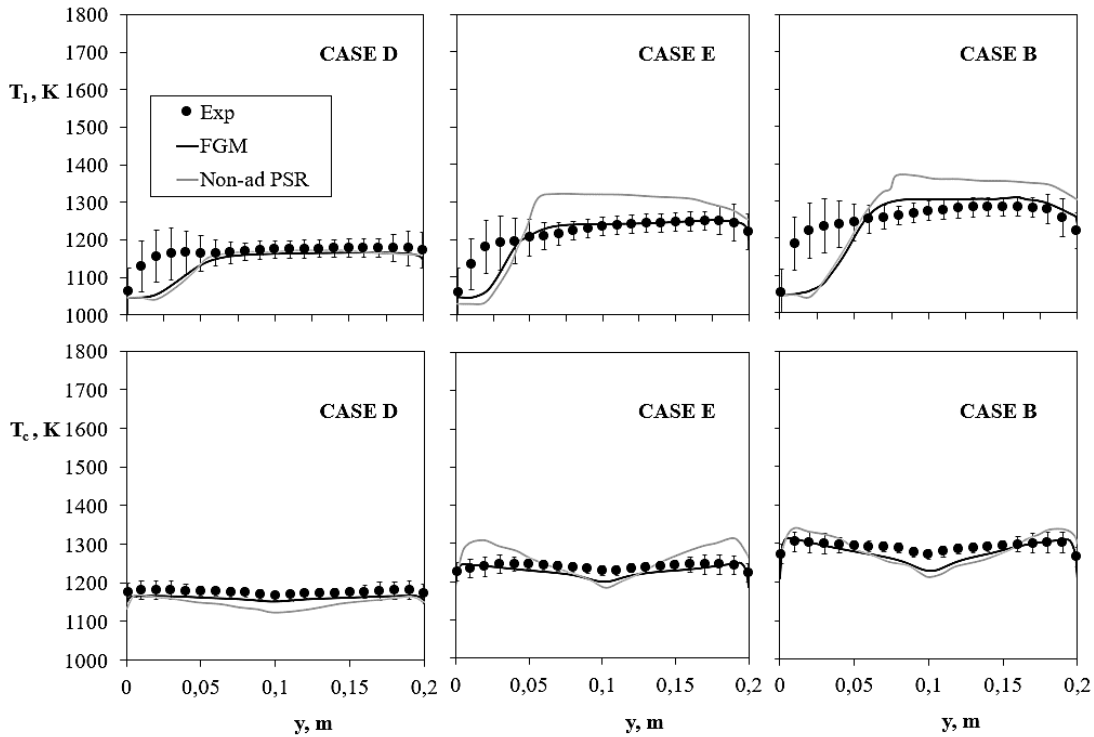


FIGURE 4.23 – MEASUREMENTS WITH UNCERTAINTIES (SYMBOLS WITH ERROR BARS) AND PREDICTED TEMPERATURE BY FGM AND NON-ADIABATIC PSR MODEL (SOLID LINES) AT DIFFERENT INLET COMPOSITIONS.

In Figure 4.24 the same analysis is repeated for different inlet temperatures. The non-adiabatic PSR model still overestimates T_1 respect to FGM. Also, it underestimates the T_c in a stronger way as the inlet temperature increases (from case B to F and from F to G). An underestimation is given by FGM as well but in a reduced way. Again, the general overprediction of the PSR tabulation can be addressed at the neglecting of the radiative heat transfer in the model implementation.

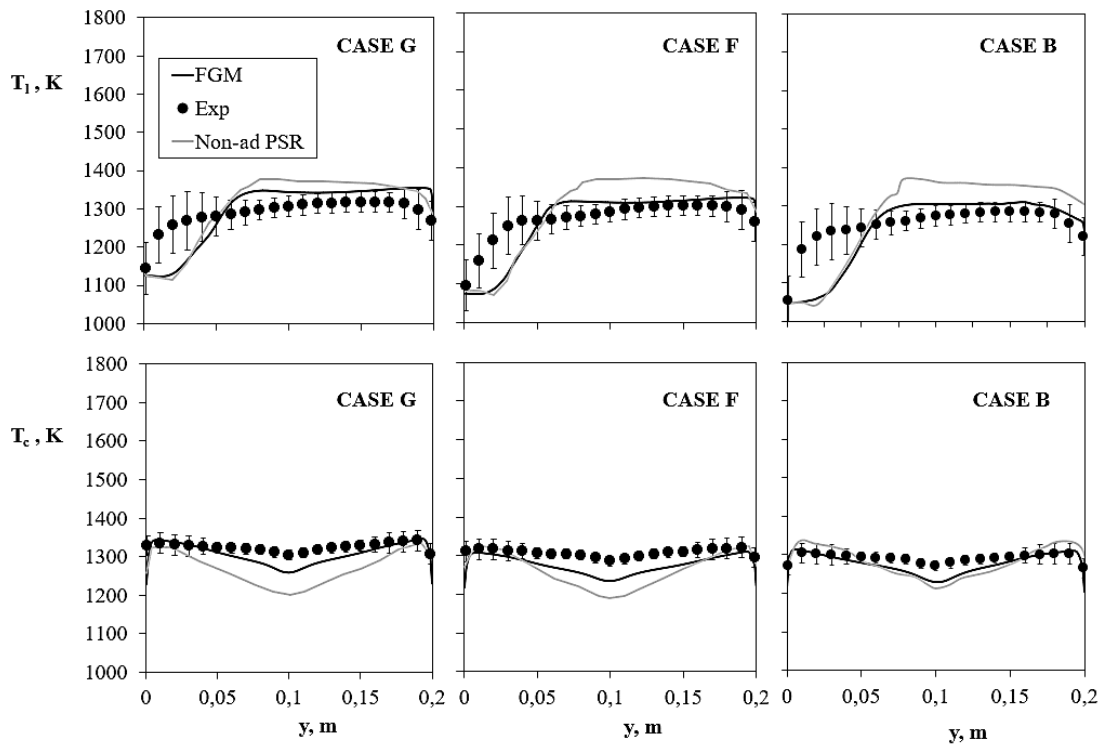


FIGURE 4.24 - MEASUREMENTS WITH UNCERTAINTIES (SYMBOLS WITH ERROR BARS) AND PREDICTED TEMPERATURE BY FGM AND NON-ADIABATIC PSR MODEL (SOLID LINES) AT DIFFERENT INLET TEMPERATURES.

In general, from the comparison shown, it can be pointed out that the performances of both the tabulated chemistry models are severely affected by the reactivity of the tabulated (inlet) conditions. The PSR method, however, shows a bigger sensitivity to the thermal power of the inlet mixture than FGM. For the latter, in particular, the predictions start to worsen only for low dilution levels, when the role of the internal dilution becomes dominant in the establishment of MILD features. The lower temperature homogeneity predicted by the PSR tabulation compared to FGM is likely due to the absence of the radiation model, thus confirming the key role of such a heat transfer mechanism in the prediction of the MILD features for the LUCY burner (see [Section 4.4](#)).

Chapter 5

Reactor Parameters and Manifold Reduction

Following the results reported in the former chapter (see [Chapter 4](#)), a novel methodological approach is here introduced to identify and exploit representative and measurable quantities for MILD reactors in relation to tabulated chemistry reduction methods. First, two main parameters affecting the performance of the cyclonic system are highlighted (see [Section 5.1](#)). Afterwards, a new type of tabulation of the chemistry with a proper manifold reduction based on such parameters is defined (see [Section 5.2](#)). Finally, the results of this approach are analyzed and commented through a comparison with the measured thermal-chemical fields (see [Section 5.3](#)).

5.1 Main parameters of a MILD reactor

The experimental measurements reported in chapter 4 have pointed out that the LUCY burner (see [Chapter 2](#)) presents a moderate and uniform thermal field for a wide range of inlet operative conditions, such as from lean to rich compositions, from no-preheating to high-preheating and from low to high dilution levels. The thermal homogeneity (smoothness of the temperature field), in particular, is one of the most relevant features for modern applications, because of the large-scale uniformity of the sensible enthalpy field due to the small temperature gradients. Such a feature was discussed in [Section 2.5](#) and was commented for all the experimental profiles related to MILD conditions reported throughout chapter 4 (see [Chapter 4](#)).

The performance of the numerical methodology used, based on the tabulated chemistry by means of a progress variable and a mixture fraction, on the contrary, have shown a high dependency on the feeding conditions, leading to an inaccurate modelling when MILD inlet requisites (high level of external dilution) are not fulfilled.

In this context, in order to address the process features (such as the thermal homogeneity) of a MILD reactor, two measurable quantities, related to the design of

such devices, obtained from experiments and reactor analysis, are identified. These parameters are reported in Figure 5.1 together with a sketch of the reactor section at the midplane. The first one is the mean overall heat loss flux at walls through the surroundings, Q_W , evaluated by means of fixed N-thermocouples placed at the exit section (T_{out}) and on the outer and inner surfaces of the burner walls (see [Section 2.3](#)). In particular, the overall wall heat flux Q_W is defined from the global balance as

$$Q_W = Q_F + Q_{OX} + Q_r - Q_{out} - Q_{unb}, \quad (5.1)$$

where Q_F and Q_{OX} are the inlet heat flux of fuel and oxidizer, respectively, Q_r is the reaction heat flux, Q_{out} is the heat flux at outlet and Q_{unb} is the heat flux related to the unburned mixture.

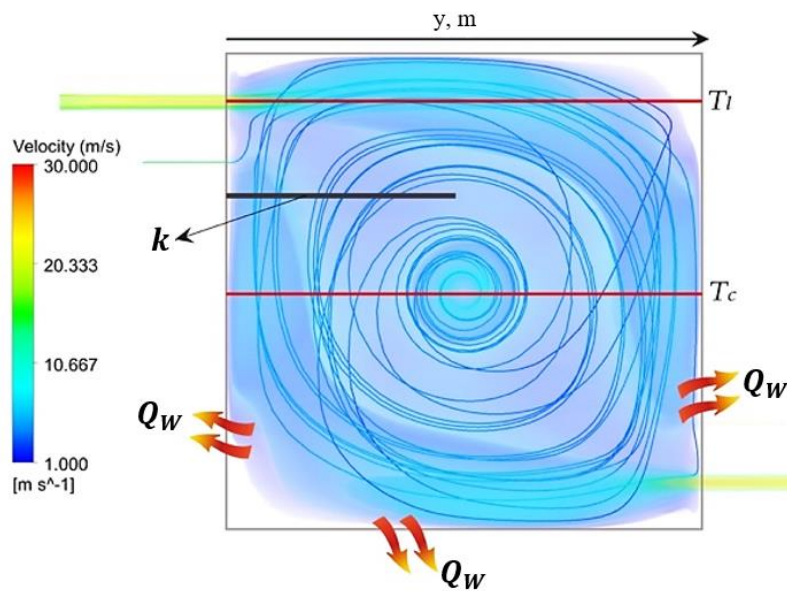


FIGURE 5.1 - SKETCH AT THE MIDPLANE OF THE VELOCITY FIELD OF THE CYCLONIC BURNER WITH THE EVALUATION SECTION OF THE RECIRCULATION FACTOR k (THICK BLACK LINE).

The other reactor design parameter is the recirculation factor k , which can be evaluated from the fluid-dynamics field and defined as the ratio between the recirculated mass flow rate of burned gases and the mass flow rate of the fresh reactants, as follows

$$k = \frac{\dot{w}_{EX}}{\dot{w}_F + \dot{w}_{OX}}, \quad (5.2)$$

where \dot{w}_F , \dot{w}_{OX} and \dot{w}_{EX} are the inlet mass flow rate of fuel, oxidizer and recirculating exhausts, respectively. In particular, the value of k is estimated through non-reacting CFD simulations of the velocity flow. This calculation is computed at a characteristic surface section, reported in Figure 5.1 as a thick black line, in the region of the strong interaction between fuel, oxidizer and recirculating exhausts. Moreover, it was verified that the specific choice of such surface does not influence the calculated value of k .

5.2 Tabulation by means of Diluted Homogeneous Reactor

In order to identify a methodological approach able to consider the internal EGR of a MILD reactor, a new chemistry tabulation method is proposed in this section. Particularly, as highlighted in the previous chapters, the internal dilution due to burned gas recirculation and the effect of heat loss strongly influence system reactivity. Such a methodology aims to consider the reactor measurable parameters k and Q_w in the tabulation procedure. In order to accomplish such objective, a network of ideal reactors developed on the commercial software Chemkin-Pro [133] is used. In particular, the main purpose of this procedure is to mimic the effects on system reactivity and temperature field of the internal dilution of mass and heat.

As discussed in chapter 3 (see [Chapter 3](#)), the numerical simulation of conventional non-premixed combustion systems by means of tabulated chemistry is usually based on the definition of a progress variable, J , and a mixture fraction related to the inlet mixture, Z_0 , [87] as the main controlling variables to parametrize the thermo-chemical state. This technique, schematized in a simplified way at the left of Figure 5.2, relies on the ignition/oxidation of the fresh reactants at various inlet equivalence ratios (various values of Z_0) in 1D or 0D ideal configurations, such as a premixed Flamelet (see Equations 3.5-3.7), batch [134] or PSR (see [Section 4.5](#)). For a non-adiabatic system, a heat loss parameter β related to the ideal configuration is usually defined as well. Therefore, given a fresh mixture with a mass flow rate \dot{w} , inlet sensible enthalpy H_{in} , fuel, oxygen and diluent mass fractions at a fixed inlet mixing level, $Y_F|^{Z_0}$, $Y_{O_2}|^{Z_0}$

and $Y_{DIL}|^{Z_0}$, respectively, the generic thermochemical variable of the system ϕ_i is uniquely determined by each coordinate of the manifold (Z_0, \mathcal{J}, β).

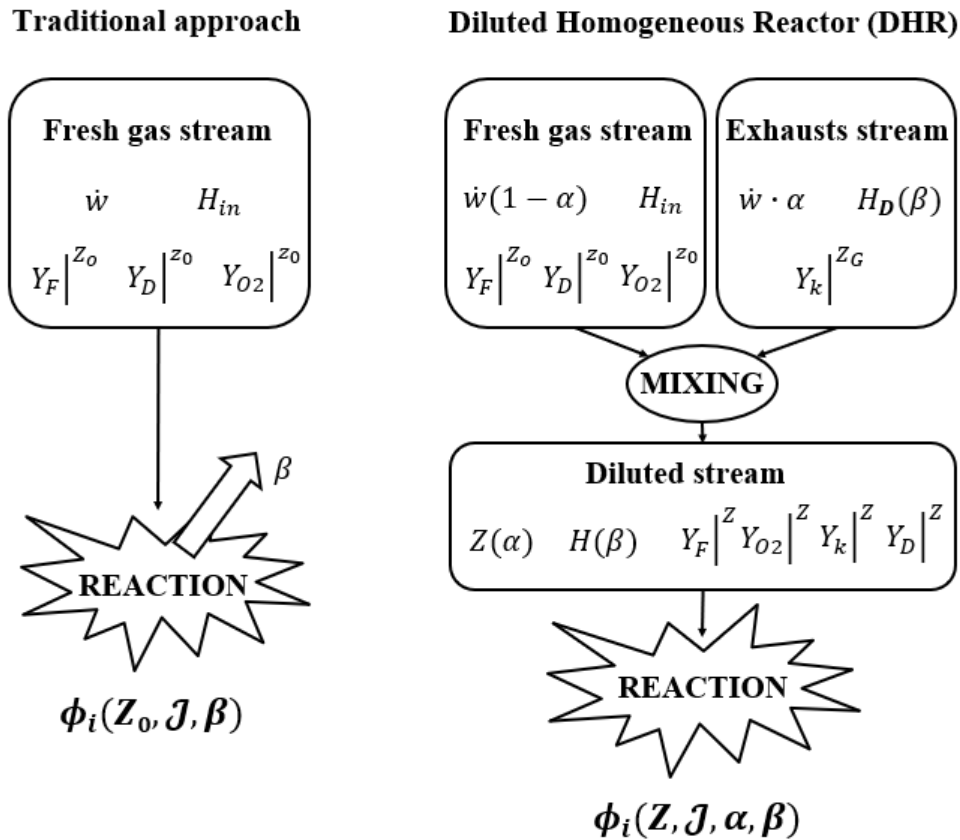


FIGURE 5.2 - FLOW DIAGRAMS REGARDING TRADITIONAL (LEFT) AND DILUTED HOMOGENEOUS REACTOR APPROACH (RIGHT).

The Diluted Homogeneous Reactor (DHR) approach proposed in this work, considers that, for a MILD reactor with elevated internal recirculation of burned products, two main hypotheses may be assumed:

- The mixing between the fresh mixture and burned gas takes place prior to ignition;
- The heat loss only affects the enthalpy content of the recirculating combustion products.

These assumptions are supported by the long residence times required to stabilize such systems leading to values of the Damköhler number close to unity [23,39,64,65]. For instance, regarding the cyclonic burner, the numerical results reported in the previous chapter (see [Chapter 4](#)) have shown that the reactant streams are mixed with each other and with the combustion products as soon as they get inside the chamber (see Figure 4.3). Therefore, before reacting, the fresh gases are diluted and preheated due to the high internal EGR, where the dilution level is controlled by the fluid dynamics whilst the local preheating level is related to the heat loss at the walls. Consequently, on the right side of Figure 5.2, a simplified flow diagram of the DHR configuration is depicted. The fresh stream is mixed with the exhaust stream before reacting in a PSR configuration. The latter consists of the main combustion products, whose mass fractions are denoted as $Y_k|^{Z_G}$, in the thermodynamic equilibrium state at the mixture fraction Z_G , which is the mixture fraction related to the inlet equivalence ratio of the reactants. Indicating the sensible enthalpy of the exhausts as H_D , a heat loss parameter β can be defined as

$$\beta = \frac{H_D - H_{ad}|^{Z_G}}{H_{ign}|^{Z_G} - H_{ad}|^{Z_G}} \quad (5.3)$$

where $H_{ad}|^{Z_G}$ and $H_{ign}|^{Z_G}$ are the sensible enthalpies related to the adiabatic and the ignition temperatures, respectively, for the inlet mixture. The maximum and minimum enthalpy levels ($H_{ad}|^{Z_G}$ and $H_{ign}|^{Z_G}$) used to define β are related to the thermochemical manifold reduction based on the features of the combustion process. In fact, the temperature under reactive conditions cannot be lower than the ignition one because MILD systems rely on autoignition, whereas the maximum enthalpy level is related to the adiabatic state of the feeding condition. Thus, the heat loss factor β represents a dimensionless form of the heat loss flux Q_W .

Furthermore, due to dilution, the overall mass flow rate \dot{w} is split between the fresh and the exhaust streams through the dilution parameter α . Denoting with $Y_i|^{Z_o}$, $Y_i|^{Z_G}$ and $Y_i|^{Z}$ the mass fractions of the species i in the fresh, the exhaust and the diluted streams, respectively, the definition of α reads

$$\alpha = \frac{Y_i|^Z - Y_i|^{Z_0}}{Y_i|^{Z_G} - Y_i|^{Z_0}} \quad (5.4)$$

where the mixture fraction Z of the diluted stream is a function of the dilution level, as

$$Z = Z_0 (1 - \alpha) + Z_G \alpha \quad (5.5)$$

The value of the dilution factor α , therefore, is equal to the recirculating reactor parameter k , thus providing information about the internal EGR level.

Therefore, through such a tabulation, the resulting manifold presents four dimensions and the retrieving of each thermochemical variable of the system, $\phi_i(Z, PV, \alpha, \beta)$, is related to the internal recirculation of both mass and heat.

5.3 DHR tabulation applied to the cyclonic burner

In this section, the DHR tabulating methodology is used for the operative conditions listed in Table 5.1.

TABLE 5.1 BOUNDARY CONDITIONS OF THE CASES USED FOR THE DHR ANALYSIS.

CASE	Fuel	Diluent	d	T_{in}, K	Φ	P, kW	$Q_w, kW/m^2$	T_{out}, K
I	CH ₄	N ₂	71.4	300	1	2	12.5	1165
L	CH ₄	N ₂	71.4	300	1	8	15	1400
M	CH ₄	N ₂	71.4	300	1	8	13	1460
N	CH ₄	N ₂	80	300	1	8	10	1325
O	CH ₄	N ₂	80	300	1	8	8	1380

In particular, the thermal power P , the dilution level d and the heat loss flux Q_w are changed in order to test different α and β operating conditions. Precisely, the heat loss flux at walls is changed by modifying the wall thickness. First, for case I (no preheating of the oxidizer which consists of air stream), the sensitivity of the resulting manifolds on different values of α and β is investigated (see [Paragraph 5.3.1](#)). Afterwards, the

model reliability to capture the mean operational temperature under the MILD regime is tested for the LUCY burner (see [Paragraph 5.3.2](#)).

5.3.1 SENSITIVITY TO THE HEAT LOSS AND DILUTION LEVELS

In Figure 5.3 the temperature profiles simulated with the DHR configuration and related to case I (see Table 5.1) are reported as a function of the diluted mixture fraction Z and parametric in the progress variable J for different values of α and β .

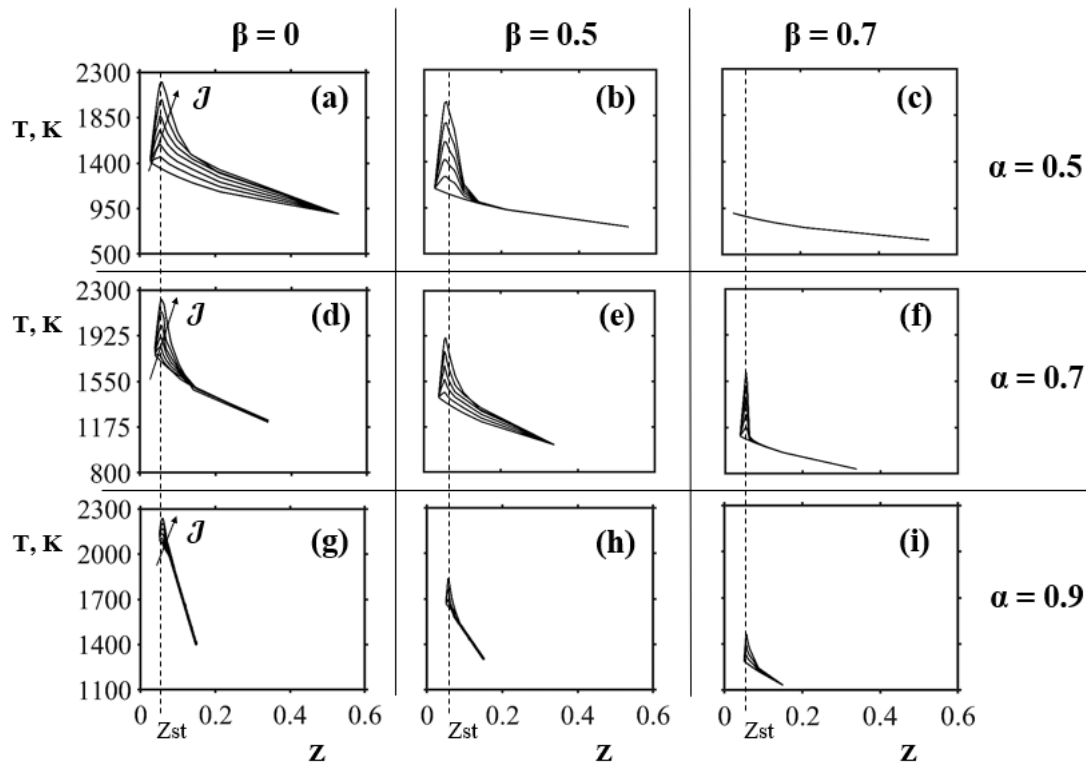


FIGURE 5.3 - DHR SIMULATED TEMPERATURE PROFILES AS A FUNCTION OF THE DILUTED MIXTURE FRACTION Z FOR VARIOUS J AND AT DIFFERENT (α, β) COORDINATES. CASE I.

The heat loss parameter is varied from adiabatic condition ($\beta = 0$) to $\beta = 0.7$, whereas the internal dilution parameter is span between $\alpha = 0.5$ and $\alpha = 0.9$. Values of α lower than 0.5 were not considered because of the absence of reaction. In fact, in this case the fresh stream is not preheated and, therefore, the amount of recirculating mass flow rate must be high enough to preheat above the ignition temperature the diluted

stream (see Figure 5.2). Firstly, it is worth noting that all the profiles in the first column at $\beta = 0$ (a, d and g in Figure 5.3) reach the adiabatic temperature when \mathcal{J} approaches the unit value. On the other hand, the increasing of α leads to the progressive collapsing of the mixture fraction range around the stoichiometric value Z_{st} , which is equal to Z_C for case I. Moving away from adiabatic condition, it can be noted that the effect of the heat loss parameter β is more relevant as α boosts. In particular, for $\beta = 0.7$ (c, f and i in Figure 5.3), the system moves from a non-reacting condition at $\alpha = 0.5$ to a reactive condition with a low increase of temperature of around 200 K at $\alpha = 0.9$.

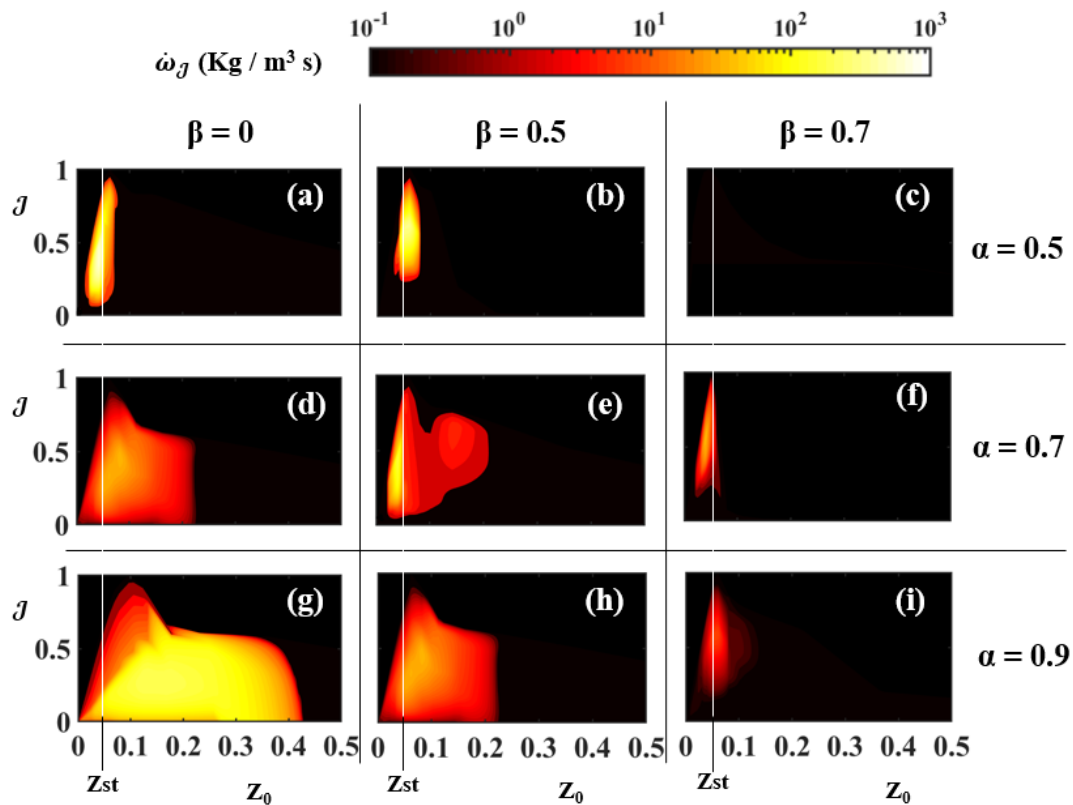


FIGURE 5.4 - DHR SIMULATED MANIFOLDS OF $\dot{\omega}_J$ IN THE (\mathcal{J}, Z_0) PLANE FOR CASE I AND DIFFERENT (α, β) COORDINATES.

In order to better investigate the modification of the system reactivity varying α and β , in Figure 5.4 the manifolds of the source term of \mathcal{J} , $\dot{\omega}_J$, related to the same case (I)

reported in Figure 5.3, are represented. The manifolds are depicted in the (J, Z_0) plane to highlight the spreading of the reactive zone along the Z_0 domain when the dilution parameter increases. For $\alpha = 0.5$ (a, b and c in Figure 5.4), indeed, it can be noted that the reaction zone is located in a small portion of the range of Z_0 , around the stoichiometric value Z_{st} . On the other hand, for $\alpha = 0.9$ (f, h and i in Figure 5.4), the production rate of the progress variable spreads over a wider range of compositions. In addition to the spreading, the reactivity also decreases in intensity for higher values of both α and β . Such a reduction is less marked along β for more diluted conditions (α approaching unit value), allowing the reaction to take place although with a low heat release, so explaining the modest temperature boost (profiles i in Figures 5.3 and 5.4).

5.3.2 DILUTION AND HEAT LOSS CONSTRAINTS FOR THE CYCLONIC BURNER

In this final paragraph, a manifold reduction of the DHR tables based on reactor constraints is presented and discussed. The development of comprehensive reduction tools needs active interconnections between experiments and computations. The elevated internal dilution levels of the LUCY burner, identified by the high values of the recirculating factor k , mean that the fresh reactants are diluted as soon as they are fed inside the cyclonic chamber thus validating the hypothesis required for the utilization of the DHR tabulation. Moreover, inside the burner, the parameters α and β can be considered fairly homogeneous under the MILD operating conditions. In fact, the fluid dynamic field is dominated by the exhausts cyclonic flow due to the burner geometry and the inlet configuration, as showed by the CFD study (see [Section 4.1](#)). Therefore, it can be assumed that, apart from the mixing zone near the inlets, the dilution parameter α is almost constant throughout the chamber. Such behavior is verified by computing the recirculation factor k in several regions of the reactor and by obtaining the same mean value. On the other hand, the heat loss β , normalized between the enthalpy of the products at adiabatic temperature and the one at the ignition temperature (see Equation 5.3), may also be regarded as homogeneous because of the small size of the burner (high exchange surface area at the walls) and the radiative heat transfer. The latter effect, in particular, was proved to have a dominant role on the uniformity of the temperatures inside a MILD combustion system

due to both the cavity behavior of the walls and the radiative reabsorption of the exhausts (see [Section 4.4](#)). Following such considerations, it can be inferred that inside the cyclonic burner under MILD regime there is a very small variability of internal dilution and heat loss parameters and mean values of α and β can be estimated. Therefore, for each condition reported in Table 5.1, a mean α_m is defined as equal to the recirculation factor k calculated by CFD, as

$$\alpha_m = k, \quad (5.6)$$

whereas a mean β_m , evaluated assuming the enthalpy of the exhausts stream equal to the enthalpy of the exit flow experimentally measured, H_{out}^{EXP} , reads

$$\beta_m = \frac{H_{out}^{EXP} - H_{ad}|^{Z_G}}{H_{ig}|^{Z_G} - H_{ad}|^{Z_G}}. \quad (5.7)$$

In the upper part of Figure 5.5 (see from a to c), the measured temperatures profiles along the thermocouples positions T_c and T_l are reported for the non-preheated cases I, M and L (see Table 5.1). In the lower part of the Figure (see from d to i), for the same cases, the profiles of T and $\dot{\omega}_J$ calculated by means of the DHR tabulation are reported against the inlet mixture fraction Z_0 at different J and for the fixed estimated values α_m and β_m . Therefore, in the figure, the experimental thermal fields are basically associated to the numerical temperature ranges of the reduced manifolds of coordinates $(J, Z_0, \beta_m, \alpha_m)$. These temperature ranges are marked by the gray areas in the experimental domains (from a to c). It can be noted that such a gray regions include the whole central profile T_c and half of the lateral one, T_l . The only exception is related to the inlet zone (T_l profiles at $0 < y < 0.05 \text{ m}$) where the mean values of β_m, α_m are still not reached. This means that the reduced manifolds are able to give a reliable indication about the measured temperature ranges and the maximum temperatures inside the cyclonic burner (except for the inlet region). Moreover, it is worth noting that for the cases at higher thermal power M and L ($P=8 \text{ kW}$), which experimentally show a greater thermal uniformity than case I ($P=2 \text{ kW}$), the gray regions are thinner because of the lower temperature increases (see from d to f). Although their bigger thermal power, in fact, the reactivity for these cases is reduced by the higher internal dilution level ($\alpha_m = 0.95$). The tabulated $\dot{\omega}_J$ for cases M and

L, in fact, are almost one order of magnitude lower than case I and they spread over a wider range of Z_0 due to dilution (see from g to i). The heat loss effect, on the other hand, moving from case M and L, does not have a big influence on the reaction rate range as dilution does (see h and i).

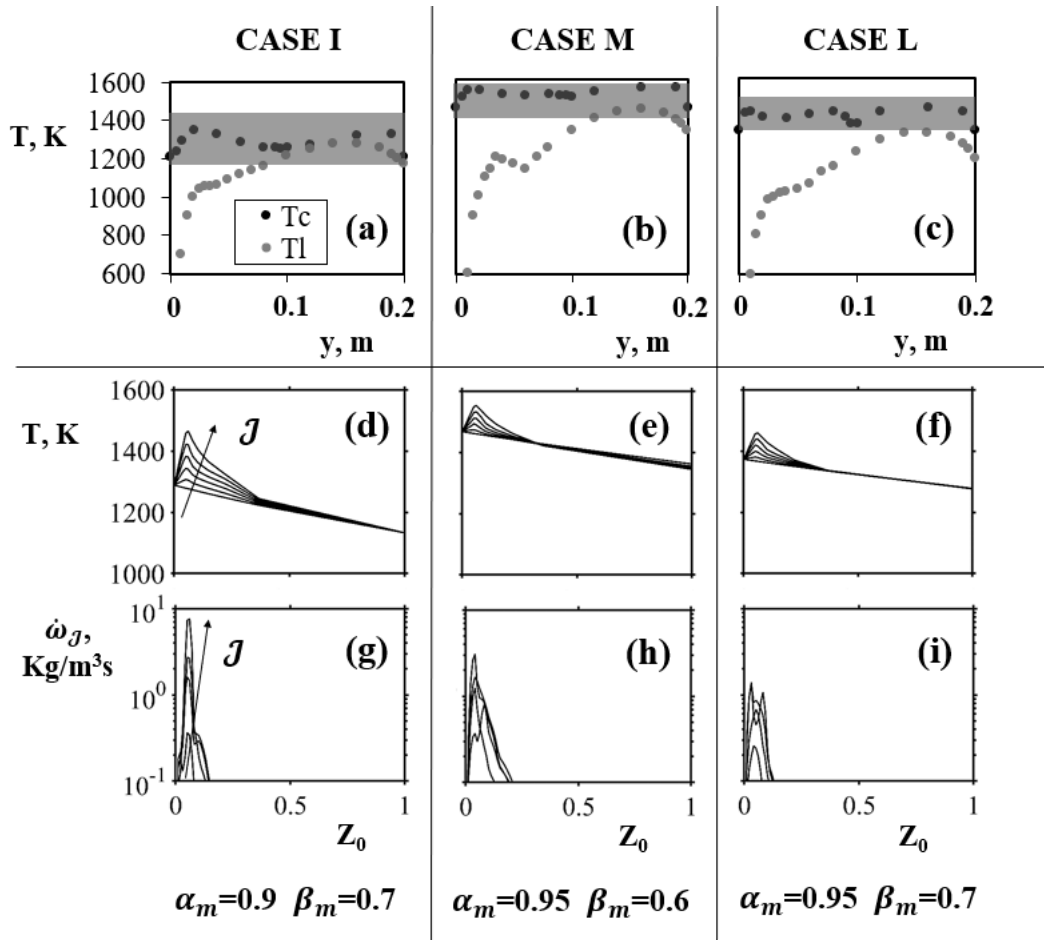


FIGURE 5.5 - MEASURED TEMPERATURE PROFILES INSIDE THE CYCLONIC BURNER (A-C); AND DHR TEMPERATURE AND $\dot{\omega}_J$ SIMULATED FOR ESTIMATED OPERATIONAL MEAN VALUES OF α AND β (D-I) FOR CASES I, M AND L.

In Figure 5.6, the same analysis is repeated for the cases O and N (see Table 5.1). For those cases, the elevated inlet velocities required to reach the operative thermal power lead to a very high mean internal dilution level ($\alpha_m = 0.98$) and, therefore, the source terms of the progress variable are around 0.1 Kg/m³s (see e and f), which is an order of magnitude lower than cases M and L (see Figure 5.5). Thus, the mixing region

where the mean values of β_m, α_m are not reached is extended throughout T_1 and only the central profile T_c is included in the gray regions. Moreover, T_c depicts a higher uniformity (see a and b) in agreement with the very thin gray regions due to the low-temperature increases in the reduced manifolds (see c and d).

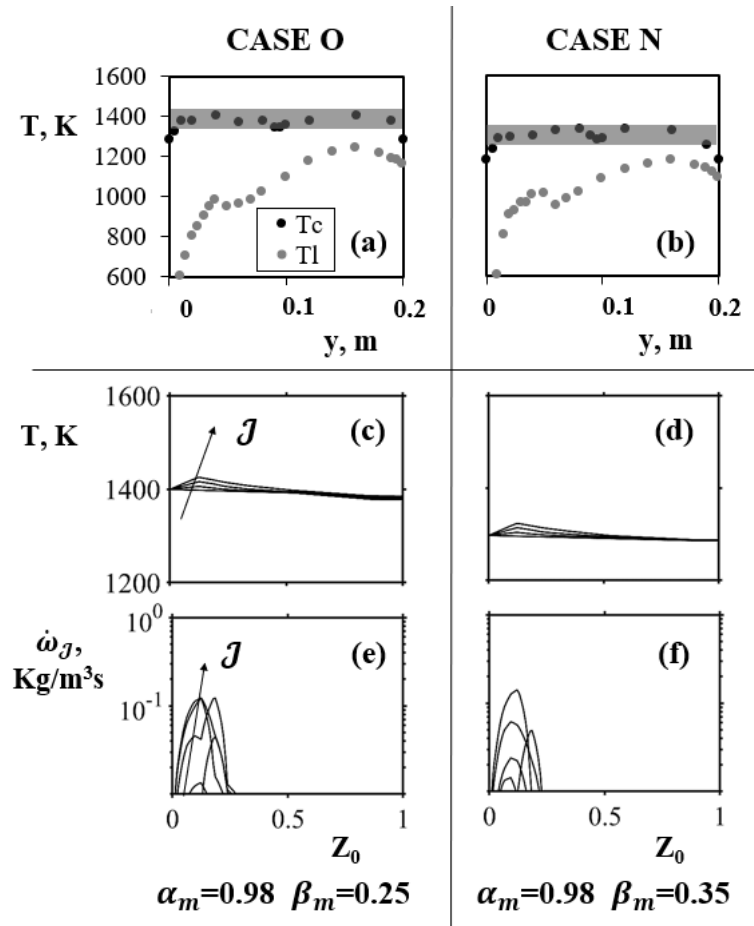


FIGURE 5.6 - MEASURED TEMPERATURE PROFILES INSIDE THE CYCLONIC BURNER (A-C); AND DHR TEMPERATURE AND $\dot{\omega}_J$ SIMULATED FOR ESTIMATED OPERATIONAL MEAN VALUES OF α AND β (D-I) FOR CASES O AND N.

Therefore, the reduction of the thermo-chemical manifold (Z, J, α, β) for a MILD system by using significant reactor parameters related to operating constraints, has led to very good results. In fact, such results highlight the reliability of the DHR tabulation methodology for MILD Combustion systems with elevated internal EGR since it takes into account the combined effect of heat loss and internal dilution. The 4D tabulation,

in fact, is able to store the characteristic very low and distributed reaction rates of these systems thus allowing to reproduce the low-temperature gradients and the highly isothermal behavior of a MILD reactor. Therefore, it can be stated that the DHR tabulation represents a very valuable tool for the future development of a comprehensive CFD model for such a kind of systems in order to reproduce their reacting behavior for a wide range of inlet conditions.

Chapter 6

Conclusions and Future Perspectives

In this last chapter the main conclusions of this thesis work are discussed (see [Section 6.1](#)). Moreover, following the results obtained, an outlook to the future developments is also reported (see [Section 6.2](#)).

6.1 Conclusions

In this thesis, the author points out the main features of a MILD reactor, regarded as a system where the MILD conditions are stabilized as a result of high internal recirculation of exhausts (see [Chapter 1](#)). By means of the literature study conducted, the role of the heat transfer in these systems to reach their performances and homogeneous conditions is highlighted. In particular, the different heat transfer mechanisms involved were reported and discussed. The internal heat transfer mechanisms were found to be crucial both for convection and radiation modes. On one hand, the high velocities, required to ensure good levels of internal recirculation, increase the convection term. On the other hand, the recirculation of the internal product (mainly H₂O/CO₂ mixtures) are involved in the radiative re-absorption. It was also discussed how MILD systems behave as a quasi-black body cavity due to their confined enclosures.

In order to characterize those systems, an interconnected numerical and experimental study was carried out on a novel cyclonic burner (see [Chapter 2](#)) operating under MILD combustion conditions. It represents a compact combustion system where the feeding configuration geometry is such to guarantee the required recirculating levels. Moreover, by carrying out a theoretical analysis it was found that, in this MILD reactor, the radiation is the dominant heat transfer mechanism between reactive mixture and walls under MILD conditions.

The CFD results were compared with the measured data focusing the attention on the temperature field. The modelling was performed by using a Flamelet/tabulated-chemistry paradigm (the FGM model) with a presumed β -PDF approach to treat the chemistry/turbulence interaction, whereas the radiative heat transfer was considered with the DO model to solve the RTE and a modified WSGG model to obtain the absorption coefficient at different temperature and compositions of the mixture $\text{CO}_2/\text{H}_2\text{O}$ (see [Chapter 3](#)).

Several operational conditions were investigated varying different operating parameters for which the MILD conditions persist. Two different fuels, CH_4 and C_3H_8 , were used as the fuel stream whereas a mixture of diluent and O_2 as the oxidizer. Both N_2 and CO_2 were investigated as diluents where their amount defines the overall dilution level d of the system. The oxidizer stream was fed both at environment temperature and in preheated conditions whereas the fuel was not preheated. The amount of fuel at the inlet was changed in order to investigate different thermal power P . Finally, the relative composition between fuel and oxygen was also varied (Φ). According to the model, the central position of the chamber is dominated by the heat transfer whereas the reactivity is located in the inlet region. The system pressure was kept fixed at atmospheric conditions. The comparison between FGM and experiments was mainly carried out by depicting the measured and simulated temperature profiles along the positions of two movable N-thermocouples, one placed at the centreline of the oxidizer nozzle and the other parallel to the previous one but located in the centre of the chamber, between the two inlets. In order to value the performances of FGM and detect the key features of the system, the comparisons were reported to varying of different model settings and inlet boundaries (see [Chapter 4](#)). Regarding the model settings, two different 1D configurations were used to tabulate the chemistry: a non-premixed unsteady (IML) and a premixed steady flame. It was found that the results are only slightly affected by the Flamelet paradigm in the ignition zone, where IML predicts an early ignition due to diffusion effects. Moreover, the use of premixed flame led to an overestimation of temperature and reactivity outside the flammability limits where interpolation is made. The kinetic mechanism, on the other hand, has a bigger impact on the predictions and a detailed one must be used. Regarding the comparisons at different inlet conditions, it was shown that, for highly diluted cases, changing both

inlet compositions and temperature of the oxidizer stream does not affect the simulation results. On the contrary, for a given condition, decreasing the inlet dilution level leads to a strong overestimation of the measured profiles. The diluent nature likewise changes the agreement of FGM with data. The case with CO₂ as diluent instead of N₂, in particular, predicted better the data due to the radiative reabsorption of the carbon dioxide that tends to make the temperature field uniform. This behavior, indeed, was demonstrated by conducting simulations without the radiative heat transfer model. It is worth noting that only by including radiation in the model, the experimental thermal uniformity of the LUCY burner can be reproduced. Furthermore, it was found that the importance of radiation in enhancing the predictions of the model changes for different heat loss levels. This dependency represents an important finding since a MILD reactor relies on the heat loss at walls to reach the characteristic low temperatures and avoid pollutant emissions. Afterwards, the FGM results were also compared to those obtained with a 0D tabulation based on PSR, where the heat loss was included in the tabulation by subtracting heat from the ideal reactor. The predictions, in this case, show worse agreements with experiments respect to FGM, especially for the most reactive cases considered. Such behavior is likely due to the absence of a radiation model for the PSR tabulation method.

In general, the model is able to predict successfully the MILD temperature field observed experimentally for cases where the inlet mixture has a low reactivity (MILD external conditions), such as high dilution and low thermal power, whereas it tends to overestimate the experiments high reactivity cases, such as low dilution and high thermal power. In the latter case, in fact, the reaction is ruled by the internal dilution (MILD internal conditions) which is not accounted in the FGM tables. The radiative heat transfer has a key role in reproducing the thermal uniformity of the cyclonic chamber. Moreover, for low external reactivity (good prediction of the thermal field) the location of the reaction zone predicted by the model is around the oxidizer jet. The experimental temperatures, unlike the simulated profiles, showed a high level of thermal uniformity for all the cases investigated. For most reactive conditions, in particular, the almost isothermal trends of temperature just translate to higher values.

To address the role of the internal dilution in a MILD reactor like the LUCY burner and in order to explain the low dependency of such system on the operational inlet

boundaries, two reactor parameters are assumed to characterize the burner at each MILD condition: a heat loss parameter β and an internal dilution parameter α (see [Chapter 5](#)). Therefore, a new tabulation method based on diluted PSR which allows tabulating all the thermochemical variables as a function of α and β in addition to J and Z was defined. In such a way, the intrinsic coupling of internal dilution and heat loss is successfully considered. Furthermore, by evaluating mean values for α and β by means of both numerical and experimental analysis, the reduced manifolds in the (Z, J) plane related to these mean values were compared to the measured thermal fields. The results showed comparable temperature ranges, so confirming the hypothesis made. In synthesis, the constraints imposed on both internal dilution and heat loss allow identifying a small domain where the system reactivity relies in a narrow range of reaction rates. This makes possible to identify a dimensional lower thermo-chemical manifold where the source term is quite uniform thus reproducing the low and distributed reactivity that is typical of MILD systems.

6.2 Future perspectives

In chapter 4, the numerical results demonstrated that FGM is a valuable choice to model the MILD combustion conditions, but its performance is strongly dependent on the ranges of operational inlet boundaries considered. In fact, the model ensures very good predictions only when the MILD regime is established by feeding a low reactive inlet mixture inside the system. Indeed, the progress variable/mixture fraction approach does not take into account the modification of the reactivity inside the chamber due to the internal dilution of mass and heat related to recirculating diluent and combustion products. The inclusion of the internal EGR in the tabulation process through a diluted PSR, confirmed that in a MILD reactor like the cyclonic burner studied in this thesis, this contribution is essential. Therefore, the development of a complete CFD model based on the tabulation procedure presented in chapter 5, represents the main outlook coming out from this study. In fact, it would permit to reproduce the MILD conditions for the whole operational range of the reactor. In literature, there are examples of numerical modelling of combustion systems with a high level of internal recirculation by using the tabulation of both internal dilution and

heat loss [80,88]. However, in such works, the transport equation for the dilution factor α usually presents a dilution source term whose definition does not rely on solid physical basis. Thus, it would be of great value to develop a CFD methodology able to track the internal dilution of both mass and heat by means of proper scalar quantities. Moreover, since radiation was proved to be a key parameter in reproducing MILD thermal uniformity, a more detailed non-gray gas model should be also used. Another key improvement of the presented study would be the implementation of LES simulations to better characterize the cyclonic flow and the mixing/reacting structures. Finally, the analysis conducted in order to reduce the manifold dimension based on reactor constraints for a MILD combustion system may particularly attractive in the digital twin framework, with possible application in monitoring, diagnostics and prognostics [76].

References

- [1] EIA U. International energy outlook 2019. <https://www.eia.gov/outlooks/ieo/pdf/ieo2019.pdf>.
- [2] Cavaliere A, de Joannon M, Sabia P, Sorrentino G, Ragucci R. Highly preheated lean combustion. *Lean Combust. Technol. Control* Second Ed., 2016. <https://doi.org/10.1016/B978-0-12-804557-2.00003-1>.
- [3] Li PF, Mi JC, Dally BB, Wang FF, Wang L, Liu ZH, et al. Progress and recent trend in MILD combustion. *Sci China Technol Sci* 2011;54:255–69. <https://doi.org/10.1007/s11431-010-4257-0>.
- [4] Rao GA, Levy Y. A New Combustion Methodology for Low Emission Gas Turbine Engines. 8th Int. Symp. High Temp. Air Combust. Gasif., 2010.
- [5] Hottel HC, Cohen ES. Radiant heat exchange in a gas-filled enclosure: Allowance for nonuniformity of gas temperature. *AIChE J* 1958. <https://doi.org/10.1002/aic.690040103>.
- [6] Minamoto Y, Dunstan TD, Swaminathan N, Cant RS. DNS of EGR-type turbulent flame in MILD condition. *Proc Combust Inst* 2013. <https://doi.org/10.1016/j.proci.2012.06.041>.
- [7] Göktolga MU, Van Oijen JA, De Goey LPH. 3D DNS of MILD combustion: A detailed analysis of heat loss effects, preferential diffusion, and flame formation mechanisms. *Fuel* 2015. <https://doi.org/10.1016/j.fuel.2015.07.049>.
- [8] Ranzi E, Frassoldati A, Grana R, Cuoci A, Faravelli T, Kelley AP, et al. Hierarchical and comparative kinetic modeling of laminar flame speeds of hydrocarbon and oxygenated fuels. *Prog Energy Combust Sci* 2012. <https://doi.org/10.1016/j.pecs.2012.03.004>.
- [9] Moriarty P, Honnery D. Can renewable energy power the future? *Energy Policy* 2016. <https://doi.org/10.1016/j.enpol.2016.02.051>.
- [10] Correa SM. A review of NOx formation under gas-turbine combustion conditions. *Combust Sci Technol* 1993. <https://doi.org/10.1080/00102209208947221>.
- [11] Sorrentino G, Sabia P, Bozza P, Ragucci R, de Joannon M. Low-NOx conversion of pure ammonia in a cyclonic burner under locally diluted and preheated conditions. *Appl Energy* 2019. <https://doi.org/10.1016/j.apenergy.2019.113676>.
- [12] Innovation EFP for R and. Horizon 2020 n.d.

REFERENCES

- <https://ec.europa.eu/programmes/horizon2020/>.
- [13] Wu DW, Wang RZ. Combined cooling, heating and power: A review. *Prog Energy Combust Sci* 2006. <https://doi.org/10.1016/j.pecs.2006.02.001>.
- [14] Wüning JA, Wüning JG. FLAMELESS OXIDATION TO REDUCE THERMAL NO-FORMATION. *Prog Energy Combust Sci* 1997.
- [15] Tsuji H, Gupta AK, Hasegawa T, Katsuki M, Kishimoto K, Morita M. High Temperature Air Combustion. 2002. <https://doi.org/10.1201/9781420041033>.
- [16] Duwig C, Stankovic D, Fuchs L, Li G, Gutmark E. Experimental and numerical study of flameless combustion in a model gas turbine combustor. *Combust Sci Technol* 2008. <https://doi.org/10.1080/00102200701739164>.
- [17] Reddy VM, Katoch A, Roberts WL, Kumar S. Experimental and numerical analysis for high intensity swirl based ultra-low emission flameless combustor operating with liquid fuels. *Proc Combust Inst* 2015. <https://doi.org/10.1016/j.proci.2014.05.070>.
- [18] Khalil AEE, Gupta AK. Towards colorless distributed combustion regime. *Fuel* 2017. <https://doi.org/10.1016/j.fuel.2016.12.093>.
- [19] Zhou B, Costa M, Li Z, Aldén M, Bai XS. Characterization of the reaction zone structures in a laboratory combustor using optical diagnostics: From flame to flameless combustion. *Proc Combust Inst* 2017. <https://doi.org/10.1016/j.proci.2016.06.182>.
- [20] Sorrentino G, Sabia P, de Joannon M, Bozza P, Ragucci R. Influence of preheating and thermal power on cyclonic burner characteristics under mild combustion. *Fuel* 2018. <https://doi.org/10.1016/j.fuel.2018.06.049>.
- [21] Khidr KI, Eldrainy YA, EL-Kassaby MM. Towards lower gas turbine emissions: Flameless distributed combustion. *Renew Sustain Energy Rev* 2017. <https://doi.org/10.1016/j.rser.2016.09.032>.
- [22] Cavaliere A, de Joannon M. *Mild Combustion*. vol. 30. 2004. <https://doi.org/10.1016/j.pecs.2004.02.003>.
- [23] De Joannon M, Sabia P, Sorrentino G, Bozza P, Ragucci R. Small size burner combustion stabilization by means of strong cyclonic recirculation. *Proc Combust Inst* 2017;36:3361–9. <https://doi.org/10.1016/j.proci.2016.06.070>.
- [24] Ye J, Medwell PR, Varea E, Kruse S, Dally BB, Pitsch HG. An experimental study on MILD combustion of prevaporised liquid fuels. *Appl Energy* 2015. <https://doi.org/10.1016/j.apenergy.2015.04.019>.
- [25] Li P, Dally BB, Mi J, Wang F. MILD oxy-combustion of gaseous fuels in a laboratory-scale furnace. *Combust Flame* 2013. <https://doi.org/10.1016/j.combustflame.2013.01.024>.

- [26] de Joannon M, Sorrentino G, Cavaliere A. MILD combustion in diffusion-controlled regimes of Hot Diluted Fuel. *Combust Flame* 2012;159:1832–9. <https://doi.org/10.1016/j.combustflame.2012.01.013>.
- [27] Sabia P, Sorrentino G, Bozza P, Ceriello G, Ragucci R, De Joannon M. Fuel and thermal load flexibility of a MILD burner. *Proc Combust Inst* 2019;37:4547–54. <https://doi.org/10.1016/j.proci.2018.09.003>.
- [28] Huang M, Zhang Z, Shao W, Xiong Y, Liu Y, Lei F, et al. Effect of air preheat temperature on the MILD combustion of syngas. *Energy Convers Manag* 2014. <https://doi.org/10.1016/j.enconman.2014.05.038>.
- [29] Parente A, Galletti C, Tognotti L. Effect of the combustion model and kinetic mechanism on the MILD combustion in an industrial burner fed with hydrogen enriched fuels. *Int J Hydrogen Energy* 2008;33:7553–64. <https://doi.org/10.1016/j.ijhydene.2008.09.058>.
- [30] Sabia P, de Joannon M, Fierro S, Tregrossi A, Cavaliere A. Hydrogen-enriched methane Mild Combustion in a well stirred reactor. *Exp Therm Fluid Sci* 2007. <https://doi.org/10.1016/j.expthermflusci.2006.04.016>.
- [31] Oldenhof E, Tummers MJ, van Veen EH, Roekaerts DJEM. Ignition kernel formation and lift-off behaviour of jet-in-hot-coflow flames. *Combust Flame* 2010. <https://doi.org/10.1016/j.combustflame.2010.01.002>.
- [32] Dally BB, Karpetis AN, Barlow RS. Structure of turbulent non-premixed jet flames in a diluted hot coflow. *Proc Combust Inst* 2002. [https://doi.org/10.1016/S1540-7489\(02\)80145-6](https://doi.org/10.1016/S1540-7489(02)80145-6).
- [33] Cabra R, Chen JY, Dibble RW, Karpetis AN, Barlow RS. Lifted methane-air jet flames in a vitiated coflow. *Combust Flame* 2005. <https://doi.org/10.1016/j.combustflame.2005.08.019>.
- [34] Krishnamurthy N, Paul PJ, Blasiak W. Studies on low-intensity oxy-fuel burner. *Proc Combust Inst* 2009. <https://doi.org/10.1016/j.proci.2008.08.011>.
- [35] Plessing T, Peters N, Wüning JG. Laseroptical investigation of highly preheated combustion with strong exhaust gas recirculation. *Symp. Combust.*, 1998. [https://doi.org/10.1016/S0082-0784\(98\)80183-5](https://doi.org/10.1016/S0082-0784(98)80183-5).
- [36] Cavigiolo A, Galbiati MA, Effuggi A, Gelosa D, Rota R. Mild combustion in a laboratory-scale apparatus. *Combust Sci Technol* 2003. <https://doi.org/10.1080/00102200302356>.
- [37] Veríssimo AS, Rocha AMA, Costa M. Importance of the inlet air velocity on the establishment of flameless combustion in a laboratory combustor. *Exp Therm Fluid Sci* 2013. <https://doi.org/10.1016/j.expthermflusci.2012.05.015>.
- [38] Choi GM, Katsuki M. Advanced low NO_x combustion using highly preheated air. *Energy Convers Manag* 2001. <https://doi.org/10.1016/S0196->

- 8904(00)00074-1.
- [39] Li P, Wang F, Mi J, Dally BB, Mei Z. MILD combustion under different premixing patterns and characteristics of the reaction regime. *Energy and Fuels*, 2014. <https://doi.org/10.1021/ef402357t>.
- [40] Özdemir IB, Peters N. Characteristics of the reaction zone in a combustor operating at mild combustion. *Exp Fluids* 2001. <https://doi.org/10.1007/s003480000248>.
- [41] Chinnici A, Tian ZF, Lim JH, Nathan GJ, Dally BB. Comparison of system performance in a hybrid solar receiver combustor operating with MILD and conventional combustion. Part II: Effect of the combustion mode. *Sol Energy* 2017;147:479–88. <https://doi.org/10.1016/j.solener.2017.02.054>.
- [42] Zhao D, Gutmark E, de Goey P. A review of cavity-based trapped vortex, ultra-compact, high-g, inter-turbine combustors. *Prog Energy Combust Sci* 2018. <https://doi.org/10.1016/j.pecs.2017.12.001>.
- [43] Perpignan AAV, Gangoli Rao A, Roekaerts DJEM. Flameless combustion and its potential towards gas turbines. *Prog Energy Combust Sci* 2018. <https://doi.org/10.1016/j.pecs.2018.06.002>.
- [44] Giménez-López J, Aranda V, Millera A, Bilbao R, Alzueta MU. An experimental parametric study of gas reburning under conditions of interest for oxy-fuel combustion. *Fuel Process Technol* 2011. <https://doi.org/10.1016/j.fuproc.2010.11.014>.
- [45] Kim HY, Baek SW, Kim SW. Investigation of fuel lean reburning process in a 1.5 MW boiler. *Appl Energy* 2012. <https://doi.org/10.1016/j.apenergy.2011.05.027>.
- [46] Miller CA, Touati AD, Becker J, Wendt JOL. Nox abatement by fuel-lean reburning: Laboratory combustor and pilot-scale package boiler results. *Symp Combust.*, 1998. [https://doi.org/10.1016/S0082-0784\(98\)80182-3](https://doi.org/10.1016/S0082-0784(98)80182-3).
- [47] Fureby C. Large Eddy Simulation of combustion instabilities in a jet engine afterburner model. *Combust Sci Technol* 2000. <https://doi.org/10.1080/00102200008935818>.
- [48] Parr TP, Gutmark E, Wilson K, Hanson-Parr DM, Yu K, Smith RA, et al. Compact incinerator afterburner concept based on vortex combustion. *Symp Combust* 1996. [https://doi.org/10.1016/S0082-0784\(96\)80078-6](https://doi.org/10.1016/S0082-0784(96)80078-6).
- [49] Katsuki M, Hasegawa T. The science and technology of combustion in highly preheated air. *Symp. Combust.*, 1998. [https://doi.org/10.1016/S0082-0784\(98\)80176-8](https://doi.org/10.1016/S0082-0784(98)80176-8).
- [50] Rafidi N, Blasiak W. Heat transfer characteristics of HiTAC heating furnace using regenerative burners. *Appl Therm Eng* 2006.

- <https://doi.org/10.1016/j.applthermaleng.2005.12.016>.
- [51] Abtahizadeh E, van Oijen J, De Goey P. Numerical study of Mild combustion with entrainment of burned gas into oxidizer and/or fuel streams. *Combust Flame* 2012;159:2155–65. <https://doi.org/10.1016/j.combustflame.2012.02.004>.
- [52] Cheong KP, Wang G, Wang B, Zhu R, Ren W, Mi J. Stability and emission characteristics of nonpremixed MILD combustion from a parallel-jet burner in a cylindrical furnace. *Energy* 2019. <https://doi.org/10.1016/j.energy.2018.12.146>.
- [53] Khalil AEE, Gupta AK. Swirling distributed combustion for clean energy conversion in gas turbine applications. *Appl Energy* 2011. <https://doi.org/10.1016/j.apenergy.2011.03.048>.
- [54] Sorrentino G, Sabia P, De Joannon M, Cavaliere A, Ragucci R. The Effect of Diluent on the Sustainability of MILD Combustion in a Cyclonic Burner. *Flow, Turbul Combust* 2016;96:449–68. <https://doi.org/10.1007/s10494-015-9668-3>.
- [55] Dorigon LJ, Duciak G, Brittes R, Cassol F, Galarça M, França FHR. WSGG correlations based on HITEMP2010 for computation of thermal radiation in non-isothermal, non-homogeneous H₂O/CO₂ mixtures. *Int J Heat Mass Transf* 2013;64:863–73. <https://doi.org/10.1016/j.ijheatmasstransfer.2013.05.010>.
- [56] Noor MM, Wandel AP, Yusaf T. Design and Development of MILD Combustion Burner. *J Mech Eng Sci* 2014. <https://doi.org/10.15282/jmes.5.2013.13.0064>.
- [57] Sorrentino G, Ceriello G, De Joannon M, Sabia P, Ragucci R, Van Oijen J, et al. Numerical Investigation of Moderate or Intense Low-Oxygen Dilution Combustion in a Cyclonic Burner Using a Flamelet-Generated Manifold Approach. *Energy and Fuels* 2018;32:10656–67. <https://doi.org/10.1021/acs.energyfuels.8b01099>.
- [58] Zhang Z, Li X, Zhang L, Luo C, Lu B, Xu Y, et al. Effect of H₂O/CO₂ mixture on heat transfer characteristics of pulverized coal MILD-oxy combustion. *Fuel Process Technol* 2019;184:27–35. <https://doi.org/10.1016/j.fuproc.2018.11.011>.
- [59] Alberti M, Weber R, Mancini M. Re-creating Hottel's emissivity charts for carbon dioxide and extending them to 40bar pressure using HITEMP-2010 data base. *Combust Flame* 2015. <https://doi.org/10.1016/j.combustflame.2014.09.005>.
- [60] Modest MF. Radiation Combined With Conduction and Convection. *Radiat Heat Transf* 2003:680–728. <https://doi.org/10.1016/b978-012503163-9/50022-9>.
- [61] Gebhart B. Surface temperature calculations in radiant surroundings of arbitrary

- complexity-for gray, diffuse radiation. *Int J Heat Mass Transf* 1961;3:341–6. [https://doi.org/10.1016/0017-9310\(61\)90048-5](https://doi.org/10.1016/0017-9310(61)90048-5).
- [62] Dahlquist G, Björck Å. *Numerical Methods in Scientific Computing, Volume I*. 2011. <https://doi.org/10.1137/1.9780898717785>.
- [63] Atherton LJ, Derby JJ, Brown RA. Radiative heat exchange in Czochralski crystal growth. *J Cryst Growth* 1987;84:57–78. [https://doi.org/10.1016/0022-0248\(87\)90114-X](https://doi.org/10.1016/0022-0248(87)90114-X).
- [64] Sorrentino G, Scarpa D, Cavaliere A. Transient inception of MILD combustion in hot diluted diffusion ignition (HDDI) regime: A numerical study. *Proc Combust Inst* 2013. <https://doi.org/10.1016/j.proci.2012.08.002>.
- [65] Isaac BJ, Parente A, Galletti C, Thornock JN, Smith PJ, Tognotti L. A novel methodology for chemical time scale evaluation with detailed chemical reaction kinetics. *Energy and Fuels* 2013. <https://doi.org/10.1021/ef301961x>.
- [66] Doan NAK, Swaminathan N, Minamoto Y. DNS of MILD combustion with mixture fraction variations. *Combust Flame* 2018;189:173–89. <https://doi.org/10.1016/j.combustflame.2017.10.030>.
- [67] Doan NAK, Swaminathan N. Autoignition and flame propagation in non-premixed MILD combustion. *Combust Flame* 2019. <https://doi.org/10.1016/j.combustflame.2018.12.025>.
- [68] Shim Y, Tanaka S, Tanahashi M, Miyauchi T. Local structure and fractal characteristics of H₂-air turbulent premixed flame. *Proc Combust Inst* 2011. <https://doi.org/10.1016/j.proci.2010.09.002>.
- [69] Baum M, Poinso TJ, Haworth DC, Darabiha N. *Direct Numerical Simulation of a Turbulent*. *J Fluid Mech* 1994.
- [70] Minamoto Y, Swaminathan N. Subgrid scale modelling for MILD combustion. *Proc Combust Inst* 2015;35:3529–36. <https://doi.org/10.1016/j.proci.2014.07.025>.
- [71] Minamoto Y, Swaminathan N, Cant SR, Leung T. Morphological and statistical features of reaction zones in MILD and premixed combustion. *Combust Flame* 2014;161:2801–14. <https://doi.org/10.1016/j.combustflame.2014.04.018>.
- [72] Minamoto Y, Swaminathan N. Modelling paradigms for MILD combustion. *Int J Adv Eng Sci Appl Math* 2014. <https://doi.org/10.1007/s12572-014-0106-x>.
- [73] Minamoto Y, Swaminathan N, Cant RS, Leung T. Reaction zones and their structure in MILD combustion. *Combust Sci Technol* 2014. <https://doi.org/10.1080/00102202.2014.902814>.
- [74] Minamoto Y, Swaminathan N. Scalar gradient behaviour in MILD combustion. *Combust Flame* 2014. <https://doi.org/10.1016/j.combustflame.2013.10.005>.

- [75] Galletti C, Parente A, Tognotti L. Numerical and experimental investigation of a mild combustion burner. *Combust Flame* 2007. <https://doi.org/10.1016/j.combustflame.2007.07.016>.
- [76] Aversano G, Bellemans A, Li Z, Coussement A, Gicquel O, Parente A. Application of reduced-order models based on PCA & Kriging for the development of digital twins of reacting flow applications. *Comput Chem Eng* 2019. <https://doi.org/10.1016/j.compchemeng.2018.09.022>.
- [77] Frassoldati A, Sharma P, Cuoci A, Faravelli T, Ranzi E. Kinetic and fluid dynamics modeling of methane/hydrogen jet flames in diluted coflow. *Appl Therm Eng* 2010;30:376–83. <https://doi.org/10.1016/j.applthermaleng.2009.10.001>.
- [78] Aminian J, Galletti C, Shahhosseini S, Tognotti L. Numerical investigation of a MILD combustion burner: Analysis of mixing field, chemical kinetics and turbulence-chemistry interaction. *Flow, Turbul Combust* 2012;88:597–623. <https://doi.org/10.1007/s10494-012-9386-z>.
- [79] Sabia P, de Joannon M. On H₂–O₂ oxidation in several bath gases. *Int J Hydrogen Energy* 2020.
- [80] Lamouroux J, Ihme M, Fiorina B, Gicquel O. Tabulated chemistry approach for diluted combustion regimes with internal recirculation and heat losses. *Combust Flame* 2014;161:2120–36. <https://doi.org/10.1016/j.combustflame.2014.01.015>.
- [81] Locci C, Colin O, Poitou D, Mauss F. A tabulated, flamelet based no model for large eddy simulations of non premixed turbulent jets with enthalpy loss. *Flow, Turbul Combust* 2015;94:691–729. <https://doi.org/10.1007/s10494-014-9591-z>.
- [82] Christo FC, Dally BB. Modeling turbulent reacting jets issuing into a hot and diluted coflow. *Combust Flame* 2005. <https://doi.org/10.1016/j.combustflame.2005.03.002>.
- [83] Chen ZX, Doan NAK, Lv XJ, Swaminathan N, Ceriello G, Sorrentino G, et al. A numerical study of a cyclonic combustor under MILD conditions using non-adiabatic tabulated chemistry. *Energy and Fuels* 2018;32:10256–65. <https://doi.org/10.1021/acs.energyfuels.8b01103>.
- [84] OIJEN JA VAN, GOEY LPH DE. Modelling of Premixed Laminar Flames using Flamelet-Generated Manifolds. *Combust Sci Technol* 2000. <https://doi.org/10.1080/00102200008935814>.
- [85] van Oijen JA, Donini A, Bastiaans RJM, ten Thije Boonkkamp JHM, de Goey LPH. State-of-the-art in premixed combustion modeling using flamelet generated manifolds. *Prog Energy Combust Sci* 2016. <https://doi.org/10.1016/j.pecs.2016.07.001>.

- [86] Ihme M, Zhang J, He G, Dally B. Large-eddy simulation of a jet-in-hot-coflow burner operating in the oxygen-diluted combustion regime. *Flow, Turbul Combust* 2012. <https://doi.org/10.1007/s10494-012-9399-7>.
- [87] Abtahizadeh E, De Goey P, Van Oijen J. Development of a novel flamelet-based model to include preferential diffusion effects in autoignition of CH₄/H₂ flames. *Combust Flame* 2015;162:4358–69. <https://doi.org/10.1016/j.combustflame.2015.06.015>.
- [88] Huang X, Tummers MJ, Roekaerts DJEM. Experimental and numerical study of MILD combustion in a lab-scale furnace. *Energy Procedia* 2017;120:395–402. <https://doi.org/10.1016/j.egypro.2017.07.231>.
- [89] Chen Z, Reddy VM, Ruan S, Doan NAK, Roberts WL, Swaminathan N. Simulation of MILD combustion using Perfectly Stirred Reactor model. *Proc Combust Inst* 2017;36:4279–86. <https://doi.org/10.1016/j.proci.2016.06.007>.
- [90] Magnussen BF. The Eddy Dissipation Concept: A Bridge Between Science and Technology. *ECCOMAS Themat. Conf. Comput. Combust.*, 2005.
- [91] Chomiak J. *Combustion: a study in theory, fact and application*. Abacus press; 1990.
- [92] Ferrarotti M, Li Z, Parente A. On the role of mixing models in the simulation of MILD combustion using finite-rate chemistry combustion models. *Proc Combust Inst* 2019;37:4531–8. <https://doi.org/10.1016/j.proci.2018.07.043>.
- [93] Ferrarotti M, Patrocelli S, Ceriello G, Sorrentino G, Galletti C, Parente A. Assessment of combustion paradigms for modeling a cyclonic burner under MILD Combustion conditions. In: Bockhorn H, Scala F, Commodo M, Tregrossi A, editors. *Ger. Ital. Sect. Combust. Inst. 41th Meet. Ital. Sect. Combust. Inst.*, 2018.
- [94] De A, Oldenhof E, Sathiah P, Roekaerts D. Numerical simulation of Delft-Jet-in-Hot-Coflow (DJHC) flames using the eddy dissipation concept model for turbulence-chemistry interaction. *Flow, Turbul Combust* 2011;87:537–67. <https://doi.org/10.1007/s10494-011-9337-0>.
- [95] Göktolga MU, Van Oijen JA, De Goey LPH. Modeling MILD combustion using a novel multistage FGM method. *Proc Combust Inst* 2017;36:4269–77. <https://doi.org/10.1016/j.proci.2016.06.004>.
- [96] Parente A, Malik MR, Contino F, Cuoci A, Dally BB. Extension of the Eddy Dissipation Concept for turbulence/chemistry interactions to MILD combustion. *Fuel* 2016;163:98–111. <https://doi.org/10.1016/j.fuel.2015.09.020>.
- [97] Rosenmann L, Hartmann JM, Perrin MY, Taine J. Accurate calculated tabulations of ir and raman co₂ line broadening by co₂, h₂o, n₂, o₂ in the 300-2400-k temperature range. *Appl Opt* 1988.

- <https://doi.org/10.1364/AO.27.003902>.
- [98] Becher V, Clausen S, Fateev A, Spliethoff H. Validation of spectral gas radiation models under oxyfuel conditions. Part A: Gas cell experiments. *Int J Greenh Gas Control* 2011. <https://doi.org/10.1016/j.ijggc.2011.05.005>.
- [99] Chui EH, Raithby GD. Computation of radiant heat transfer on a nonorthogonal mesh using the finite-volume method. *Numer Heat Transf Part B Fundam* 1993. <https://doi.org/10.1080/10407799308914901>.
- [100] Rothman LS, Gordon IE, Barber RJ, Dothe H, Gamache RR, Goldman A, et al. HITEMP, the high-temperature molecular spectroscopic database. *J Quant Spectrosc Radiat Transf* 2010. <https://doi.org/10.1016/j.jqsrt.2010.05.001>.
- [101] Pallarés J, Arauzo I, Williams A. Integration of CFD codes and advanced combustion models for quantitative burnout determination. *Fuel* 2007. <https://doi.org/10.1016/j.fuel.2007.01.036>.
- [102] Yang Y Bin, Newman R, Sharifi V, Swithenbank J, Ariss J. Mathematical modelling of straw combustion in a 38 MWe power plant furnace and effect of operating conditions. *Fuel* 2007. <https://doi.org/10.1016/j.fuel.2006.06.023>.
- [103] Barlow RS, Karpetsis AN, Frank JH, Chen JY. Scalar profiles and NO formation in laminar opposed-flow partially premixed methane/air flames. *Combust Flame* 2001. [https://doi.org/10.1016/S0010-2180\(01\)00313-3](https://doi.org/10.1016/S0010-2180(01)00313-3).
- [104] Chu H, Liu F, Zhou H. Calculations of gas thermal radiation transfer in one-dimensional planar enclosure using LBL and SNB models. *Int J Heat Mass Transf* 2011. <https://doi.org/10.1016/j.ijheatmasstransfer.2011.06.002>.
- [105] Modest MF. The Weighted-Sum-of-Gray-Gases Model for Arbitrary Solution Methods in Radiative Transfer. *J Heat Transfer* 2008. <https://doi.org/10.1115/1.2910614>.
- [106] Johansson R, Leckner B, Andersson K, Johnsson F. Account for variations in the H₂O to CO₂ molar ratio when modelling gaseous radiative heat transfer with the weighted-sum-of-grey-gases model. *Combust Flame* 2011;158:893–901. <https://doi.org/10.1016/j.combustflame.2011.02.001>.
- [107] Webb BW, Ma J, Pearson JT, Solovjov VP. SLW modeling of radiation transfer in comprehensive combustion predictions. *Combust Sci Technol* 2018;190:1392–408. <https://doi.org/10.1080/00102202.2018.1452123>.
- [108] Denison MK, Webb BW. An absorption-line blackbody distribution function for efficient calculation of total gas radiative transfer. *J Quant Spectrosc Radiat Transf* 1993. [https://doi.org/10.1016/0022-4073\(93\)90043-H](https://doi.org/10.1016/0022-4073(93)90043-H).
- [109] Carvalho MG, Farias TL. Modelling of heat transfer in radiating and combusting systems. *Chem Eng Res Des* 1998. <https://doi.org/10.1205/026387698524749>.

REFERENCES

- [110] Hu G, Schietekat CM, Zhang Y, Qian F, Heynderickx G, Van Geem KM, et al. Impact of radiation models in coupled simulations of steam cracking furnaces and reactors. *Ind Eng Chem Res* 2015. <https://doi.org/10.1021/ie5042337>.
- [111] Sorrentino G, Sabia P, De Joannon M, Ragucci R, Cavaliere A, Göktolga U, et al. Development of a Novel Cyclonic Flow Combustion Chamber for Achieving MILD/Flameless Combustion. *Phys Procedia* 2015;66:141–4. <https://doi.org/10.1016/j.egypro.2015.02.079>.
- [112] Kreith F, Bohn M, Kirkpatrick A. Principles of Heat Transfer. *J Sol Energy Eng* 2008. <https://doi.org/10.1115/1.2887901>.
- [113] Cho ES, Danon B, de Jong W, Roekaerts DJEM. Behavior of a 300kWth regenerative multi-burner flameless oxidation furnace. *Appl Energy* 2011;88:4952–9. <https://doi.org/10.1016/j.apenergy.2011.06.039>.
- [114] Peters N. Laminar diffusion flamelet models in non-premixed turbulent combustion. *Prog Energy Combust Sci* 1984. [https://doi.org/10.1016/0360-1285\(84\)90114-X](https://doi.org/10.1016/0360-1285(84)90114-X).
- [115] Maas U, Pope SB. Simplifying chemical kinetics: Intrinsic low-dimensional manifolds in composition space. *Combust Flame* 1992. [https://doi.org/10.1016/0010-2180\(92\)90034-M](https://doi.org/10.1016/0010-2180(92)90034-M).
- [116] Vasavan A, De Goey P, Van Oijen J. Numerical Study on the Autoignition of Biogas in Moderate or Intense Low Oxygen Dilution Nonpremixed Combustion Systems. *Energy and Fuels* 2018;32:8768–80. <https://doi.org/10.1021/acs.energyfuels.8b01388>.
- [117] Gerstein M. The structure of laminar flames. *Symp Combust* 1953. [https://doi.org/10.1016/S0082-0784\(53\)80008-1](https://doi.org/10.1016/S0082-0784(53)80008-1).
- [118] Sorrentino G, Göktolga U, De Joannon M, Van Oijen J, Cavaliere A, De Goey P. An experimental and numerical study of MILD combustion in a Cyclonic burner. *Energy Procedia*, 2017. <https://doi.org/10.1016/j.egypro.2017.07.173>.
- [119] Somers LMT. Ph.D. Thesis. Technische Universiteit Eindhoven, 1994.
- [120] Bilger RW, Stårner SH, Kee RJ. On reduced mechanisms for methane-air combustion in nonpremixed flames. *Combust Flame* 1990. [https://doi.org/10.1016/0010-2180\(90\)90122-8](https://doi.org/10.1016/0010-2180(90)90122-8).
- [121] Medwell PR, Kalt PAM, Dally BB. Imaging of diluted turbulent ethylene flames stabilized on a Jet in Hot Coflow (JHC) burner. *Combust Flame* 2008. <https://doi.org/10.1016/j.combustflame.2007.09.003>.
- [122] The Mathworks, Inc. MATLAB, Version 9.6 2019. MATLAB - MathWorks - MATLAB. [WwwMathworksCom/Products/Matlab](http://www.MathworksCom/Products/Matlab) 2019.
- [123] Vreman AW, Albrecht BA, van Oijen JA, de Goey LPH, Bastiaans RJM.

- Premixed and nonpremixed generated manifolds in large-eddy simulation of Sandia flame D and F. *Combust Flame* 2008. <https://doi.org/10.1016/j.combustflame.2008.01.009>.
- [124] Ansys. ANSYS ICEM CFD User Manual. Knowl Creat Diffus Util 2016.
- [125] ANSYS-Fluent User's Guide. ANSYS FLUENT Theory Guide. Release 182 2013. [https://doi.org/10.1016/0140-3664\(87\)90311-2](https://doi.org/10.1016/0140-3664(87)90311-2).
- [126] Aminian J, Galletti C, Shahhosseini S, Tognotti L. Key modeling issues in prediction of minor species in diluted-preheated combustion conditions. *Appl Therm Eng* 2011. <https://doi.org/10.1016/j.applthermaleng.2011.06.007>.
- [127] Eckert ERG. Radiative transfer, H. C. Hottel and A. F. Sarofim, McGraw-Hill Book Company, New York, 1967. 52 pages. *AIChE J* 2004. <https://doi.org/10.1002/aic.690150504>.
- [128] Peters N. Turbulent Combustion. 2000. <https://doi.org/10.1017/cbo9780511612701>.
- [129] University of California. The San Diego Mechanism. Research 2012.
- [130] Leung KM, Lindstedt RP. Detailed kinetic modeling of C1 - C3 alkane diffusion flames. *Combust Flame* 1995. [https://doi.org/10.1016/0010-2180\(94\)00254-P](https://doi.org/10.1016/0010-2180(94)00254-P).
- [131] Sabia P, de Joannon M, Sorrentino G, Giudicianni P, Ragucci R. Effects of mixture composition, dilution level and pressure on auto-ignition delay times of propane mixtures. *Chem Eng J* 2015. <https://doi.org/10.1016/j.cej.2015.04.143>.
- [132] Mardani A, Tabejamaat S, Hassanpour S. Numerical study of CO and CO₂ formation in CH₄/H₂ blended flame under MILD condition. *Combust Flame* 2013. <https://doi.org/10.1016/j.combustflame.2013.04.003>.
- [133] Reaction Design: San Diego. CHEMKIN-PRO 2013.
- [134] Locci C, Colin O, Michel JB. Large Eddy simulations of a small-scale flameless combustor by means of diluted homogeneous reactors. *Flow, Turbul Combust* 2014;93:305–47. <https://doi.org/10.1007/s10494-014-9548-2>.

Acknowledgements

I wish to express my gratitude to my academic tutor Prof. Antonio Cavaliere. Thank you for the constant inspiration and passion you conveyed to me, first when I was a master student and then during my PhD. Your scientific integrity has been a guide in allowing me to develop critical thinking and grow up as scientist, engineer and person.

I would also like to acknowledge my co-tutors, Dr. Giancarlo Sorrentino from the University of Naples and Dr. Raffaele Ragucci from the CNR of Naples. You let me explore my research topic in a free way, but always being there to give me support and advice, helping me to focus my research on the right path. You've given me every possible opportunity to improve my skills and make the best experiences with courses and schools. You helped me to build self-confidence allowing me to attend conferences and present my work in public.

I feel also very grateful towards the researchers of the CNR Dr Mara de Joannon, Dr Pino Sabia and Dr Paola Giudicianni. I deeply thank you for the guidance and support for the experiments. I truly admire your persistence in pursuing the best solutions for problems. I would like to express my gratitude to all of you for your patience and generosity in our discussions. Thanks for having created a safe and efficient lab environment. I have learned new aspects of a laboratory life from you.

I want to thank Prof. Jeroen van Oijen from the University of Technology of Eindhoven which hosted me at TU/e before and during my PhD. I owe you so much for helping me to deal with my first experiences with computer codes and numerical modelling. I couldn't make so much in the understanding and fixing of the queries of my research without your support.

I also wish to acknowledge Prof. Swaminathan from the University of Cambridge. You gave me the opportunity to spend time in your lab working in a very interesting and motivating environment. I really appreciated the discussions we had, and I feel you have helped me to improve myself.

Many thanks to Prof. Chiara Galletti from the University of Pisa. Our meetings and discussions have inspired me to focus the attention towards specific aspects regarding fluid-dynamics and heat transfer mechanisms.

I also acknowledge Prof. Alessandro Parente from the Université libre de Bruxelles (ULB) for the helpful advices he gave me and the fruitful discussions we had on several occasions. Moreover, I deeply thank the Prof. for accepting to take part to the committee for the final discussion of this thesis.

Then I thank all the Postdocs and PhDs I worked with in Naples over the years, Marco Lubrano Lavadera, Corinna Maria Grottola, Pio Bozza, Virginia Manna, Giovanni Ariemma and Marco Agrillo. I had a great time with you working together and facing all kind of problems always with a positive attitude. Discussions with you guys were enlightening for my research. I will always carry with me the moments we shared.

A 3 years Doctorate is not only a scientific and professional journey but is a cathartic period of deep personal growth. Therefore, I wish to thank all my friends that helped me to make this process step by step. I'd rather not mention anyone for fear of forgetting someone, but you guys know who I turn to.

I say thank you to my parents Angelo and Lucia from the bottom of my heart. Without your support, none of this would have been possible. Although some frictions and misunderstandings, you were always there to back up me when I most needed and I know you always will. Thank you to my gorgeous and smart sister Francesca. I just want to say to you that your big brother loves you and is there for you anytime.

Thanks to all my family for the love and support I constantly received from you. In particular my endless gratitude to my grandpa Geppino, my grandma Fortuna and to my special hero Ciro (miss you everyday buddy). Thank you to my "number one" uncle Enzo and my lovely aunt Anna and my cousins Ulderico and Arianna. I can never imagine my life without you all.

These three years have been an unforgettable journey. I really want to say thank you to all the people who have contributed to this and that I did not mention.